eXPRESS Polymer Letters Vol.4, No.3 (2010) 130
Available online at www.expresspolymlett.com
DOI: 10.3144/expresspolymlett.2010.17

Editorial corner – a personal view
Nanocomposites, excellent properties or hype?

*J. Seppälä**

Faculty of Chemistry and Materials Sciences, Department of Biotechnology and Chemical Technology,
Polymer Technology Research Group, Helsinki University of Technology, P.O. Box 6100, FI-02015 TKK, Finland

Nanotechnology, nanostructured polymers, nanoparticles and nanocomposites have been a hot research topic of high promise for years. A lot has been done, highly interesting scientific findings and even significant technical applications, yet there are still unfulfilled promises and visions to be made true.

Carbon nanotubes, nanofibrous cellulose and TiO_2-nanoparticles, just to mention a few, have numerous interesting properties that might upgrade polymer properties to a new level in composites, that at least is the high flying vision for the future.

However, some of the visions and promises seem to have been heavily hyped up. Often individual nanofibre's or particle's properties are extrapolated straight forward to the bulk material's technical properties – and the hype is ready. By using e.g. tiny amounts of CNF's on polymer matrix we are promised extraordinary mechanical stiffness and toughness, superior electrical conductivity, high heat conductivity, light weight and excellent processability. Often said prerequisites are nanoscale dispersion in a polymer matrix and good interfacial adhesion i.e. compatibility. Is this all that is needed? No, also a rather high nanoparticle concentration is often needed, to ensure percolation for electrical conductivity or entanglements for mechanical reinforcing.

In addition, the state of the art in technical composites is still far away from the fantastic visions. Carbon nanofibre concentrations of 2–3% are needed to exceed the percolation limit for electrical conductivity. The mechanical toughness increment is around 30% by using the CNF's, a level easily achievable with conventional reinforcements. High heat conductivities by using small amounts of NFC's in composites is just a dream, at least based on our experiments.

Too often in nanocomposite articles only one mechanical parameter, modulus, is reported. This does not give a comprehensive picture of the essential properties of the materials. Actually, it is rather obvious to achieve high modulus values in blends and composites whilst effects on elongation and breaking energy are neglected. So there seems to be lacking in information and contradiction between phenomena and wishes in the field.

In spite of this criticism it is good to keep in mind that nature is a master in optimising nanostructures in materials. Also, nature has shown that significant improvements in materials properties can be reached, and tailored properties achieved. Can we, as polymer scientists, achieve something that even remotely resembles the level of control that can be found in nature's materials.

Prof. Dr. Jukka Seppälä
Member of International Advisory Board

*Corresponding author, e-mail: jukka.seppala@tkk.fi

eXPRESS Polymer Letters Vol.4, No.3 (2010) 131-140
Available online at www.expresspolymlett.com
DOI: 10.3144/expresspolymlett.2010.18

Effect of nano-Si_3N_4 surface treatment on the tribological performance of epoxy composite

Y. Luo[1,2*], *X. Y. Yu*[1], *X. M. Dong*[1,2], *M. Z. Rong*[2], *M. Q. Zhang*[2]

[1]Department of Applied Chemistry, College of Science, South China Agricultural University, Guangzhou 510642, People' Republic of China
[2]Key Laboratory for Polymeric Composite and Functional Materials of Ministry of Education, Zhongshan University, Guangzhou 510275, People' Republic of China

Received 18 October 2009; accepted in revised form 15 December 2009

Abstract. To overcome the disadvantages generated by the loose nano-partilce agglomerates dispersed in polymer composites, a chemical grafting method was applied to modify nano-Si_3N_4 by covalently bonding glycidyl methacrylate (GMA) onto the particles. The tribological behavior of the epoxy composite filled with nano-Si_3N_4 or GMA treated Si_3N_4 (Si_3N_4-g-PGMA) was studied using a ring-on-block wear tester under dry sliding, and the worn surface of the filled epoxy composite and the surface roughness of the composites after the sliding wear test were investigated by SEM (scanning electron microscopy) and AFM (atomic force microscopy), respectively. In comparison to the composites filled with untreated nano-Si_3N_4 particles, the composites with the grafted nano-Si_3N_4 exhibit improved sliding wear resistance and reduced friction coefficient owing to the chemical bonding at the filler/matrix interface.

Keywords: *nanocomposites, nano-Si_3N_4 particles, surface grafting, friction and wear*

1. Introduction

Polymers and polymer composites have been used increasingly as engineering materials for technical applications in which tribological properties are of considerable importance. Recent investigations on inorganic nanoparticles filled polymers demonstrate their significant potential in producing composites with low friction and high wear resistance [1–5]. Compared with the composites incorporated with micro-particles, which are characterized by severe wear resulting from abrasion and particles pull-out, nanocomposites exhibit rather mild wear with fine individual debris acting as lubricant and contributing to material removal by polishing. Evidently, a uniform dispersion of nanoparticles and strong filler/matrix interfacial interaction in the composites are the prerequisites for the aforesaid performance improvement.

It is worth noting that nanoparticles are very difficult to be uniformly dispersed in polymers because of the strong attraction between the particles and the limited shear force during compounding. Consequently, nano-particle filled polymers used to contain a number of loose clusters of nanoparticles, which would lead to extensive material loss in terms of disintegration and crumbling of the particle agglomerates under tribological conditions. To avoid these drawbacks, a series of methods have been attempted in two aspects: development of new compounding (dispersion) techniques and surface pretreatment approaches for nanoparticles. Comparatively, surface modification of nano-fillers is more effective and easier to be applied. Similar to the case of micro-size particles, surface treatment of inorganic nanoparticles can be conducted by either physical or chemical method. The former

*Corresponding author, e-mail: luoying@scau.edu.cn

deals with surfactant treatment [6] and polymer encapsulation [7], while the later is related to coupling agent treatment [8–9] and graft polymerization [10–14]. Comparatively, the effect of surface modification based on chemical interaction is more significant, as it provides stronger interaction between modifiers and nanoparticles.

In our previous works, graft polymerization onto nanoparticles proved to be feasible in improving tribological behavior of polymer nanocomposites [15–19]. The grafted polymers changed the hydrophilic surface feature of the particles to hydrophobic and broke apart the nanoparticle agglomerates during polymerization process. Besides, filler/matrix interfacial interaction in the composites was enhanced mainly due to chain entanglement of grafted polymer with matrix polymer. Actually, the interfacial adhesion can be further increased if a chemical reaction between the filler and matrix could take place. This concept is similar to the reactive compatibilization employed in making polymer blends.

In this work, nano-Si_3N_4 particles grafted by polyglycidyl methacrylate (PGMA) were mixed with epoxy. The grafted polymer PGMA was selected because the epoxide groups on PGMA would take part in curing reaction of epoxy resin, so that the nano-Si_3N_4 particles could be covalently connected to the matrix. The technical route is believed to be beneficial to the tribological performance of the composites.

2. Materials and methods

2.1. Materials

The nano-size Si_3N_4 particles supplied by the Hua-Tai, China, have a specific surface area of 52 m^2/g and an averaged diameter of 17 nm, respectively. Prior to use, the particles were dried in an oven at 110°C vacuum for 24 h to get rid of the physically absorbed and weakly chemically absorbed species. Bisphenol-A epoxy resin (type E-51) was provided by Guangzhou Dongfeng Chemical Co., China. The curing agent 4,4′-diaminodiphenysulfone (DDS) was supplied by Shanghai Medical Agents Co., China. A silane coupling agent (γ-methacryloxypropyl trimethoxy silane, provided by Liao Ning Gaizhou Chemical Industry Co., China) was employed to introduce the reactive double bonds on the surface of the nanoparticles prior to graft polymerization. The grafting monomer glycidyl methacrylate (GMA, Shanghai Yuanji Chemical Engineering Co., China) was distilled under low pressure before use.

2.2. Graft polymerization onto Si_3N_4 nanoparticles

The nanoparticles were grafted with PGMA by surfactant-free emulsion graft polymerization. The details of the surfactant-free emulsion graft polymerization have been described in Reference [20]. After the graft polymerization, the resultant suspension was filtered, washed, and extracted with methanol for 8 h to remove the residual monomer. The dried mixture was extracted with acetone for 50 h to isolate the polymer-grafted Si_3N_4 (Si_3N_4-g-PGMA) from the absorbed homopolymers. Then the grafted nanoparticles were dried under vacuum at 50°C. Some of them were transferred to Shimadzu TA-50 thermogravimeter to determine the percent grafting, γ_g. In the subsequent procedures of composites manufacturing, the Si_3N_4-g-PGMA with a percent grafting of 7.25 wt% was used as the treated fillers. Besides, Fourier transform infrared (FTIR) spectroscopy was used to evaluate the reactivity of Si_3N_4-g-PGMA with the curing agent DDS.

2.3. Manufacturing of epoxy based nanocomposites

The composite materials were fabricated by mixing the (untreated or treated) Si_3N_4 nanoparticles and epoxy (EP) together with a fast stirring for 3 h under vacuum, and then ultrasonic agitation for 1h. After that, the mixture was heated to 130°C and the curing agent (DDS) was added under continuous stirring. Then the composite system was poured into a preheated mold and the curing procedure began after extraction of possible air bubbles for 45 min. The curing proceeded step by step as follows: 3 h at 100°C, 2 h at 140°C, 2 h at 180°C, and 2 h at 200°C.

2.4. Characterization

Unlubricated sliding wear tests were carried out on a pin-on-ring configuration at a constant velocity of 0.42 m/s and pressure of 3 MPa to obtain specific wear rate, w_s, and friction coefficient, μ. The con-

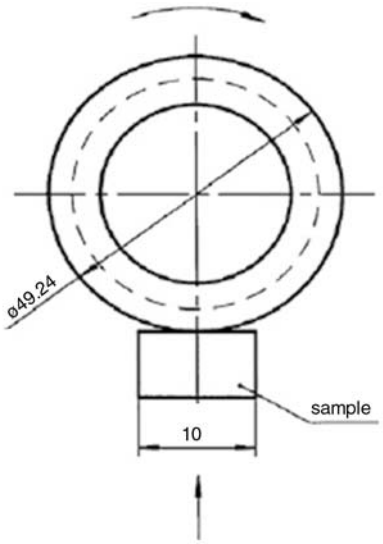

Figure 1. Contact schematic diagram for the friction couple

tact schematic diagram of the frictional couple is shown in Figure 1. The carbon steel ring (0.42–0.45 wt% C, 0.17–0.37 wt% Si and 0.5–0.8 wt% Mn, HRC 50) had a diameter of 40 mm and an initial surface roughness of 0.1 μm. The specimens for wear tests were machined with a geometry of 5 mm×10 mm×15 mm, resulting in an apparent contact area of about 5 mm×10 mm. Prior to wear testing, all the samples were pre-worn to average surface conditions and to reduce the running-in period. The actual steady-state test was conducted for 3 h using the same steel ring as that used for the pre-worn procedure. After that, a weight measure of the specimens was conducted.

The worn surfaces of the specimens were observed by a Philips XL-30FEG scanning electron microscope (SEM). Transmission electron microscopic (TEM) observation was performed with a Philips EM400 on the sample prepared from acetone dispersion of the particles (0.1 g in 50 ml), which were sonicated for 45 min and then deposited on copper grids covered by carbon film. The roughness of the worn surface was measured by SPM-9500J3 atomic force microscope (AFM). X-ray energy distribution spectra (EDS) of the counterpart steel rings were collected with a LINK-ISIS 300 apparatus at an accelerating voltage of 20 kV. X-ray photoelectron spectra (XPS) of the composites' surface were recorded by means of a Vacuum Generators Escalab MK II X-ray photoelectron spectrometer with a resolution of 0.8 eV at 240 W (Mg K_α 12 kV). Three-point bending tests of the composites specimens were carried out in a Hounsfield universal tester in accordance with GB/T1039-92 standard at a deformation rate of 5 mm/min.

3. Results and discussion

3.1. Surfactant-free emulsion graft polymerization of GMA and its characterization

When nanoparticles are mixed with epoxy, whether a stationary suspension state can be kept is of the first importance for producing homogeneous composites. To check the effect of surface treatment qualitatively, the dispersibility of PGMA grafted Si_3N_4 in acetone was compared with that of the untreated nano-Si_3N_4 (Figure 2). The results clearly show that a remarkable improvement of dispersibility of the former particles originating from the surface grafting. Untreated nano-Si_3N_4 completely precipitates after a few hours. On the contrary, Si_3N_4-g-PGMA gives a stable colloidal dispersion in the solvent. In addition, the grafted nano-Si_3N_4 particles with higher percent grafting (48%) tend to be less stable than that with lower percent grafting (7%) within 25 h, indicating that excessive graft polymer chains interfere with the dispersion of nano-Si_3N_4 particles due to molecular entanglement.

Figure 3 shows the TEM morphologies of the nano-Si_3N_4 particles before and after the grafting treatment in acetone. Due to the serious aggregation resulting from the high specific surface area, the untreated nano-Si_3N_4 particles get together forming clusters larger than 500 nm. When the particles are grafted by PGMA, they can be well dispersed in the

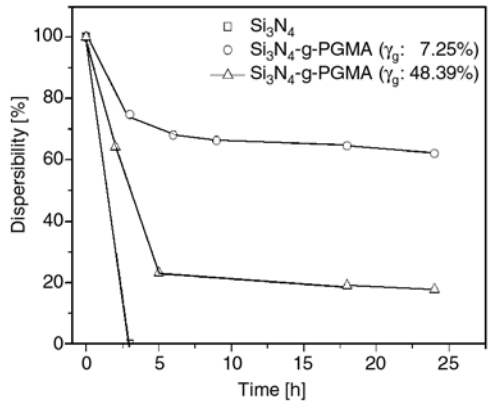

Figure 2. Dispersibility of nano-Si_3N_4 particles and Si_3N_4-g-PGMA particles with different grafting percent in acetone at room temperature

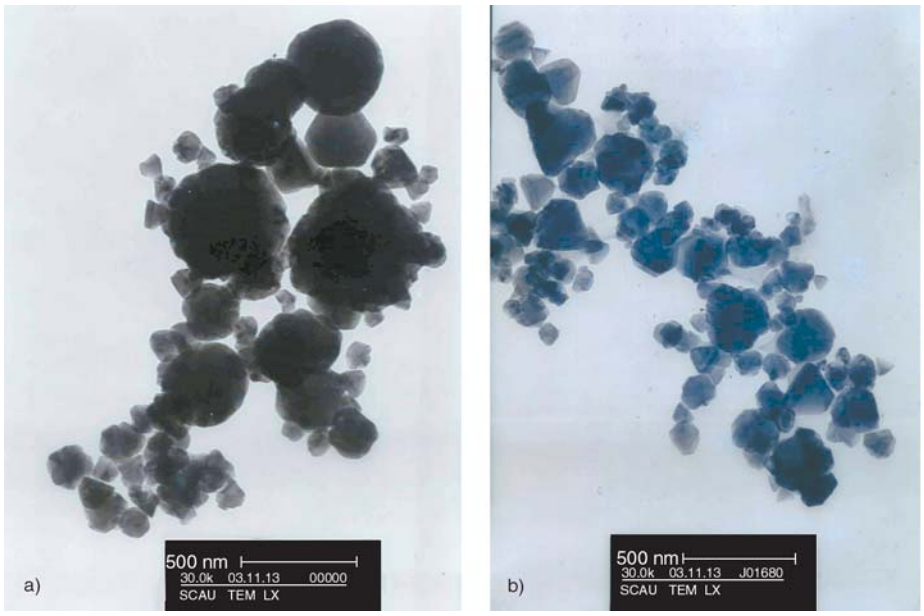

Figure 3. TEM photos of (a) nano-Si_3N_4 particles and (b) Si_3N_4-g-PGMA particles (γ_g: 7.25%)

solvent and most of them have sizes smaller than 100 nm. A comparison between Figures 3a and 3b obviously demonstrates that the graft treatment is rather effective in separating the agglomerated nanoparticles, which would benefit the subsequent composites manufacturing.

Since the surface treatment of the particles aims at increasing the reactive compatibilization in the nanocomposites by grafting polymers with reactive groups onto the nanoparticles, the reactivity of the grafted polymer should be of interests. Firstly, it is needed to confirm whether the epoxide groups of PGMA grafted on the nano-Si_3N_4 particles will react with the amine groups of DDS. To prove the reaction, a model system consisting of stoichimetrical Si_3N_4-g-PGMA and the curing agent 4,4′-diamino-diphenysulfone (DDS) was thermally treated following the same curing sequence as that applied for epoxy/DDS compound, and then evaluated by FTIR. It is seen from Figure 4 that the double bands at 3332 and 3369 cm^{-1} corresponding to the primary amine groups ($–NH_2$) disappear after curing. Instead, a single band at 3365 cm^{-1} representing the secondary amine groups (–NH) is perceived, evidencing the above deduction. Therefore, it is known that PGMA is able to take part in the curing reaction of epoxy. Such a chemical bonding between the PGMA chains grafted onto nano-Si_3N_4 particles and the surrounding epoxy networks would certainly enhance the filler/matrix adhesion in the composites.

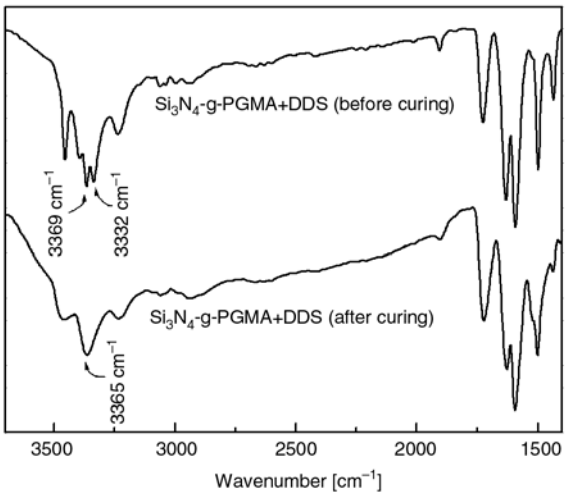

Figure 4. FTIR spectra of the mixture of Si_3N_4-g-PGMA/DDS before and after curing

3.2. Friction and wear performance of Si_3N_4/EP nanocomposites

To illuminate the effect of the grafting polymer on the tribological performance of the epoxy composites, Figure 5 presents the specific wear rate, w_s, and frictional coefficient, μ, as a function of the amount of the grafting polymers attached to nano-Si_3N_4 particles. It is found that the particles with a medium grafting percentage (γ_g = 7.25%) give the lowest w_s and μ. It can thus be estimated that the molecular chains of the grafted PGMA with a medium grafting percentage might present themselves in an extended conformation, which is beneficial to the dispersion of the grafted particles and

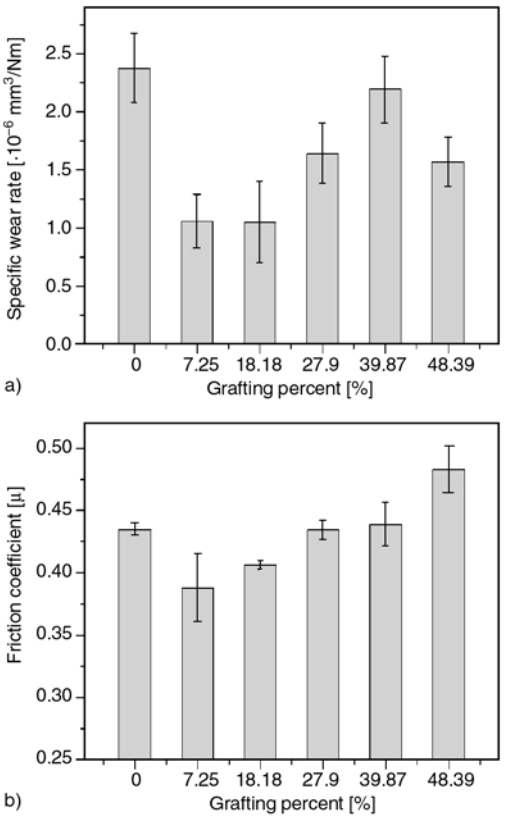

Figure 5. (a) Specific wear rate, w_s, and (b) friction coefficient, μ, of epoxy composites filled with Si_3N_4-g-PGMA (0.79 vol%) with different grafting percentage

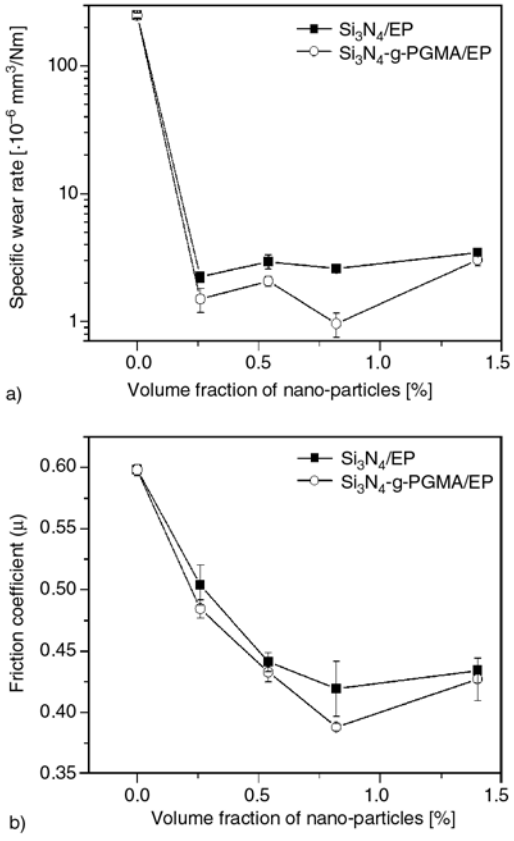

Figure 6. (a) Specific wear rate and (b) friction coefficient of Si_3N_4/EP and Si_3N_4-g-PGMA/EP (γ_g: 7.25%) composites as a function of filler content

the establishment of chemical bonding between the particles and the matrix.

The typical steady-state friction coefficients and specific wear rates of the unfilled and filled epoxy composites under 3 MPa and at 0.42 m/s are shown in Table 1. It can be seen that Si_3N_4 and Si_3N_4-g-PGMA can reduce the friction coefficient and specific wear rate of the epoxy composites significantly. Comparatively, 0.52 vol% Si_3N_4-g-PGMA is more effective than untreated Si_3N_4 in improving the tribological performance of the composites. Furthermore, when the composites are mixed with the help of acetone solvent (wet mixed), it holds the lowest friction coefficient and specific wear rate under a pressure of 3 MPa.

Effect of the content of Si_3N_4 and Si_3N_4-g-PGMA on the friction coefficient and specific wear rate of the epoxy composite sliding against the steel ring is revealed in Figure 6 under dry sliding. It is seen that within the entire range of filler content of interests, both frictional coefficient and specific wear rate of the composites incorporated with nano-Si_3N_4 particles show a drastical decrease as compared with the values of unfilled epoxy. For example, the wear rate of epoxy is decreased from ~$200 \cdot 10^{-6}$ to ~$2.6 \cdot 10^{-6}$ and $0.96 \cdot 10^{-6}$ mm³/Nm by the addition of 0.8 vol% of untreated nano-Si_3N_4 and treated nano-Si_3N_4, respectively. Comparatively, Si_3N_4-g-PGMA is more effective than untreated Si_3N_4 in improving the tribological performance of the composites. The difference in improving the wear resistance of epoxy between the composites with untreated and treated nano-Si_3N_4 particles should mainly result from the filler/

Table 1. Typical friction coefficient and specific wear rate of epoxy composites under dry sliding (3 MPa, 0.42 m/s)

Composites	Friction coefficient	Specific wear rate [·10⁻⁶ mm³/Nm]
Epoxy+DDS	0.598	248.75
Epoxy+DDS+0.52 vol% Si_3N_4	0.441	2.95
Epoxy+DDS+0.52 vol% Si_3N_4-g-PGMA (dry mixed)	0.433	2.33
Epoxy+DDS+0.52 vol% Si_3N_4-g-PGMA (wet mixed)	0.428	1.55

matrix adhesion strength. As stated before, the grafted PGMA employed in the present work can build up chemical bonding between the nanoparticles and epoxy resin, which should be responsible for the higher resistance to periodic frictional stress. With a rise in the nanoparticles concentration, both the wear rate and the friction coefficient increase slightly. It might be due to the fact that the increased amount of the nanoparticles is unfavorable to filler dispersion [21]. Meanwhile, the grafted nanoparticles also lead to more significant reduction on specific wear rate of epoxy as compared with the friction coefficient.

Figure 7 compares the worn surface of unfilled epoxy with those of the composites. Clearly, the severe wear associated with the detachment of bulk materials for unfilled epoxy (Figure 7a, 7b) is replaced by the mild wear for untreated Si_3N_4 filled composites (Figure 7c, 7d). In comparison with the flake-like wear failures on the surface of Si_3N_4/EP, the wear scars on the surface of Si_3N_4-g-PGMA/EP composites (Figure 7e, 7f) are characterized by tiny

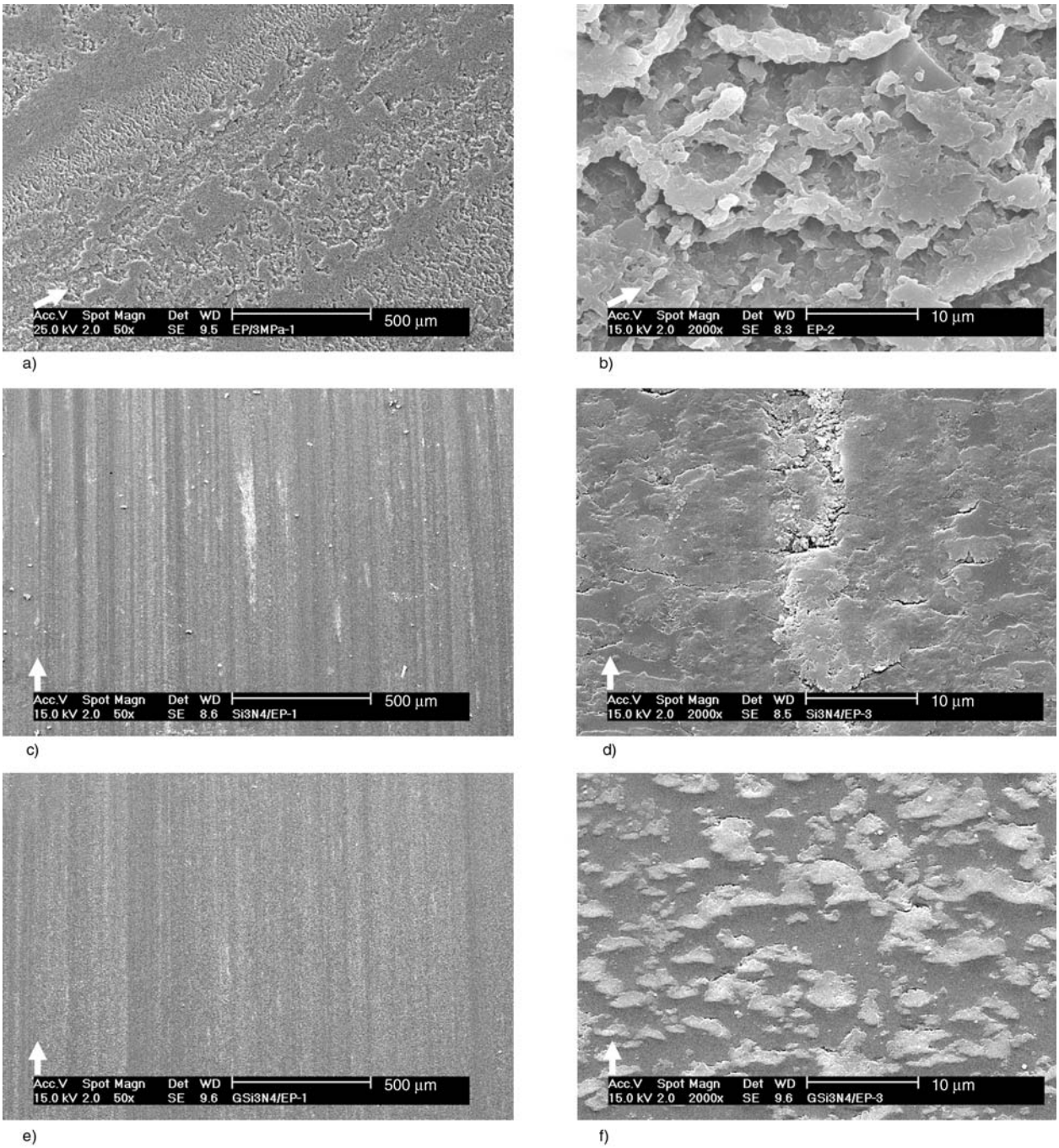

Figure 7. SEM micrographs of the worn surface of (a, b) epoxy, (c, d) Si_3N_4/epoxy composites (0.79 vol%), and (e, f) 'dry mixed' Si_3N_4-g-PGMA/epoxy composites (0.79 vol%, γ_g: 7.25%) (arrows indicate the sliding direction)

scratches without any detached flakes. It can be attributed to the fact that the treatment via graft polymerization onto the nanoparticles further improves the miscibility between the grafted polymer and matrix epoxy. It should be beneficial to the dispersion of nano-Si_3N_4 particles, and improve the composites' integrity. As a result, the composites' wear resistance was raised accordingly. On the other hand, it suggests that polishing effect predominates the wear process of the latter composites, evidencing the change in wear mode.

3.3. Effect of the reaction between grafted polymer and epoxy matrix on the composites' surface feature

The aforementioned results have demonstrated the efficiency of surface grafting treatment of Si_3N_4 nanoparticles in improving sliding wear properties of epoxy composites. Nevertheless, some details of the role of the chemical bonding on the composites' surface characteristics should be further investigated. Figure 8 shows the surface feature of epoxy and its composites characterized by load-unload curves recorded during the micro-hardness measurements. In the case of unfilled epoxy, the worn surface exhibits greater portion of plastic deformation as compared with the unworn one. This reflects destruction of the epoxy network due to the high frictional temperature. However, the addition of nano-Si_3N_4 particles exerts restraining effect on the plastic deformation, and even results in a rise in the elastic deformation after the wear test, proving that the interaction between nano-Si_3N_4 particles and epoxy is rather strong. When the Si_3N_4 had been grafted with PGMA, the elastic deformation of the composites is further improved due to the chemical bonding at the interface.

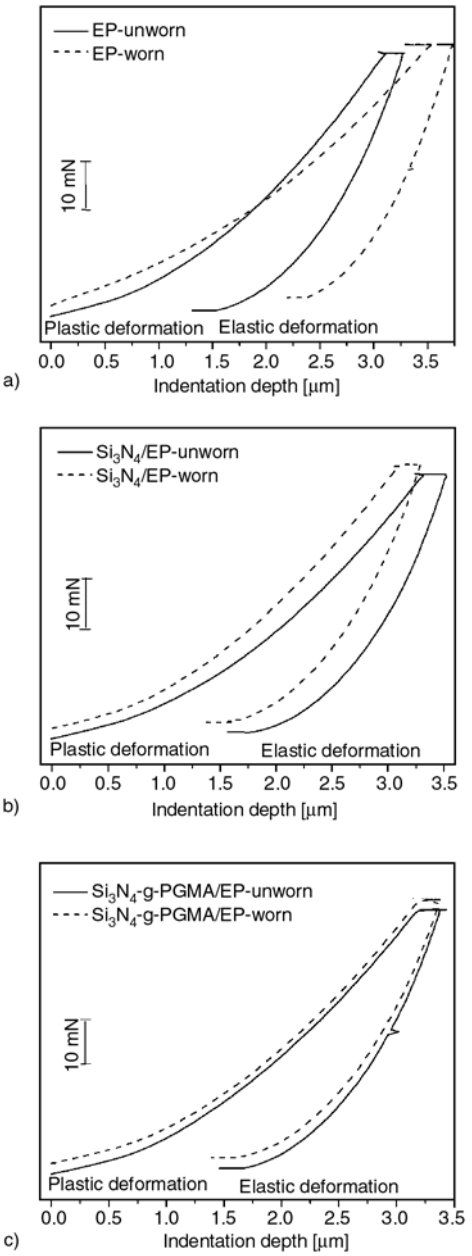

Figure 8. Load-unload test results of (a) epoxy, (b) Si_3N_4/EP (0.26 vol%) and (c) Si_3N_4-g-PGMA/EP (0.26 vol%, γ_g: 7.25%) composites before and after the wear test

Quantitative description of the worn pin surface profile by AFM presents information about the improvement of the composites' resistance to surface shearing due to the incorporation of nano-Si_3N_4 particles from another angle (Figure 9). Clearly, the wear process in the Si_3N_4 filled nanocomposites are dominated by polishing and the worn pin surface appears rather smooth. When the particles were grafted with PGMA, the average roughness of the composites is further reduced by three to four times. The results agree with the aforesaid enhanced integrity and higher wear resistance of the composites.

To illuminate the influence of the chemical bonding on the materials transfer from the specimens to the steel counterpart during wear test, elements on the steel ring surface were examined in Table 2. It is seen that having rubbed against either the unfilled epoxy or the epoxy composites, element Si was detected on the steel counter face. Besides, the amount of Si on the steel ring surface rubbing against the composites is higher than that on the

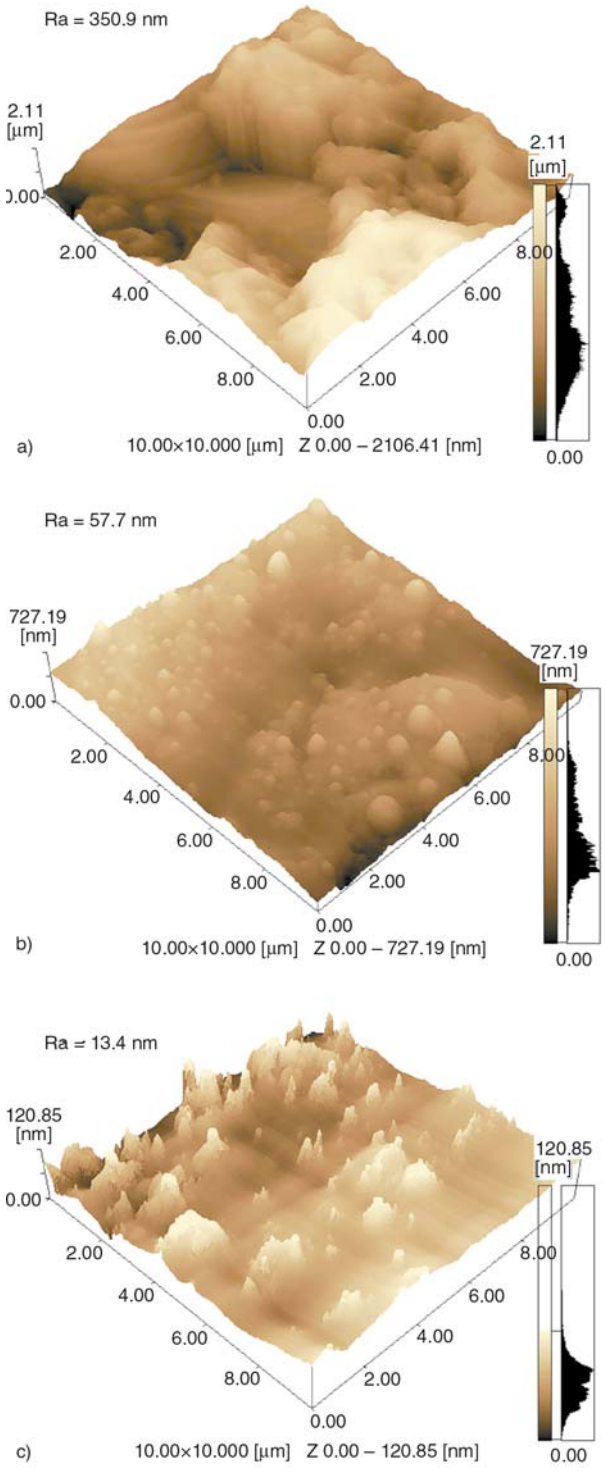

Figure 9. AFM 3D height trace images of worn surface of (a) epoxy, (b) Si_3N_4/EP (0.26 vol%) and (c) Si_3N_4-g-PGMA/EP (0.26 vol%, γ_g: 7.25%) composites

steel ring rubbing against neat epoxy. These data prove that the grafted polymer facilitates the adhesion of Si_3N_4 particles on the steel ring, and strengthens the transferred film. Besides, the low resolution XPS spectra of the pin surfaces of epoxy

Table 2. EDS analysis of the surface of the steel counterpart before and after the wear test

Samples	Elements and contents [wt%]		
	Fe	Si	S
Steel ring before wearing	98.76	0.48	0.00
Steel ring worn against EP	98.55	0.42	0.21
Steel ring worn against nano-Si_3N_4/EP (0.52 vol%)	96.77	2.46	0.42
Steel ring worn against Si_3N_4-g-PGMA/EP (0.52 vol%, γ_g: 7.25%)	98.73	0.51	0.54

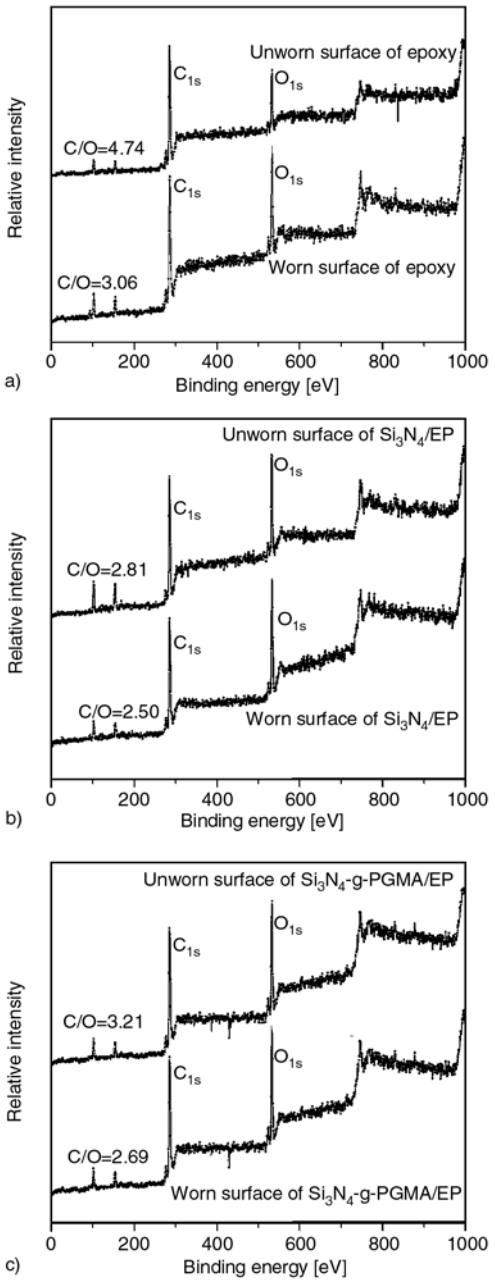

Figure 10. Low resolution XPS spectra of pin surface of (a) epoxy, (b) Si_3N_4/EP (0.79 vol%) and (c) Si_3N_4-g-PGMA/EP (0.79 vol%, γ_g: 7.25%)

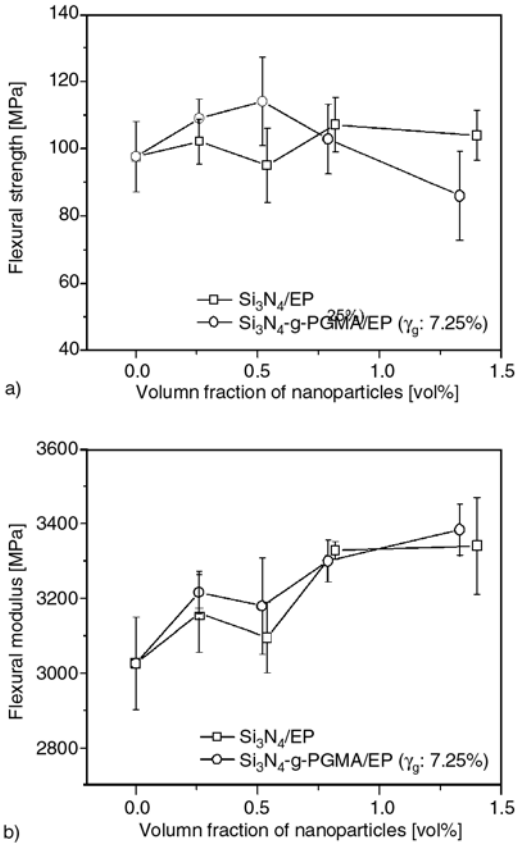

Figure 11. Flexural strengths and modulus of (a) Si_3N_4/EP and (b) Si_3N_4-g-PGMA/EP (γ_g: 7.25%) composites as a function of filler concentration

and nano-Si_3N_4/epoxy composites before and after the wear tests reveal that the atomic ratios of C/O have changed (Figure 10). The decrease of C/O ratios is indicative of oxidation of epoxy surface during wearing process. Incorporation of nano-Si_3N_4 and Si_3N_4-g-PGMA particles increases the resistance of epoxy against oxidation.

The addition of either untreated nano-Si_3N_4 or grafted nano-Si_3N_4 could enhance the flexural strength and modulus of epoxy (Figure 11), which can be easily explained by the high hardness of the particles. The composites with Si_3N_4-g-PGMA particles possess high flexural performance, especially at low filler content. The graft treatment of the nano-Si_3N_4 particles by PGMA ensures good filler-matrix bonding and favors stress transfer across interface.

4. Conclusions

1. Grafting of GMA onto nano-Si_3N_4 increased the interfacial interaction between the particles and the epoxy matrix through chemical bonding. It proved to be an effective way to further enhance the nano-effect of the nanoparticles on the improvements of the tribological performance. However, excessive GMA groups are detrimental to the enhancement of wear resistance of the composites due to molecule entanglement.
2. Compared with the unfilled and nano-Si_3N_4 filled epoxy, the epoxy filled with low content Si_3N_4-g-PGMA exhibited lower friction coefficient and higher wear rate. However, the friction and wear of the filled epoxy composites deteriorated with further increasing content of nano-Si_3N_4 and Si_3N_4-g-PGMA particles.
3. The technical route proposed by the authors is not limited to the system made of Si_3N_4 nanoparticles and epoxy resin. In fact, the surface treatment method presented in this paper is also feasible for various inorganic/polymer composites aiming at improving particle dispersion and interface interaction.

References

[1] Ng C. B., Schadler L. S., Siegel R. W.: Synthesis and mechanical properties of TiO_2-epoxy nanocomposites. Nanostructured Materials, **12**, 507–510 (1999). DOI: 10.1016/S0965-9773(99)00170-1

[2] Wetzel B., Haupert F., Zhang M. Q.: Epoxy nanocomposites with high mechanical and tribological performance. Composites Science and Technology, **63**, 2055–2067 (2003). DOI: 10.1016/S0266-3538(03)00115-5

[3] Sawyer W. G., Freudenberg K. D., Bhimaraj P.: A study on the friction and wear behavior of PTFE filled with alumina nanoparticles. Wear, **254**, 573–580 (2003). DOI: 10.1016/S0043-1648(03)00252-7

[4] Chang L., Zhang Z., Breidt C., Friedrich K.: Tribological properties of epoxy nanocomposites: I. Enhancement of the wear resistance by nano-TiO_2 particles. Wear, **258**, 141–148 (2005). DOI: 10.1016/j.wear.2004.09.005

[5] Chang L., Zhang Z., Ye L., Friedrich K.: Tribological properties of epoxy nanocomposites III. Characteistics of transfer films. Wear, **262**, 699–706 (2007). DOI: 10.1016/j.wear.2006.08.002

[6] Geng Y., Liu M. Y., Li J., Shi X. M., Kim J. K.: Effects of surfactant treatment on mechanical and electrical properties of CNT/epoxy nanocomposites. Composites Part A: Applied Science and Manufacturing, **12**, 1876–1883 (2008). DOI: 10.1016/j.compositesa.2008.09.009

[7] Rosa M. C., Peter A. L., Parnia N.: Polymer encapsulation of surface-modified carbon blacks using surfactant-free emulsion polymerization. Polymer, **48**, 2554–2563 (2007).
DOI: 10.1016/j.polymer.2007.02.063

[8] Vassileva E., Friedrich K.: Epoxy/alumina nanoparticle composites. II. Influence of silane coupling agent treatment on mechanical performance and wear resistance. Journal of Applied Polymer Science, **101**, 4410–4417 (2006).
DOI: 10.1002/app.23297

[9] Chand N., Dwived U. K.: Effect of coupling agent on abrasive wear behaviour of chopped jute fiber-reinforced polypropylene composites. Wear, **261**, 1057–1063 (2006).
DOI: 10.1016/j.wear.2006.01.039

[10] Espiard Ph., Guyot A.: Poly(ethyl acrylate) latexs encapsulating nanoparticles of silica: 2. Grafting process onto silica. Polymer, **23**, 4391–4395 (1995).
DOI: 10.1016/0032-3861(95)96844-X

[11] Sondi I.: Encapsulation of nanosized silica by in situ polymerization of *tert*-butyl acrylate monomer. Langmuir, **16**, 9031–9034 (2000).
DOI: 10.1021/la000618m

[12] Rong M. Z., Zhang M. Q., Zheng Y. X., Zeng H. M., Walter R., Friedrich K.: Structure-property relationship of irradiation grafted nano-inorganic particle filled polypropylene composites. Polymer, **42**, 167–183 (2001).
DOI: 10.1016/S0032-3861(00)00325-6

[13] Zhang M. Q., Rong M. Z., Yu S. L.: Effect of particle surface treatment on the tribological performance of epoxy based nanocomposites. Wear, **253**, 1086–1093 (2002).
DOI: 10.1016/S0043-1648(02)00252-1

[14] Ueda J., Yamaguchi H., Yamaguchi T., Tsubokawa N.: Radical graft polymerization of vinyl monomers onto nanoparticles in ionic liquid initiated by azo groups introduced onto the surface. Journal of Polymer Science Part A: Polymer Chemistry, **6**, 1143–1149 (2007).
DOI: 10.1002/pola.21879

[15] Rong M. Z., Zhang M. Q., Shi G.: Graft polymerization onto inorganic nanoparticles and its effect on tribological performance improvement of polymer composites. Tribology International, **36**, 697–707 (2003).
DOI: 10.1016/S0301-679X(03)00029-X

[16] Ji Q. L., Zhang M. Q., Rong M. Z., Wetzel B., Friedrich K.: Tribological properties of surface modified nano-alumina/epoxy composites. Journal of Materials Science, **39**, 6487–6493 (2004).
DOI: 10.1023/B:JMSC.0000044887.27884.1e

[17] Luo Y., Rong M. Z., Zhang M. Q.: Covalently connecting nanoparticles with epoxy matrix and its effect on the improvement of tribological performance of the composites. Polymers and Polymer Composites, **13**, 245–252 (2005).

[18] Luo Y., Rong M. Z., Zhang M. Q.: Tribological behavior of epoxy composites containing reactive SiC nanoparticles. Journal of Applied Polymer Science, **104**, 2608–2619 (2007).
DOI: 10.1002/app.24414

[19] Guo Q. B., Rong M. Z., Jia G. L., Lauc K. T., Zhang M. Q.: Sliding wear performance of nano-SiO_2/short carbon fiber/epoxy hybrid composites. Wear, **266**, 658–665 (2009).
DOI: 10.1016/j.wear.2008.08.005

[20] Luo Y., Rong M. Z., Zhang M. Q., Friedrich K.: Surface functionalization of Si_3N_4 nanoparticles by graft polymerization of glycidyl methacrylate and styrene. Journal of Applied Polymer Science, **102**, 992–999 (2006).
DOI: 10.1002/app.24011

[21] Wu C. L., Zhang M. Q., Rong M. Z., Friedrich K.: Tensile performance improvement of low nanoparticles filled-polypropylene composites. Composites Science and Technology, **62**, 10–11 (2002).
DOI: 10.1016/S0266-3538(02)00079-9

eXPRESS Polymer Letters Vol.4, No.3 (2010) 141–152
Available online at www.expresspolymlett.com
DOI: 10.3144/expresspolymlett.2010.19

Non-isothermal crystallization kinetics of partially miscible ethylene-vinyl acetate copolymer/low density polyethylene blends

J. Jin, S. J. Chen, J. Zhang[1]

Department of Polymer Science and Engineering, College of Materials Science and Engineering, Nanjing University of Technology, Nanjing 210009, People's Republic of China

Received 25 October 2009; accepted in revised form 16 December 2009

Abstract. The non-isothermal crystallization kinetics of ethylene-vinyl acetate copolymer (EVA, 14 wt% vinyl acetate content), low density polyethylene (LDPE) and their binary blends with different blending ratio were investigated via differential scanning calorimetry. Jeziorny theory and Mo's method were utilized in evaluating the crystallization behavior of both neat materials successfully. In the primary crystallization stage both EVA and LDPE had three-dimensional spherulitic growth mechanism. Apparently the crystallization rate of LDPE was faster than that of EVA at a low cooling rate. Increase in cooling rate limited the spherulites' growth, which narrowed their rate difference. Influences from blending on the crystallization kinetics of each component in EVA/LDPE mixture were evaluated by Kissinger's activation energy (ΔE) and Khanna's crystallization rate coefficient (*CRC*). Inter-molecular interaction in the melt increased the ΔE of both EVA and LDPE components at the beginning of cooling. During the primary crystallization stage of LDPE, dilution effect from EVA facilitated the crystal growth in LDPE. Co-crystallization between EVA component and the secondary crystallization stage of LDPE component also increased the *CRC* of EVA. In blend of EVA/LDPE = 7/3, LDPE obtained the maximal *CRC* value of 174.2 h^{-1}. Results obtained from various approaches accorded well with each other, which insured the rationality of conclusion.

Keywords: *thermal properties, ethylene-vinyl acetate copolymer, low density polyethylene, polymer blend, non-isothermal crystallization kinetics*

1. Introduction

Ethylene-vinyl acetate copolymer (EVA) has good transparency, flexibility and good oxygen barrier properties [1]. Blending EVA with low density polyethylene (LDPE) could increase the elasticity of material, and optimize its combination with inorganic materials [2]. It is an economical and efficient alternative to the development of new polymer materials [3–5]. The crystallizable units in both EVA and LDPE are ethylene chain segments [6]. To EVA, polar vinyl-acetate units (VAc) are introduced randomly into the backbone of copolymer, acting as intervals of ethylene chain segments with various lengths. As for LDPE, the short branches could also hinder its crystallization behavior while chains arranging into lattices. This could lead to multiple crystallization stages based on complex thermal history. Regarding their binary blends, the partial miscibility has been studied in our previous works via isothermal crystallization [7]. However, their crystallization under non-isothermal conditions would be more complicated than the ideal isothermal situation. This is of importance both in theoretical research and industrial manufacturing fields. Influences from cooling rate, heat transmission lags and thermal gradients within samples

*Corresponding author, e-mail: zhangjun@njut.edu.cn

must be taken into account, which are all vital factors referring to the overall crystallization properties of polymer.

Non-isothermal crystallization study via differential scanning calorimetry (DSC) provides not only a good controlled and reproducible procedure, but also an access to the quantitative analysis of crystallization kinetics. Many widely used kinetic models such as Jeziorny theory [8], Ziabicki theory [9], Ozawa model [10] and Mo's method [11, 12], which were mostly derived from the classical Avrami equation in isothermal condition, have been successfully performed in many single polymers, polymer blends and composites. For instance, Shi studied the influence of VAc content on the crystallization rate of single EVA [13]; non-isothermal crystallization kinetics of PP/EVA blends were reported by Goodarzi *et al.* [14]; Li *et al.* [15] also researched the nucleation effect of inorganic fillers in EVA/carbon nanotube composites. However, the non-isothermal crystallization kinetics studies in EVA/LDPE binary mixtures were rarely reported. Their partial miscibility resulted in apparent overlaps of exotherms during cooling process. Their asymmetric figures also restricted the fitting accuracy of peak separation. It was inappropriate to obtain the separate enthalpy integration of each component for further calculation. A model with a parameter of crystallization rate coefficient (*CRC*) proposed by Khanna [16] could be utilized.

In this work, the non-isothermal crystallization kinetics and the subsequent melting of neat EVA, LDPE, and their binary blends with various ratios were studied via Jeziorny theory and Mo's method. Influences from their partial miscibility on the crystallization behavior and mechanism of each component in blends were investigated by Kissinger's activation energy and Khanna's *CRC* model, respectively.

2. Experimental

2.1. Materials

Ethylene-vinyl acetate copolymer with 14 wt% VAc (EVA 14-2) was supplied by Beijing Organic Chemistry Plant, Beijing, China; the melting flow rate (MFR) is 2.0 g/10 min, the density is 0.94 g/cm^3. Low density polyethylene (LDPE 2426H) was obtained from BASF-YPC Co. Ltd., Nanjing, China. Its MFR is 2.0 g/10 min, the density is about 0.92~0.93 g/cm^3.

2.2. Preparation of blends

Blends of EVA/LPDE with various ratios were prepared in a 60 ml Rheomix internal mixer (Shanghai Kechuang XSS-300, China); the melt compounding was performed at 135°C for 10 min; the rotor speed is 30 rpm and the total mixing weight was about 50 g per batch. Samples were designated as EVA, EVA/LDPE = 7/3, EVA/LDPE = 5/5, EVA/LDPE = 3/7 and LDPE for various EVA mass ratios in blend, respectively.

2.3. Differential scanning calorimetry

The non-isothermal crystallization and the subsequent melting behaviors were carried out by a differential scanning calorimeter (TA Q200, USA). Samples weighing about 10 mg were cut off for characterization. Nitrogen purge gas with a flux of 50 ml/min was used to prevent thermal degradation of samples during scanning. In order to eliminate residual volatile impurities and the small crystals, all samples were first quickly heated (at 40°C/min) up to 150°C and held isothermally for 3 minutes. Then they were cooled down from melt to 0°C at five different cooling rates: 2.5, 5, 10, 15 and 20°C/min, respectively. The subsequent melting process after each step of non-isothermal cooling was executed by heating run from 0 to 150°C at a constant rate of 10°C/min.

3. Results and discussion

3.1. Non-isothermal crystallization

Figure 1 illustrates the non-isothermal cooling traces of all samples. Molecular chain segments crystallized slower than the continuous temperature dropping. And their movability degenerated at a lower ambient temperature. Such lag between them was magnified under a higher cooling rate [17]. Exothermic peaks exhibited broader figure and shifted gradually to a lower temperature. Multiple exothermic characteristics were observed both in neat EVA and LDPE: a sharp major exothermic peak followed by a following broad peak/shoulder with apparent lagging tail. For EVA, the randomly

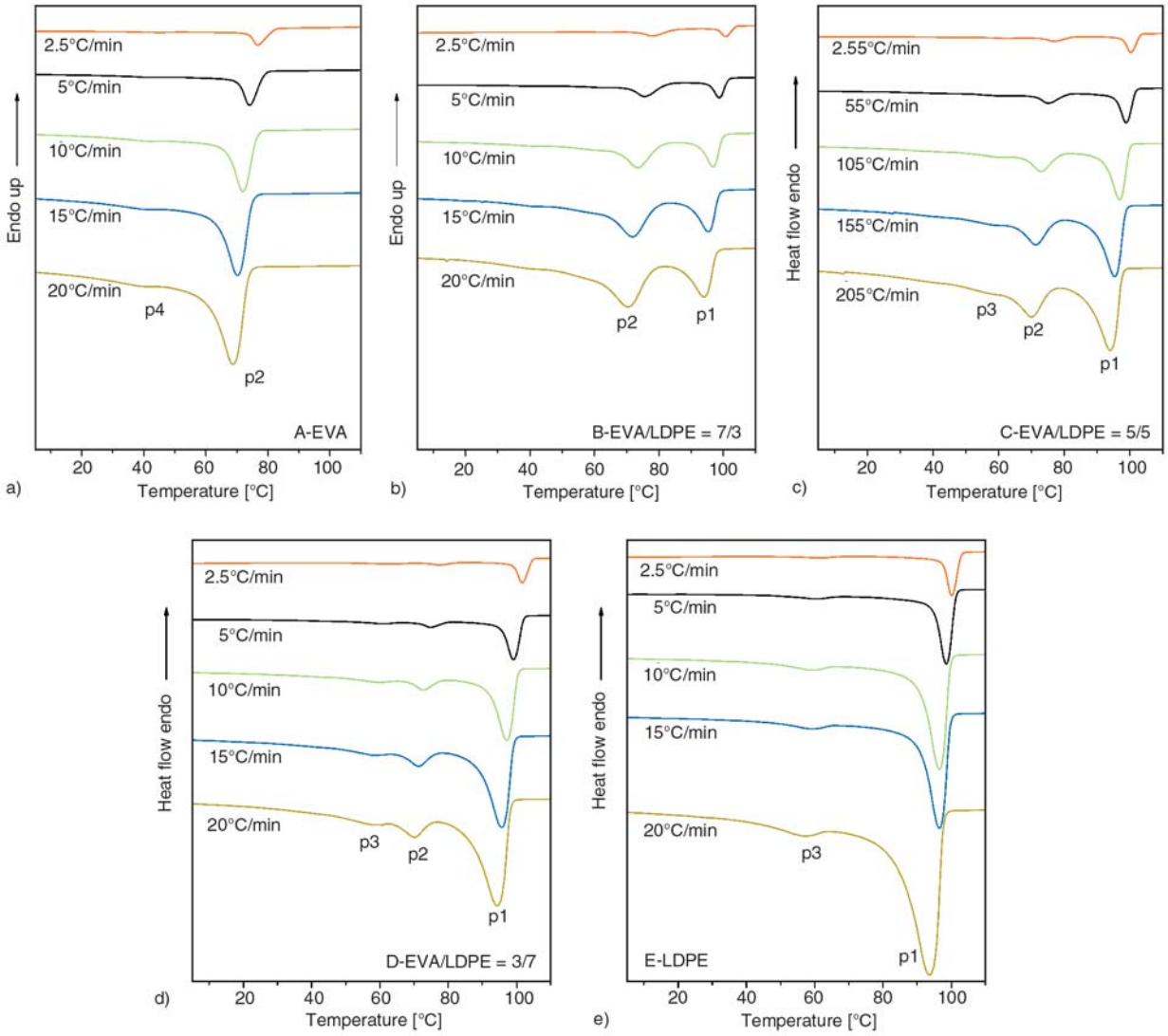

Figure 1. Non-isothermal crystallization exotherms of blends at different cooling rate (A-EVA, B-EVA/LDPE = 7/3, C-EVA/LDPE = 5/5, D-EVA/LDPE = 3/7, E-LDPE)

introduced VAc units acted as the interval in the backbone of copolymer, which fractionated ethylene chain segments by various crystallizable lengths [18]. The major exothermic peak represented the fusion of lamellae arranged by a portion of chain segments of the highest crystallizablity, indicating the primary crystallization stage. While those defective chain segments were repelled to the surface of the existing crystal. They were forced to crystallize under a lower temperature later with more deficiency during arrangement, thus formed the secondary crystallization region [7]. It has been widely accepted that the short ethylene branches in LDPE could inhibit its overall crystallization behavior [19]. Similar molecular fractionation and secondary crystallization stage during non-isothermal crystallization were even more remarkable in neat LDPE. In traces of blends, the peak of EVA component overlapped partially with LDPE component. The secondary crystallization shoulder in EVA component became imperceptible in all blends; the secondary crystallization peak of LDPE component was also affected. As the LDPE ratio increased in blends, its exotherms grew to a larger and sharper figure.

3.1.1. Non-isothermal crystallization of neat materials

The non-isothermal crystallization kinetics of neat EVA and LDPE were first studied. Data in Table 1 show that the onset crystallization temperature (T_c^{on}) of LDPE was about 20°C higher than that of EVA. The secondary crystallization peak tempera-

Table 1. Non-isothermal crystallization data of neat EVA and LDPE

Sample	D [°C/min]	T_c^f [°C]	T_c^{p4} [°C]	T_c^{p3} [°C]	T_c^{p2} [°C]	T_c^{p1} [°C]	T_c^{on} [°C]	ΔT_c [°C]	ΔH_c [J/g]
EVA	2.5	30.7	44.0	–	75.6	–	81.1	50.4	79.2
	5.0	28.7	43.2	–	74.1	–	78.8	50.1	77.3
	10.0	28.5	42.1	–	71.9	–	76.4	48.0	75.2
	15.0	26.7	41.8	–	70.3	–	74.9	48.2	73.8
	20.0	25.4	39.5	–	68.7	–	73.7	48.3	72.6
LDPE	2.5	50.9	–	61.3	–	100.1	102.8	51.9	123.7
	5.0	49.2	–	60.3	–	98.5	101.3	52.1	124.2
	10.0	46.0	–	59.0	–	96.5	99.7	53.7	129.3
	15.0	44.4	–	58.2	–	95.0	98.5	54.1	118.4
	20.0	41.3	–	57.2	–	93.6	97.6	56.3	125.7

D: cooling rate; T_c^{on}: onset crystallization temperature; T_c^{p1}: peak crystallization temperature of the primary crystallization in LDPE; T_c^{p2}: peak crystallization temperature of primary crystallization in EVA; T_c^{p3}: peak crystallization temperature of secondary crystallization in LDPE; T_c^{p4}: peak crystallization temperature of secondary crystallization in EVA; T_c^f: final crystallization temperature; $\Delta T_c = T_c^{on} - T_c^f$; ΔH_c: crystallization enthalpy of polymer

ture (T_c^{p3}) of LDPE was about 17°C higher than the corresponding parameter of EVA (T_c^{p4}). The crystallization enthalpy (ΔH_c) of EVA decreased slightly along with the increase in cooling rate.

A-Jeziorny theory

The classical Avrami equation [20–22] relates to the amount or fraction of un-crystallized material that remains after time *t*, which has been commonly utilized in describing isothermal crystallization kinetics of polymer. It is given by Equation (1):

$$1 - X_t = \exp(-Z_t t^n) \tag{1}$$

where Z_t is the crystallization rate constant, which involves the contribution from both nucleation and crystal growth. *n* represents the Avrami exponent, representing the mechanism and dimensional geometry of crystal growth. X_t stands for the relative crystallinity, which is set as a function of time *t* according to Equation (2):

$$X_t = \frac{\int_{t_0}^{t} \left(\frac{dH_c}{dt}\right) dt}{\int_{t_0}^{t_\infty} \left(\frac{dH_c}{dt}\right) dt} \cdot 100\% \tag{2}$$

where t_0 and t_∞ mean the onset and completion time of the specific crystallization stage, respectively. dH_c is the enthalpy of the crystallization released during an infinitesimal time range d*t*. In this experiment, for a chosen cooling rate, the heat flow integration of relative crystallinity calculation can be firstly recorded as a function of temperature *T* [23], see Equation (3):

$$X_T = \frac{\int_{T_0}^{T} \left(\frac{dH_c}{dT}\right) dT}{\int_{T_0}^{T_\infty} \left(\frac{dH_c}{dT}\right) dT} \cdot 100\% \tag{3}$$

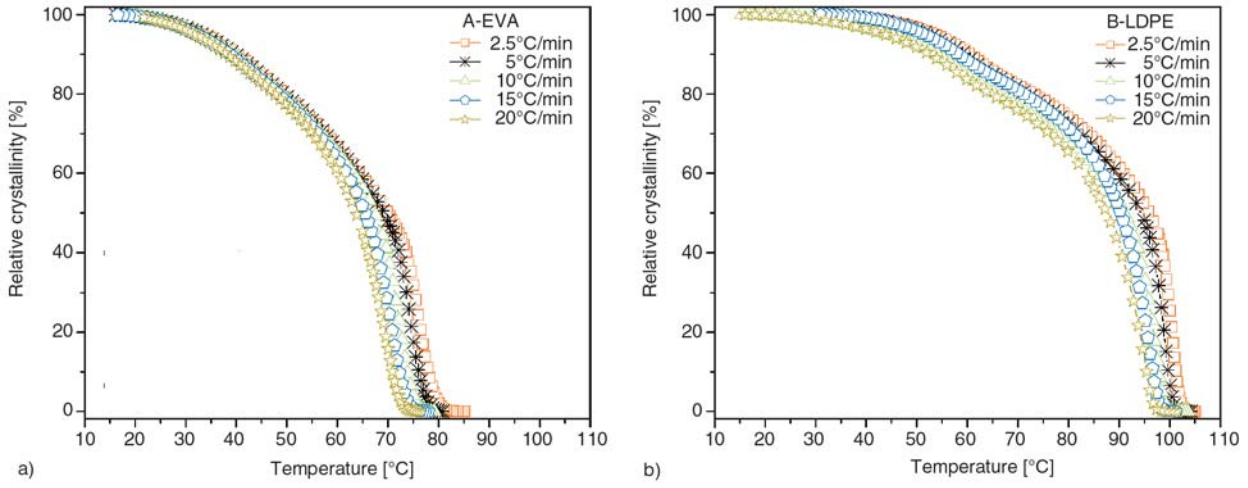

Figure 2. Plots of X_t versus *T* for neat EVA and LDPE during non-isothermal crystallization stage (A-EVA, B-LDPE)

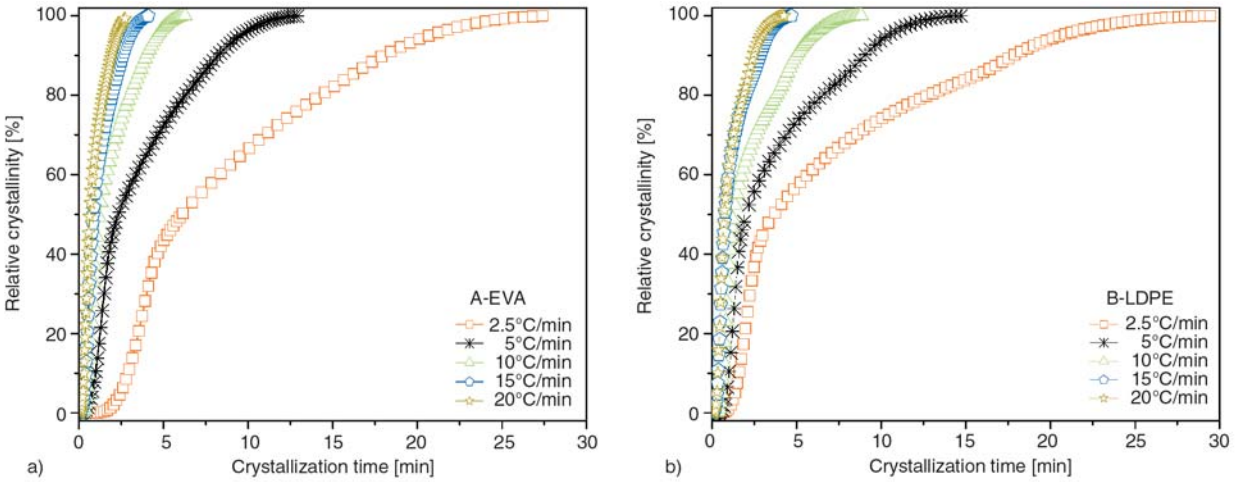

Figure 3. Plots of X_t versus t for neat EVA and LDPE during non-isothermal crystallization stage (A-EVA, B-LDPE)

T_0 and T_∞ in Equation (3) are the onset and completion temperature of the crystallization stage, respectively. Figure 2 illustrates the development of the relative crystallinity to T of two neat materials at varying cooling rate.

The T-axis can be transformed into the t-axis as shown in Figure 3. Crystallization time can be calculated from the following Equation (4), in which the D stands for the cooling rate (2.5, 5, 10, 15 and 20°C/min, respectively):

$$t = \frac{|T_0 - T|}{D} \tag{4}$$

In the primary crystallization, relative crystallinity increases acutely along with t. The half crystallization time $t_{1/2}$, representing the time needed to achieve 50% of the entire crystallization progress, keeps lower than 5 min in all cases. However, after X_t overreached about 40%, the secondary crystallization stage of EVA and LDPE began. It took much longer time to complete the overall crystallization stage. Such characteristic was also reported in crystallization kinetics of metallocene polyethylene [24].

The double-logarithmic form of the Equation (1) is given by Equation (5):

$$\log[-\ln(1 - X_t)] = \log Z_t + n \log(t) \tag{5}$$

Plotting $\log[-\ln(1-X_t)]$ against $\log(t)$ for each D, the primary linear section obtained from Equation (5) enables one to obtain the Avrami exponent n and the crystallization rate constant Z_t from the slope and the intercept, respectively. Considering the influence from continuously changing temperature in the non-isothermal crystallization, parameters do not have the same physical meaning as in the iso-thermal situation. Z_t should be corrected for the non-isothermal situation by Equation (6):

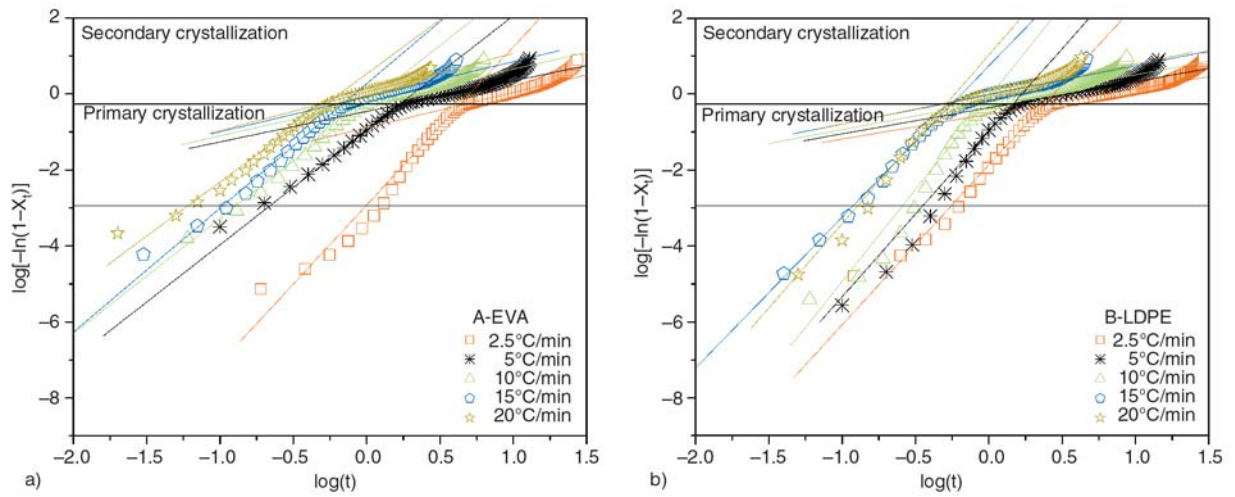

Figure 4. Plots of $\log[-\ln(1-X_t)]$ versus $\log(t)$ for EVA and LDPE as received at various cooling rate (A-EVA, B-LDPE)

Table 2. Data from Jeziorny theory in non-isothermal crystallization kinetic analysis

Sample	D [°C/min]	Primary crystallization			Secondary crystallization		$t_{1/2}$ [min]
		Z_c [min^{-1}]	n	Adj. R^2	n'	Adj. R^2	
EVA	2.5	0.06	4.52	0.9960	0.93	0.9996	6.10
	5.0	0.64	3.01	0.9998	0.79	0.9997	2.34
	10.0	0.96	3.40	0.9986	0.87	0.9995	1.21
	15.0	1.05	3.40	0.9928	0.94	0.9994	0.85
	20.0	1.07	2.98	0.9907	0.96	0.9993	0.66
LDPE	2.5	0.16	4.80	0.9989	0.67	0.9997	3.67
	5.0	0.66	5.79	0.9983	0.69	0.9998	2.00
	10.0	1.08	6.57	0.9978	0.75	0.9974	1.29
	15.0	1.20	4.79	0.9919	0.76	0.9994	0.85
	20.0	1.25	5.99	0.9918	0.77	0.9994	0.73

D: cooling rate; Z_c: non-isothermal crystallization rate constant modified by Jeziorny; *n*: Avrami index in the primary crystallization stage; *n*': Avrami index in the secondary crystallization stage; $t_{1/2}$: half crystallization time; *Adj.* R^2: adjust R^2 of plots fitting

$$\ln Z_c = \frac{\ln Z_t}{D} \tag{6}$$

Z_c was modified by Jeziorny [8] in Equation (6), which stands for the non-isothermal crystallization rate constant. And *n* is designated as the apparent Avrami exponent.

Figure 4 exhibites plots of $\log[-\ln(1-X_t)]$ against $\log(t)$ of neat EVA and LDPE, respectively. Plots above could be separated into three stages along with $\log(t)$: the nucleation process, the primary crystallization stage and the secondary crystallization stage. The primary crystallization showed approximately linear shape. In the secondary crystallization stage, all plots deviated from the former direction, and exhibited another approximately linear shape with gentley slopes.

The values of Z_c, *n* and $t_{1/2}$ in EVA and LDPE were listed in Table 2. Good linear fitting results of both the primary and secondary crystallization are obtained (*Adj*. $R^2 > 0.99$). In the 2.5°C/min cooling case, the Z_c of the primary crystallization stage in LDPE (0.16 min^{-1}) was much higher than that in EVA (0.06 min^{-1}). Increase in cooling rate limited the further spherulites' growth, which narrowed the rate difference between EVA and LDPE. Similar shrinking tendency was also observed in $t_{1/2}$. When beeing cooled at a rate of 20°C/min, $t_{1/2}$ of EVA was even lower than LDPE. It has been accepted that, a high ambient temperature would inhibit the nucleation but facilitate the crystal growth of polymer molecules. While a low temperature environment could have contrary influences on crystallization behaviors [7, 25, 26]. Intense cooling rate has limited the time needed for a sufficient primary crystallization growth. More crystallizable chain segments were forced to form the secondary crystallization at the end of a rapid cooling.

Values of *n* implied both EVA and LDPE had homogenous random nucleation followed by three-dimensional spherulitic growth in a spherical form. *n* at various cooling rates arranged between 2.98~4.52 in EVA and 4.80~5.99 in LDPE, respectively. LDPE had a higher dimensionality of crystal growth than EVA. Non-integral *n* value >4 was considered as a result of nucleation rate increasing during interface controlled growth [27]. Crystallization mechanism in the secondary stage is also analyzed. Corresponding apparent *n*' of EVA varied from 0.93~0.96, and the value of LDPE slightly fluctuates within 0.67~0.77. This referred to a thickening of long cylinders or large lamellae after the spherulites' impingement [27]. The secondary crystallization stage took place in a more restricted surrounding, which needed much longer time than the primary stage. The slow secondary crystallization is positive to the perfecting of the overall crystallization behavior. That is why the annealing treatment during practical manufacturing has positive influence on the final properties of products.

B-Mo's method

Mo's method [11, 12, 28–30] is another efficient approach derived from the combination of both Avrami equation and Ozawa model [10], which have been successfully utilized in various cases [29, 31, 32]. Dividing the Avrami equation by the Ozawa's equation, functions are given in Equations (7) and (8):

$$\log Z_t + n\log(t) = \log K(T) - m\log(D) \tag{7}$$

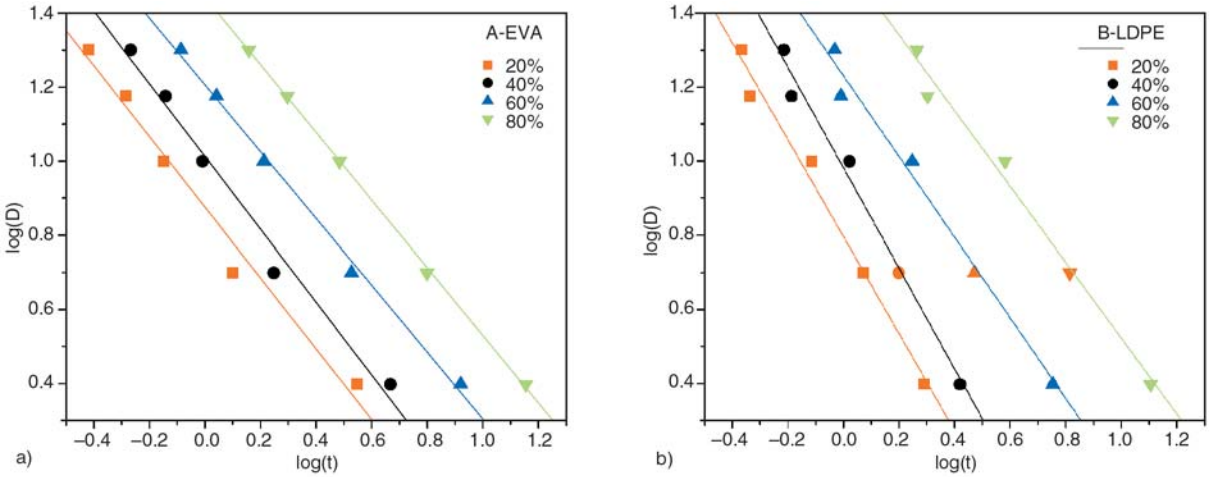

Figure 5. Plots of log(D) versus log(t) for neat EVA and LDPE during the non-isothermal crystallization (A-EVA, B-LDPE)

$$\log(D) = \frac{1}{m}\log\left[\frac{K(T)}{Z_t}\right] - \left(\frac{n}{m}\right)\log(t) \tag{8}$$

Parameter $F(T)$ is assumed as $F(T) = [K(T)\cdot Z_t^{-1}]^{1/m}$. It is denoted as the value of a cooling rate which has to be chosen at a unit crystallization time when the measured sample amounts to a certain degree of crystallinity. a refers to the ratio of Avrami exponent n to the Ozawa exponent m. The final form of Mo's method is obtained as Equation (9):

$$\log(D) = \log[F(T)] - a\log(t) \tag{9}$$

A good linear fitting was obtained by plotting log(D) against log(t) as shown in Figure 5. The intercept and slope represent $F(T)$ and a, respectively, which were listed in Table 3. The value of $F(T)$ increased monotonically with the increasing relative crystallinity, implying that under the same time unit, a larger cooling rate was needed in order to obtain a higher X_t. $F(T)$ accorded well with results from Jeziorny theory. It was suggested that only the primary crystallization stage accounted for the first 20% crystallization behavior. However, LDPE needed a more intense undercooling condition than EVA to reach the higher X_t = 80%. It was the accumulation of both the primary and secondary crystallization stages to obtain a higher X_t. This suggested that the secondary crystallization in LDPE accounted for comparatively larger contribution to the entirety, or it was slower than in EVA.

Table 3. Data from Mo's method in non-isothermal crystallization kinetic analysis

Sample	X_t [%]	F(T)	*a*
EVA	20	7.51(0.03)*	0.95(0.08)
	40	10.29(0.02)	0.98(0.07)
	60	16.09(0.02)	0.90(0.03)
	80	27.73(0.01)	0.91(0.01)
LDPE	20	6.24(0.02)	1.30(0.09)
	40	9.54(0.02)	1.28(0.09)
	60	16.94(0.03)	1.03(0.07)
	80	35.19(0.05)	0.98(0.07)

X_t:given relative crystallinity; $F(T)$: non-isothermal crystallization rate parameter from Mo's method; a: slop of plots in Figure 5 (the ratio of Avrami exponent n to the Ozawa exponent m)
*standard error

3.1.2. Non-isothermal crystallization of blends

It is accepted that, like LDPE, crystallizable chain segments in EVA are also continuous ethylene chain segments with different lengths [18, 33]. As shown in Figure 1, overlapping of exotherms widely existed in blending situation, which was mostly due to the partial miscibility [7] between EVA and LDPE. Both widely used Jeziorny theory and Mo's method suitable for neat polymers, are based on the exothermic enthalpy integration of single exothermic peak. Peak separation, enthalpy integration and fitting would bring inevitable errors in analysis crystallization kinetics. However, variation in the major peak position of each component at EVA/LDPE blends with different ratios indicated their changes in crystallization behaviors under a given crystallization condition. Kinetics information can be investigated via other appropriate approaches, which can avoid the influences from peak overlapping in exotherms.

A-Apparent activation energy

The apparent activation energy of each component of blends in non-isothermal crystallization was evaluated via Kisinger's method [34]. Considering influences from cooling rate, the apparent activation energy ΔE could be determined by Equation (10):

$$\frac{d\left[\ln\left(\frac{D}{T_c^{p2}}\right)\right]}{d\left(\frac{1}{T_c^p}\right)} = \frac{-\Delta E}{R} \tag{10}$$

where R is the universal gas constant, (8.314 J/(mol·K), T_c^p is the crystallization peak temperature of each polymer component in blends. D represents the cooling rate. It is suitable to kinetics studying situations even with exothermic peak overlapping. The good linear relation plot of $\ln(D/T_c^{p2})$ versus $1/T_c^p$ for EVA and LDPE component in blends were shown in Figure 6. As data listed in Table 4, after blending, the ΔE of both polymer components increased, which indicated the inter-molecular interaction at melt between EVA and LDPE would hinder the nucleation at the beginning of cooling process.

B-Crystallization rate coefficient

Another similar approach with a crystallization rate coefficient (*CRC*) parameter, proposed by Khanna [16], and Di Lorenzo and Silvestre [26] was also utilized in this work. As the polymer cooled from melt state (T_m), structures which have symmetrical and short repeating chain segments crystallize sooner than those with longer, unsymmetrical or branched repeating units. Khanna considered the cooling rate D dependence against the exothermic peak temperature T_c^p. It was proposed that, once the crystallization began, it could be hindered by a higher cooling rate. But the amount of hindrance would be the least for the fastest crystallizing polymer. By plotting the dependence of D [°C/min] against T_c^p [°C], the slope should have a larger value (absolute value) for one crystallized comparatively faster. *CRC* was finally defined as the $\Delta D/\Delta T_c^p$ [h^{-1}], representing the variation in cooling rate required for a 1°C-change in the under cooling of the polymer melt [26, 35].

As shown in Figure 7 and Table 5, *CRC* ranked the materials on a scale of crystallization rate. Blending affected the crystallization of EVA more significantly than LDPE. CRC of LDPE increased after blending since being blended with EVA, and

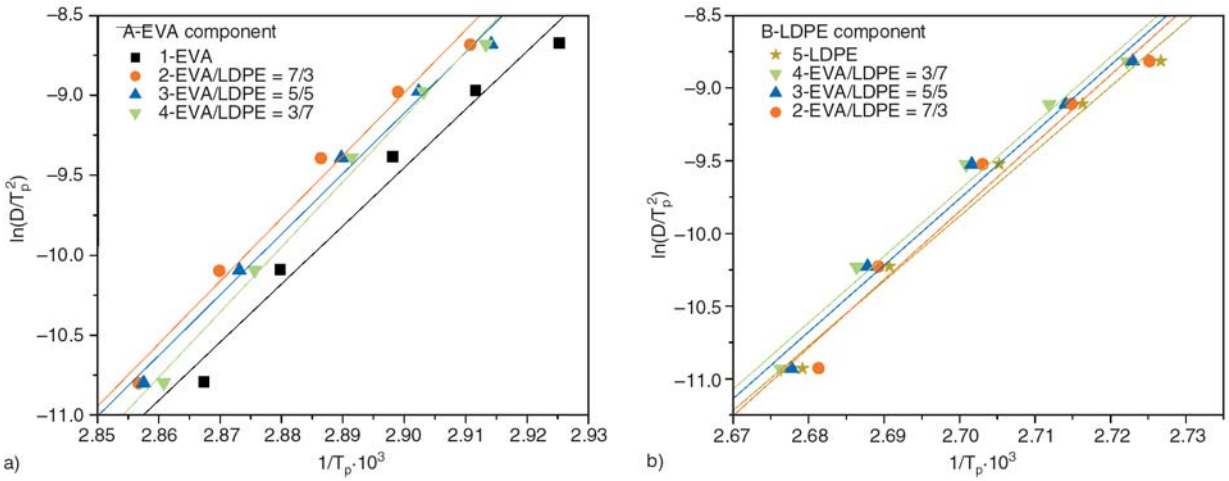

Figure 6. Plots of $\ln(D/T_c^{p2})$ versus $1/T_c^p$ for EVA and LDPE component in blends (A-EVA component, B-LDPE component)

Table 4. Apparent activation energy of EVA and LDPE components in blends

Component	ΔE [kJ/mol]				
	EVA	EVA/LDPE = 7/3	EVA/LDPE = 5/5	EVA/LDPE = 3/7	LDPE
EVA	302.2(0.9665)*	326.0(0.9769)	315.0(0.9852)	338.1(0.9895)	–
LDPE	–	389.6(0.9491)	381.4(0.9693)	379.7(0.9694)	370.7(0.9770)

*adjust $R^2$of plots fitting

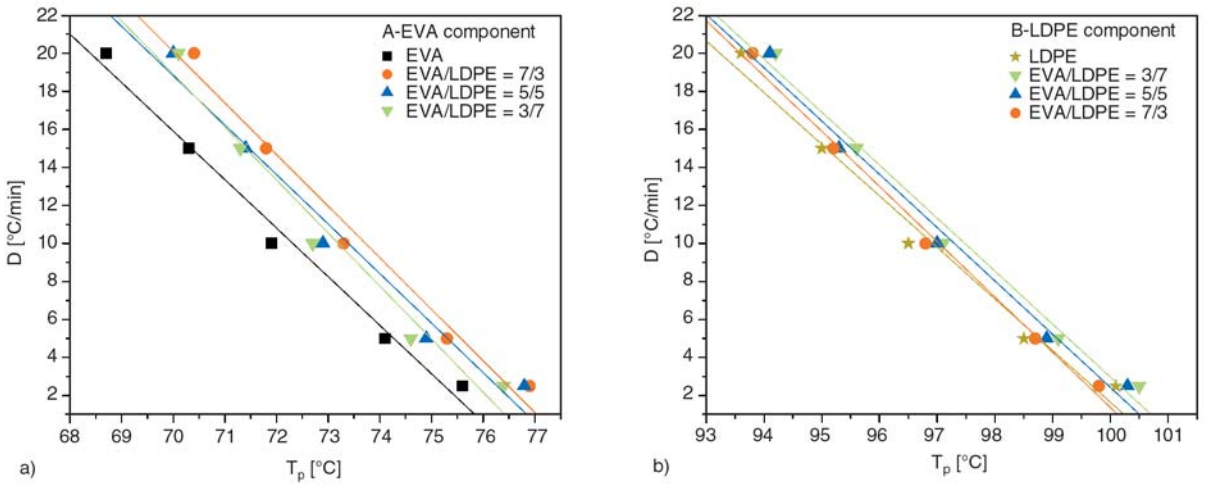

Figure 7. Plots of D versus T_c^p for EVA and LDPE component before and after blending (A-EVA component, B-LDPE component)

Table 5. Value of *CRC* for EVA and LDPE components in blends

Component	CRC [h^{-1}]				
	EVA	**EVA/LDPE = 7/3**	**EVA/LDPE = 5/5**	**EVA/LDPE = 3/7**	**LDPE**
EVA	153.0(0.9823)*	162.7(0.9733)	156.0(0.9605)	167.1(0.9538)	–
LDPE	–	174.3(0.9919)	168.0(0.9790)	167.2(0.9805)	162.7(0.9733)

*adjust R^2 of plots fitting

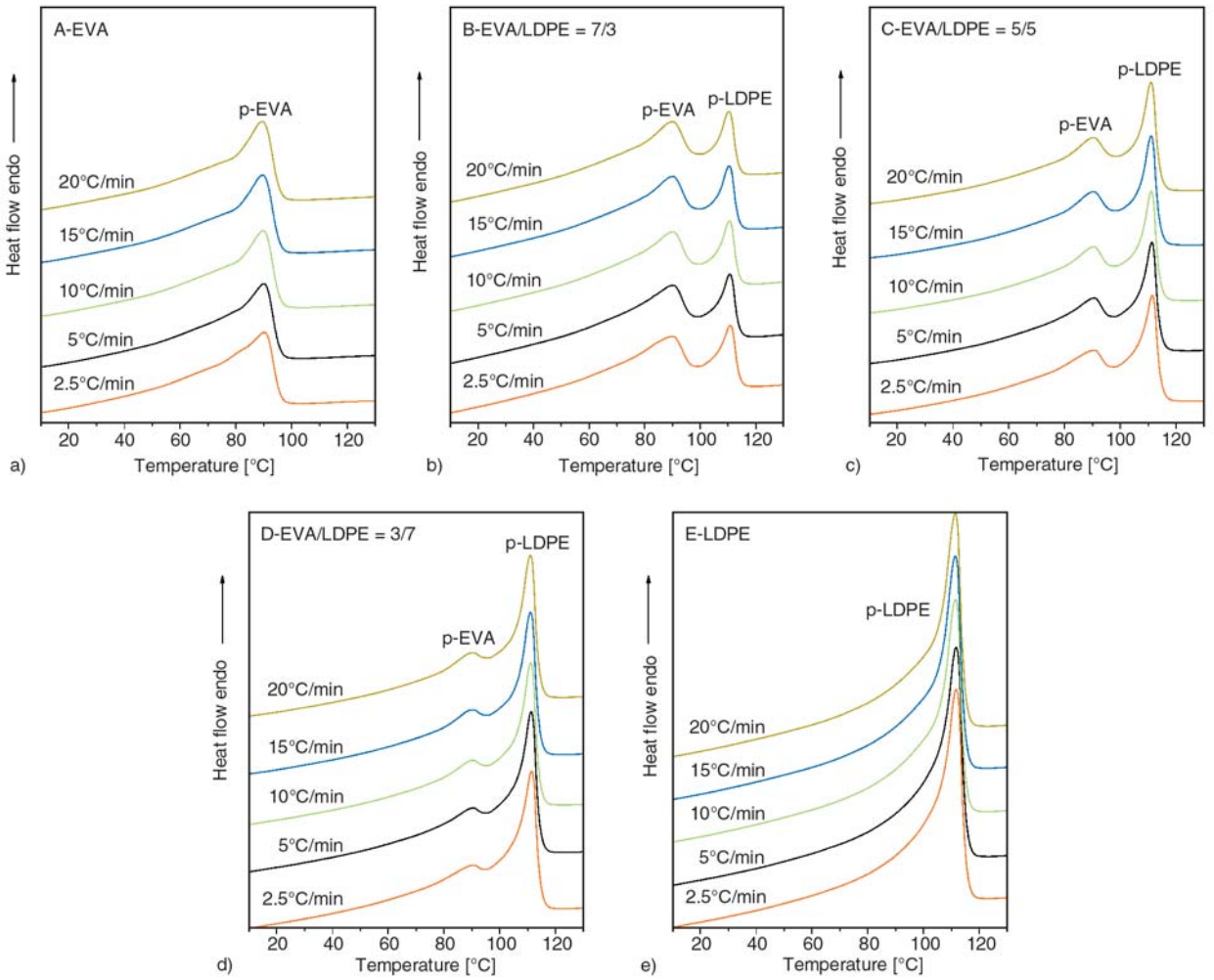

Figure 8. Subsequent melting endotherms of blends corresponding to different cooling rate (A-EVA, B-EVA/LDPE = 7/3, C-EVA/LDPE = 5/5, D-EVA/LDPE = 3/7, E-LDPE)

obtained its maximum (174.3 h^{-1}) in blend of EVA/LDPE = 7/3. Similar *CRC* growth in EVA component was also observed. The crystallizable units in both EVA and LDPE are symmetrical and short repeating ethylene chain segments. They were firstly randomly mixed in the melt. During the primary crystallization stage of LDPE, EVA is kept in the molten state; its dilution effect prevented the molecules of LDPE from self entanglement, which facilitated the crystal growth of LDPE. The short branches of LDPE were kept at amorphous state until a lower temperature. They formed the secondary crystallization of LDPE, which occurred simultaneously with the crystallization of EVA component as shown in Figures 1B, 1C, 1D. Their partial miscibility led to co-crystallization between two components, which also affected the crystallization rate of EVA component. In blend of EVA/LDPE = 7/3, the *CRC* of LDPE component had the maximum in all cases.

3.2. Subsequent melting

The subsequent melting traces of all samples are exhibited in Figure 8 and Table 6. The secondary crystallization in neat EVA and LDPE started to melt at a very low temperature, endothermic behavior grew up gradually and finally formed the major melting peak. This demonstrated that the secondary crystals were the aggregation of defective crystals with various completion degrees. This phenomenon was also confirmed in thermal traces of all blends.

The higher peak (p-LDPE) referred to the primary crystallization melting in LDPE component. While the secondary crystal melting of LDPE incorporated partially with the major melting of EVA component, which resulted in a much broader shape of p-EVA. The slight depression in T_m^{p-LDPE} and growth in T_m^{p-EVA} also affirmed the partial miscibility between EVA and LDPE. Overlaps in endotherms demonstrated the existence of co-crystallization between them.

Table 6. Subsequent melting data of all samples

Sample	Sub-heat after cooled at [°C/min]	$T_m^{p\text{-}EVA}$ [°C]	$T_m^{p\text{-}LDPE}$ [°C]	T_m^f [°C]	ΔH_m [J/g]
EVA	2.5	90.2	–	95.9	77.7
	5.0	89.9	–	95.7	77.1
	10.0	89.7	–	95.7	76.4
	15.0	89.6	–	95.7	76.0
	20.0	89.5	–	95.7	75.8
EVA/LDPE = 7/3	2.5	90.1	110.8	114.1	88.7
	5.0	90.3	110.7	113.9	87.3
	10.0	90.3	110.4	113.8	86.1
	15.0	90.2	110.4	113.7	86.4
	20.0	90.2	110.3	113.7	86.1
EVA/LDPE = 5/5	2.5	90.7	111.4	114.4	104.9
	5.0	90.7	111.2	114.2	104.4
	10.0	90.6	111.1	114.0	102.9
	15.0	90.5	110.9	114.1	102.1
	20.0	90.5	110.9	114.1	101.9
EVA/LDPE = 3/7	2.5	90.7	111.4	114.4	118.1
	5.0	90.7	111.3	114.2	116.3
	10.0	90.5	111.0	114.0	114.0
	15.0	90.5	111.0	114.0	113.7
	20.0	90.4	111.0	114.0	112.7
LDPE	2.5	–	111.6	115.0	133.6
	5.0	–	111.4	114.7	131.6
	10.0	–	111.4	114.7	130.8
	15.0	–	111.4	114.6	129.6
	20.0	–	111.2	114.6	130.2

$T_m^{p\text{-}EVA}$: the major melting peak temperature of EVA component in blends; $T_m^{p\text{-}LDPE}$: the major melting peak temperature of LDPE component in blends; T_m^f: final temperature of melting behavior; ΔH_m: melting endothermic enthalpy

4. Conclusions

The Jeziorny theory and Mo's method were successfully utilized to evaluate the crystallization rate of neat EVA and LDPE. In the primary crystallization stage, LDPE crystallized faster than EVA apparently. Along with the increasing in cooling rate, such rate differences shrank gradually for the lack of primary crystal growth time in polymer. The Avrami index n indicated that both polymers had homogeneous nucleation and crystallized in a three-dimensional spherulitic growth mechanism. LDPE had a higher dimensionality of crystal growth than EVA. $F(T)$ from Mo's method also revealed a tendency that accorded well with results from Jeziorny theory. Blending EVA with LDPE led to apparent overlaps of exotherms during cooling. Inter-molecular interaction between them in the melt increased the activation energy of crystallization at the beginning of cooling. During the primary crystallization stage of LDPE, the dilution effect of liquid EVA prevented the molecules of LDPE from self entanglement, which facilitated the crystal growth of LDPE. The short branches of LDPE kept at amorphous state until a lower temperature. They formed the secondary crystallization of LDPE, which occurred simultaneously with the crystallization behavior of EVA component. Their partial miscibility led to co-crystallization between two components, which also affected the crystallization rate of EVA component. In blend of EVA/LDPE = 7/3, the *CRC* of EVA was higher than that in the neat polymer, LDPE component obtained the maximal *CRC* value at 174.3 h^{-1}. The subsequent melting further demonstrated the partial miscibility and co-crystallization between EVA and LDPE components in blends.

References

[1] Takidis G., Bikiaris D. N., Papageorgiou G. Z., Achilias D. S., Sideridou I.: Compatibility of low-density polyethylene/poly(ethylene-co-vinyl acetate) binary blends prepared by melt mixing. Journal of Applied Polymer Science, **90**, 841–852 (2003).
DOI: 10.1002/app.12663

[2] Landete-Ruiz M. D., Martinez-Díez J. A., Rodríguez-Pérez M. A., De Saja J. A., Martin-Martinez J. M.: Improved adhesion of low-density polyethylene/EVA foams using different surface treatments. Journal of Adhesion Science and Technology, **16**, 1073–1101 (2002).
DOI: 10.1163/156856102760146174

[3] Rodríguez-Pérez M. A., Duijsens A., De-Saja J. A.: Effect of addition of EVA on the technical properties of extruded foam profiles of low-density polyethylene/EVA blends. Journal of Applied Polymer Science, **68**, 1237–1244 (1998).
DOI: 10.1002/(SICI)1097-4628(19980523)68:8<1237::AID-APP5>3.0.CO;2-E

[4] Borisova B., Kressler J.: Environmental stress-cracking resistance of LDPE/EVA blends. Macromolecular Materials and Engineering, **288**, 509–515 (2003).
DOI: 10.1002/mame.200390048

[5] Khonakdar H. A., Jafari S. H., Yavari A., Asadinezhad A., Wagenknecht U.: Rheology, morphology and estimation of interfacial tension of LDPE/EVA and HDPE/EVA blends. Polymer Bulletin, **54**, 75–84 (2005).
DOI: 10.1007/s00289-005-0365-6

[6] Moly K. A., Radusch H. J., Androsh R., Bhagawan S. S., Thomas S.: Nonisothermal crystallisation, melting behavior and wide angle X-ray scattering investigations on linear low density polyethylene (LLDPE)/ethylene vinyl acetate (EVA) blends: Effects of compatibilisation and dynamic crosslinking. European Polymer Journal, **41**, 1410–1419 (2005).
DOI: 10.1016/j.eurpolymj.2004.10.016

[7] Shi X. M., Jin J., Chen S. J., Zhang J.: Multiple melting and partial miscibility of ethylene-vinyl acetate copolymer/low density polyethylene blends. Journal of Applied Polymer Science, **113**, 2863–2871 (2009).
DOI: 10.1002/app.30271

[8] Jeziorny A.: Parameters characterizing the kinetics of the non-isothermal crystallization of poly(ethylene terephthalate) determined by d.s.c.. Polymer, **19**, 1142–1144 (1978).
DOI: 10.1016/0032-3861(78)90060-5

[9] Ziabicki A., Jarecki L.: Theoretical analysis of oriented and non-isothermal crystallization III. Kinetics of crystal orientation. Colloid and Polymer Science, **256**, 332–342 (1978).
DOI: 10.1007/BF01544326

[10] Ozawa T.: Kinetics of non-isothermal crystallization. Polymer, **12**, 150–158 (1971).
DOI: 10.1016/0032-3861(71)90041-3

[11] Ren M., Mo Z., Chen Q., Song J., Wang S., Zhang H., Zhao Q.: Crystallization kinetics and morphology of nylon 1212. Polymer, **45**, 3511–3518 (2004).
DOI: 10.1016/j.polymer.2004.03.027

[12] Song J., Ren M., Chen Q., Sun X., Zhang H., Song C., Zhang H., Mo Z.: Isothermal and nonisothermal crystallization kinetics of irradiated nylon 1212. Journal of Polymer Science Part B: Polymer Physics, **43**, 2326–2333 (2005).
DOI: 10.1002/polb.20447

[13] Shi X. M., Zhang J., Jin J., Chen S. J.: Non-isothermal crystallization and melting of ethylene-vinylacetate copolymers with different vinyl acetate contents. Express Polymer Letters, **2**, 623–629 (2008).
DOI: 10.3144/expresspolymlett.2008.75

[14] Goodarzi V., Jafari S-H., Khonakdar H. A., Monemian S. A., Hässler R., Jehnichen D.: Nonisothermal crystallization kinetics and determination of surface-folding free energy of PP/EVA/OMMT nanocomposites. Journal of Polymer Science Part B: Polymer Physics, **47**, 674–684 (2009).
DOI: 10.1002/polb.21672

[15] Li S-N., Li Z-M., Yang M-B., Hu Z-Q., Xu X-B., Huang R.: Carbon nanotubes induced nonisothermal crystallization of ethylene-vinyl acetate copolymer. Materials Letters, **58**, 3967–3970 (2004).
DOI: 10.1016/j.matlet.2004.09.005

[16] Khanna Y. P.: A barometer of crystallization rates of polymeric materials. Polymer Engineering and Science, **30**, 1615–1619 (1990).
DOI: 10.1002/pen.760302410

[17] Ying J-R., Liu S-P., Guo F., Zhou X-P., Xie X-L.: Non-isothermal crystallization and crystalline structure of PP/POE blends. Journal of Thermal Analysis and Calorimetry, **91**, 723–731 (2008).
DOI: 10.1007/s10973-007-8586-6

[18] Li C. X., Kong Q. S., Zhao J., Zhao D. L., Fan Q. R., Xia Y. Z.: Crystallization of partially miscible linear low-density polyethylene / poly(ethylene-co-vinylacetate) blends. Materials Letters, **58**, 3613–3617 (2004).
DOI: 10.1016/j.matlet.2004.06.057

[19] Hussein I. A.: Nonisothermal crystallization kinetics of linear metallocene polyethylenes. Journal of Applied Polymer Science, **107**, 2802–2809 (2008).
DOI: 10.1002/app.27392

[20] Avrami M.: Kinetics of phase change I: General theory. Journal of Chemical Physics, **7**, 1103–1112 (1939).
DOI: 10.1063/1.1750380

[21] Avrami M.: Kinetics of phase change II: Transformation-time relations for random distribution of nucle. Journal of Chemical Physics, **8**, 212–224 (1940).
DOI: 10.1063/1.1750631

[22] Avrami M.: Granulation, phase change and microstructure kinetics of phase change. III. Journal of Chemical Physics, **9**, 177–184 (1941).
DOI: 10.1063/1.1750872

[23] Cebe P., Hong S. D.: Crystallization behavior of poly (ether-ether-ketone). Polymer, **27**, 1183–1192 (1986).
DOI: 10.1016/0032-3861(86)90006-6

[24] Run M., Gao J., Li Z.: Nonisothermal crystallization and melting behavior of mPE/LLDPE/LDPE ternary blends. Thermochimica Acta, **429**, 171–178 (2005).
DOI: 10.1016/j.tca.2005.03.007

[25] Paul D. R., Newman S.: Polymer blends. Wiley, New York (1978).

[26] Di Lorenzo M. L., Silvestre C.: Non-isothermal crystallization of polymers. Progress in Polymer Science, **24**, 917–950 (1999).
DOI: 10.1016/S0079-6700(99)00019-2

[27] Christian J. W.: The theory of transformation in metals and alloys. Pergamon Press, Oxford (1975).

[28] Liu T., Mo Z., Wang S.: Nonisothermal melt and cold crystallization kinetics of poly(aryl ether ether ketone ketone). Polymer Engineering and Science, **37**, 568–571 (1997).
DOI: 10.1002/pen.11700

[29] Liu M., Zhao Q., Wang Y., Zhang C., Mo Z., Cao S.: Melting behaviors, isothermal and non-isothermal crystallization kinetics of nylon 1212. Polymer, **44**, 2537–2545 (2003).
DOI: 10.1016/s0032-3861(03)00101-0

[30] Song J. B., Chen Q. Y., Ren M. Q., Sun X. H., Zhang H. L., Zhang H. F., Mo Z.: Effect of partial melting on the crystallization kinetics of nylon-1212. Journal of Polymer Science Part B: Polymer Physics, **43**, 3222–3230 (2005).
DOI: 10.1002/polb.20525

[31] Tao Y., Pan Y., Zhang Z., Mai K.: Non-isothermal crystallization, melting behavior and polymorphism of polypropylene in [beta]-nucleated polypropylene/recycled poly(ethylene terephthalate) blends. European Polymer Journal, **44**, 1165–1174 (2008).
DOI: 10.1016/j.eurpolymj.2008.01.023

[32] Huang J-W., Wen Y-L., Kang C-C., Tseng W-J., Yeh M-Y.: Nonisothermal crystallization of high density polyethylene and nanoscale calcium carbonate composites. Polymer Engineering and Science, **48**, 1268–1278 (2008).
DOI: 10.1002/pen.21087

[33] Jin J., Chen S., Zhang J.: Investigation of UV aging influences on the crystallization of ethylene-vinyl acetate copolymer via successive self-nucleation and annealing treatment. Journal of Polymer Research, in press (2009).
DOI: 10.1007/s10965-009-9374-8

[34] Kissinger H. E. Variation of peak temperature with heating rate in differential thermal analysis. Journal of Research of the National Bureau of Standard, **57**, 217–221 (1956).

[35] Liu T-Y., Lin W-C., Yang M-C., Chen S-Y.. Miscibility, thermal characterization and crystallization of poly(l-lactide) and poly(tetramethylene adipate-co-terephthalate) blend membranes. Polymer, **46**, 12586–12594 (2005).
DOI: 10.1016/j.polymer.2005.10.100

eXPRESS Polymer Letters Vol.4, No.3 (2010) 153–160
Available online at www.expresspolymlett.com
DOI: 10.3144/expresspolymlett.2010.20

Influence of processing on the ethylene-vinyl alcohol (EVOH) properties: Application of the successive self-nucleation and annealing (SSA) technique

E. Franco-Urquiza[*]*, O. O. Santana, J. Gámez-Pérez, A. B. Martínez, M. Ll. Maspoch*

Centre Català del Plàstic, Universitat Politècnica de Catalunya (UPC), Colom 114, 08222 Terrassa, Spain

Received 8 October 2009; accepted in revised form 22 December 2009

Abstract. Films of EVOH copolymers, processed three times by twin-screw extrusion were prepared using a cast-film line. The variation on the melt flow rate (MFR) and rheological behaviour of the films were determined, as well as the thermal properties assessed by differential scanning calorimetry (DSC) and dynamic-mechanical thermal analysis (DMTA). As the results showed that the reprocessing induced an increase in the viscosity and orientation of the films, it was suggested that structural modifications from chain-extension or cross-linking reactions promoted by hydroxyl and residual acetoxyl groups, could be occurring. The successive self-nucleation and annealing (SSA) technique was applied, evidencing the structural modifications on the EVOH copolymer.

Keywords: *processing technologies, EVOH, SSA, processing-structure relationship*

1. Introduction

Ethylene-vinyl alcohol (EVOH) copolymers are semicrystalline materials regardless of vinyl alcohol (VOH) content. They are prepared commercially by transesterification (saponification) of Ethylene-vinyl acetate copolymers (EVA). They could be considered, then, as complex copolymers of ethylene, vinyl alcohol and some vinyl acetate units, if the saponification process is not 100% complete [1–3]. In addition, owing to the free-radical nature of the EVA copolymerization, the resulting EVOH copolymers posses a certain degree of short chain branching, which, according to Vanderhart *et al*. [4] are rejected from the crystalline region.

EVOH copolymers are widely employed in food packaging, biomedical and pharmaceutical industries because of their excellent barrier properties to gases, hydrocarbons and organic solvents [3, 5]. Such properties are caused by strong hydrogen bond interactions, both inter and intra-molecular, which reduce the free volume of the polymer chains [6]. However, the barrier properties, stiffness or tensile strength, drop dramatically in high relative humidity conditions. EVOH copolymers are highly hygroscopic, as a consequence of the hydrophilic OH side groups and their interaction with the absorbed water molecules weakens the inter- and intra-molecular hydrogen bonds, increasing the free volume of the chains [7, 8]. To avoid that loss of the barrier capacity, some authors have proposed the addition of organo-modified clays into the EVOH matrix via melt-blending method, using internal mixers and twin-screw extrusion [9, 10].

Some authors [11–13] suggested a melt-blending process for preparation of thermoplastic/organo-modified clays that could be easily scaled to industrial level. Such process implies three steps of twin-screw extrusion: (a) preparation of a master-batch with high clay content (~10 wt%), (b) master-

[*]Corresponding author, e-mail: edgar.adrian.franco@upc.edu

batch homogenization and (c) final dilution to the required clay contents.

The global aim of this work is to analyze the possible structural and properties modifications of EVOH occurred during a 3-step twin-screw extrusion process during its melt-blending with organo-modified clay. In this paper it will be discussed and analysed by the use of the thermal fractionation technique known as *successive self-nucleation and annealing* (SSA) and relate those results with structural changes suggested by other techniques (plate-plate rheometer, dynamo mechanical thermal analysis and differential scanning calorimetry).

The SSA fractionation technique, proposed by Müller *et al*. 14], is based on the existence of defects in the main polymer chain, which limits the segment length able to crystallize, contributing to the generation of a crystalline distribution with different lamellar thicknesses during crystallization. The method involves applying a thermal treatment that includes intercalated isothermal steps, which promote the nucleation and annealing of crystals. A final standard heating scan reveals the succession of endothermic signals corresponding to the melting of each crystalline entity [15].

Müller *et al*. [14] analyzed the branching distribution from linear low-density polyethylene (LLDPE), pointing out that the melting enthalpy of each signal can be considered proportional to the normalized weight fraction of molecular populations with a certain branching content. The SSA technique has also been successfully applied in the characterization of several polymer systems [16], as for example on functionalized polyethylenes [17].

2. Experimental

2.1. Materials

EVOH copolymer (Soarnol® DC3203F) containing 32 mol% ethylene (E32) was kindly supplied by Nippon Gohsei (Osaka, Japan). The melting point (T_m) and glass transition (T_g) temperatures are 183 and 69°C respectively.

2.2. Melt processing and films preparation

Films of 300 μm thickness were obtained using a cast film line, consisting of a single-screw extruder (L/D = 25; D = 20 mm) Collin Teach Line 20T-E (Ebersberg, Germany), a multi-manifold die and chill-rolls calender Teach Line CR 72T (Ebersberg, Germany). The profile temperatures used were those suggested by the E32 producer, 160°C in feed section to 220°C at the extrusion die and the chill-rolls were set at 50°C with 7 bar of pressure.

In order to simulate the production of EVOH/clay nanocomposites, E32 was processed several times (1, 2 or 3) in a twin-screw extruder (L/D = 36; D = 25 mm) Collin ZK-35 (Ebersberg, Germany) before the film production. In every reprocessing step, the twin-screw rotation speed was set at 80 rpm and the processing temperatures were comprised between 160°C in the feed section and 220°C at the extrusion die. According to the processing history, the films were named as follows: E32-0X for the film non-processed by twin-screw extruder and E32-1X, 2X or 3X for the films processed in twin-screw extruder 1, 2 or 3 times, respectively.

It is important to mention that E32 was dried (in pellet form) at 110°C during 10 h in an air oven J. P. Selecta (Barcelona, Spain) before each twin-screw extrusion and cast film processes, since the presence of coordinated water, along with shear stress and temperature processing, may lead to significant modifications in the chemical structure of EVOH.

2.3. Characterization techniques

Melt flow rate was determined using a melt flow tester CEAST 6841 (Pianezza, Italy) at 210°C and a load of 2.16 kg, according to the ISO 1133 standard.

Rheological tests were performed in a dynamic rheometer AR-G2 from TA Instrument (New Castle, USA) with 25 mm diameter parallel plates and a gap of 300 μm approximately. The tests were run at a frequency rate from 0.1 to 100 Hz, 220°C and 2% strain amplitude to ensure that measurements were taken within the linear viscoelastic range. All experiments were conducted under nitrogen gas blanket in order to prevent thermo-oxidative degradation during the test. The apparent shear viscosity (η_{app}) *vs*. shear rate ($\dot{\gamma}$) curves were generated using the Cox-Merz rule and the data were adjusted using the Cross model.

Dynamic mechanical thermal analysis (DMTA) measurements in tensile mode were performed using a DMTA Q800 from TA Instruments (New

Castle, USA). The tests were run in a temperature range from 25 to 160°C under linear viscoelastic conditions applying a static stress of 1 MPa with a frequency of 1 Hz and a constant heating rate of 2°C/min. In order to prevent sample buckling during heating, the 'force track' option was activated and set at 120% with an initial pre-load of 0.5 N. All rectangular samples (15×5×0.3 mm) were taken from central part of the films in the melt flow direction.

Differential scanning calorimetry (DSC) measurements were carried out using a Perkin-Elmer Pyris 1 calorimeter (Massachusetts, USA) with a cooling system Intracooler IIP. The calorimeter was previously calibrated with standard samples of Indium and Lead. The samples were taken form the central zone of the films with exactly 10 mg in weight and the scans were run under nitrogen atmosphere using aluminium pans.

Two different thermal experiments were performed: the first one consisted in a *standard evaluation*, with a first heating scan (from 30 to 230°C with an isothermal step of 3 min), cooling scan (including an isothermal step) and subsequent second heating scan. All runs were conducted at a heating/cooling rate of 10°C/min. The second approach consisted in applying the *successive self-nucleation and annealing* (SSA) method, according to the thermal program sketched in Figure 1. After erasing the thermal history and setting a common controlled cooling at 10°C/min (ramp A, in Figure 1), five cycles of heating-cooling scans with isothermal steps of 5 min were run, decreasing the isothermal temperature (T_{s1}) in each cycle. Finally, a heating scan (ramp B in Figure 1) was performed in order to reveal the melting behaviour of the treated samples.

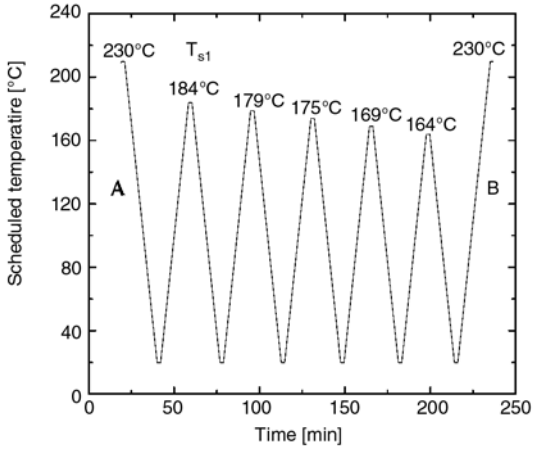

Figure 1. Schematic representation of successive self-nucleation and annealing (SSA) thermal treatment

The initial isothermal temperature T_{s1} = 184°C, selected as the optimum self-nucleation temperature (Figure 1), was determined by self-nucleation tests performed according to the methodology suggested by Fillon *et al*. [18]. This temperature caused the maximum shift on the peak crystallization temperature (T_c) without annealing. The subsequent temperatures (179 to 164°C) were selected at intervals of 5°C lower than the previous T_s (Figure 1), following the program suggested for polyethylene based systems [14].

The melting (T_m) and crystallization (T_c) temperatures, as well as enthalpies related to the corresponding signals, were obtained according to standards procedures. In order to estimate the crystallinity degree (X_c), the enthalpy of a 100% pure crystalline poly-vinyl alcohol (157.8 J/g) has been taken [8]. According to Cerrada *et al*. [8], EVOH copolymers show a polymorphic behaviour depending on composition and thermal treatment. Nevertheless, with relative high vinyl alcohol content, the EVOH copolymers crystallize into a monoclinic lattice, similar to that of poly-vinyl alcohol, regardless of the ethylene sequences, which are located as punctual defects into the main crystalline lattice.

3. Results and discussion

3.1. Melt flow rate and rheological measurements

The variations on the melt flow rate (MFR) with respect to the number of twin-screw extrusion steps is shown in Figure 2a. It can be observed that the MFR decreases up to 26% from the E32-0X as the number of extrusion steps increases. Such a fall in MFR values lead to perform a detailed study of the rheological behaviour with a plate-plate rheometer. The curves of apparent shear viscosity (η_{app}) versus shear rate ($\dot{\gamma}$) obtained after applying the Cox-Merz rule, are plotted in Figure 2b.

From the rheological measurements, it can be noticed an increase of the zero shear viscosity (η_0) as well as a decrease on $\dot{\gamma}$ at the beginning of the pseudoplastic behaviour. This implied an increase on the characteristic time (k), as reported in Table 1, where the main rheological parameters for all materials are summarized.

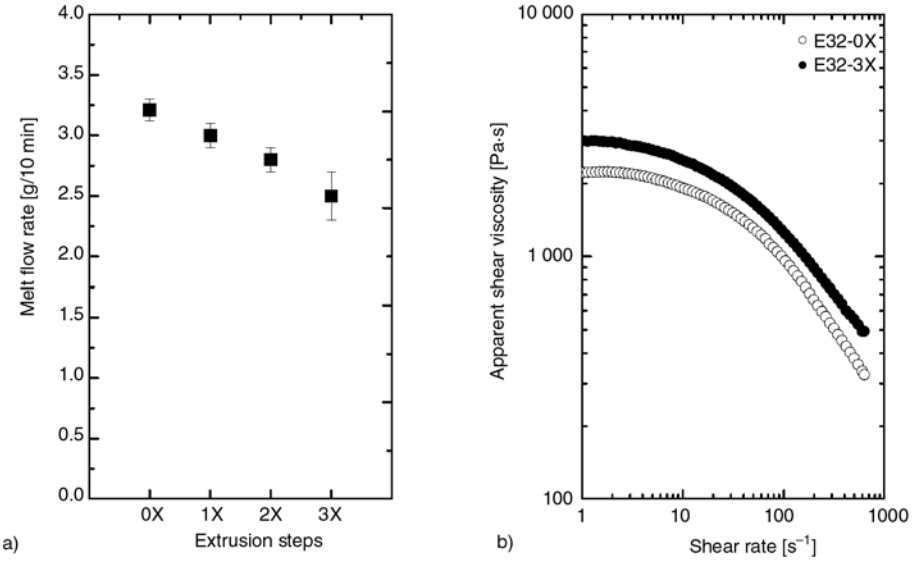

Figure 2. a) Melt flow rate variation for each extrusion step and b) apparent shear viscosity related to shear rate

Table 1. Rheological parameters based on the Cross equation

	η_0 [Pa·s]	k [s]	m
E32-0X	2321	0.016	0.86
E32-3X	3163	0.019	0.78

The results above mentioned indicate that some changes in the chain structure, induced during the processing of EVOH, altered the rheological behaviour, increasing the overall viscosity of the melt under similar temperature and shear conditions. Such behaviour supports the idea of an increase in molecular weight (M_w) altogether with a slight increase on molecular weight distribution. Artzi *et al*. [19] working with EVOH/nanocomposites pointed out that when EVOH is processed at high temperatures, two competitive mechanisms may take place, namely thermal degradation (with chain scission) and grafting and oxidative cross-linking reactions. Similar results have been reported by Lagaron *et al*. [20] under thermo-oxidative conditions (about 2 h at 215°C) without shearing.

Considering that some traces of acetoxyl groups from incomplete saponification of EVA precursor could be present, some intermolecular transesterification reactions between the ester and hydroxyl groups could be taking place, resulting in some cross-linking and/or chain extension reactions. In addition, Rodríguez-Vázquez *et al*. [21] suggested some combination and addition of macro-radicals to chain-linked double bonds studying degradation and stabilization of EVA, which could also be present in EVOH.

The increase on shear viscosity in the Newtonian plateau implies an increase in the elongational viscosity (following the Troutonian relation), which would promote an increase on the orientation degree during calendering [22]. Consequently, it can be expected to find out other changes in the film properties like in the mechanical behaviour [12].

3.2. Dynamic mechanical thermal analysis

The DMTA analysis performed in tensile mode revealed the differences in the mechanical behaviour of the films after reprocessing. This is shown in Figure 3, where the storage modulus and loss tangent (tanδ) of E32-0X and E32-3X are presented.

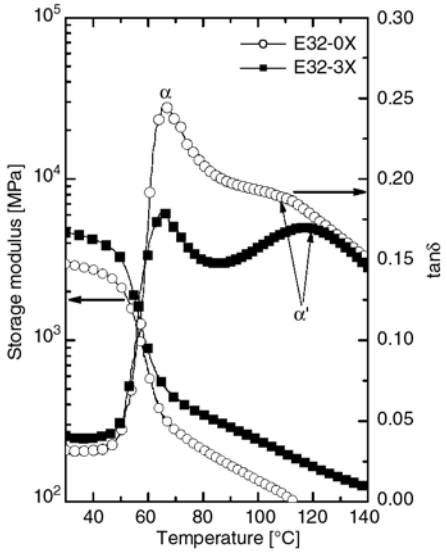

Figure 3. Temperature dependence of the storage modulus and loss tangent of EVOH

It can be observed that the storage modulus increased after the three twin-screw extruder steps in the whole range of temperatures evaluated. On the other hand, it is also noticeable that tanδ shows two maxima, indicating different structural relaxations. The main one, labelled as α in Figure 3 is indicative of glass transition temperature and remains unchanged at approximately 63°C. The lower intensity of this signal in the E32-3X film is consequence of a decrease on the viscous component (loss modulus) along with the mentioned raise in storage modulus.

The second relaxation phenomenon, named as α′ is displayed at about 110–120°C. It is quite noticeable the increase in the definition and shift to higher temperatures for E32-3X. According to Cerrada *et al*. [23], α′ is strongly related to the molecular orientation, corresponding to motions within the crystalline phase, caused either by the relaxation of hydrogen bonds or the movements close to the crystal lamellae surface. In this case, such orientation could have been induced during the cast film processing.

Since cast-film processing conditions were exactly the same in all cases, the fact that the film E32-3X shows higher orientation can be explained on basis of the increase of viscosity produced by the twin-screw extruder reprocessing. Such orientation, along with the hypothetical increase on M_w and/or cross-linking, would be the cause for the higher values on storage modulus upon reprocessing on twin-screw extruder.

3.3. Differential scanning calorimetry

In Figure 4 are shown the DSC melting endotherms corresponding to the first and the second heating scans for all films. The thermal parameters obtained are summarized in Table 2.

In the first heating scan (Figure 4a) it can be observed that the endothermic signal becomes more intense and slightly narrower as the number of twin-screw extrusion steps increases, indicating that the most homogeneous crystal distribution is found in the E32-3X film. Concerning to the second heating scan, the intensity of the DSC melting endotherms does not evidence significant variations as the number of twin-screw extrusion steps increase, as seen in Figure 4b. Therefore, it can be deduced that the first heating scan, which is affected by the thermo-mechanical history of the films, is strongly influenced by the induced morphology of the films during the cast-film process (crystallization in oriented melt). This is also evidenced on the X_c values (shown in Table 2) during the first melting, which are larger than those obtained from the DSC curves recorded during second heating run.

Table 2. Melting temperatures and crystallization degree of EVOH copolymers films

	First heating		Second heating	
	T_m [°C]	X_c [%]	T_m [°C]	X_c [%]
E32-0X	182.1	67	183.3	47
E32-1X	181.1	61	182.1	48
E32-2X	180.7	61	182.2	46
E32-3X	178.4	57	181.4	40

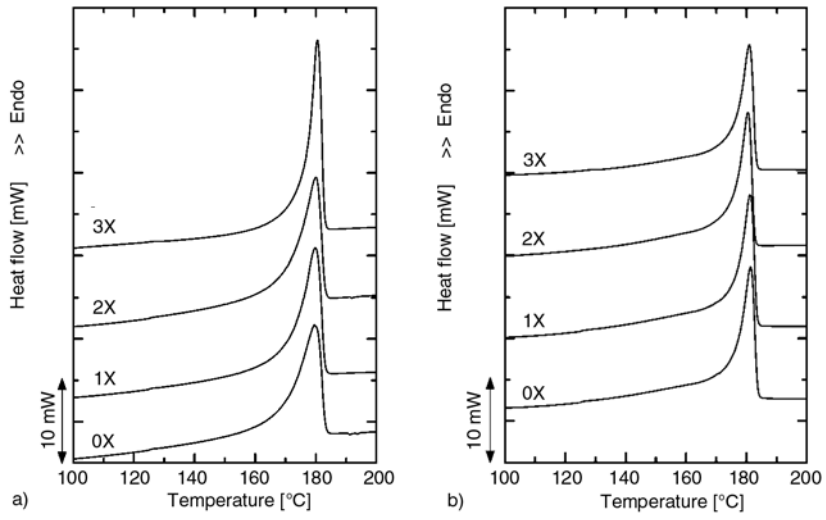

Figure 4. DSC heating scan: a) first heating and b) second heating after controlled cooling

Table 2 summarizes the assessed thermal parameters in the first and second heating scans. It can be noticed that during the first heating scan, the crystal melting temperature of the reprocessed films, especially in the case of E32-3X, are slightly lower than those shown by the E32-0X film. On the other hand, during the second scan, the melting temperature (T_m) of EVOH seems not to be affected by the twin-screw reprocessing. This data would be in agreement with the processing induced orientation of the E32-3X films, previously stated.

Concerning the variations in the crystallinity percentage, a decreasing trend with the number of reprocessing steps can be observed in Table 2. Such trend would imply that under the dynamic cooling conditions applied, the crystallization ability of the reprocessed materials is hindered. Again, these results point to some structural modification, like some cross-linking, that could be taking place and affecting the crystallization process.

3.4. Successive self-nucleation and annealing (SSA)

Figure 5 shows the final heating scans after applying the SSA thermal treatment (i.e., the final heating run in the experimental part, ramp B in Figure 1). It can be appreciated a great segregation with outstanding resolution of the melting signals, similar to those obtained for LDPE and LLDPE systems. This segregation should be expected if the existence of short chain branching is considered. According to Vanderhart *et al*. [4] in their work about molecular partitioning on EVOH monitored by solid-state ^{13}C, while OH group behaves like an interstitial defects, short chain branches of one, two and four carbons, as well as acetate branches are strongly rejected form the crystalline region of these copolymers, just like in LDPE [16].

The SSA treatment produced five fractions in every sample. Only those four T_s temperatures capable of producing self-nucleation and annealing are considered for the analysis, since they are directly responsible for the annealed crystals that subsequently melt during final heating scan. Figure 6 shows the melting temperature of each fraction *vs.* T_s. It can be seen that, as expected, these melting temperatures only depend on the T_s temperature. This indicates that the fractionation procedure is effective in separating chains of a particular short chain branching content.

The DSC curves of Figure 5 can be integrated and partial areas corresponding to each peak. They can be considered to be proportional to a normalised weight fraction of crystalline population with same lamellar thickness. The histogram associated to the enthalpy fractions is shown in Figure 7. It is possible to observe a great depletion of the most linear fraction when EVOH copolymer is processed by twin-screw extruder. This reduction contrasts to the behaviour displayed by less linear one, with T_s temperatures of 179, 174 and 169°C, which tend to increase at the expense of the highest one (T_s = 184°C). Similar behaviour has been observed by Marquez *et al*. [17] on LLDPE grafted with diethyl maleate (DEM), where the most linear sequences showed the higher susceptibility to the DEM attack.

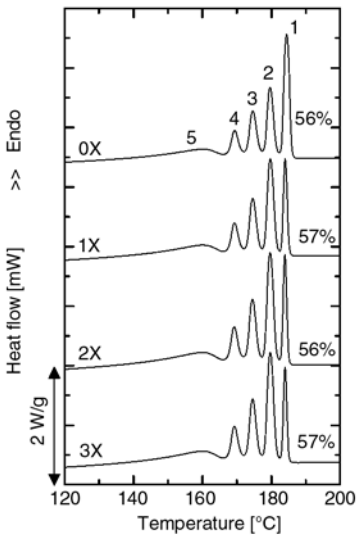

Figure 5. DSC heating scans after SSA fractionation

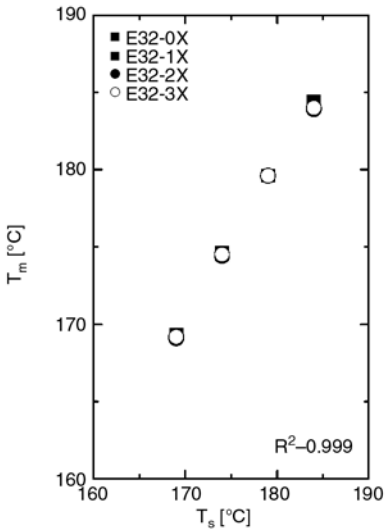

Figure 6. Linear relationship between the melting peak and T_s temperatures

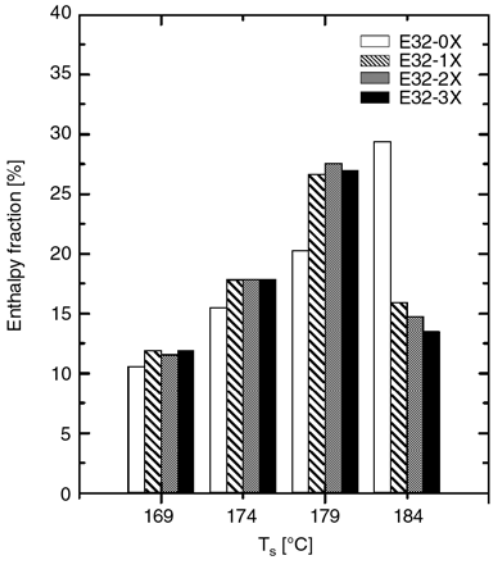

Figure 7. Histogram corresponding to the enthalpy fraction contribution

In our case, the above mentioned depletion could be a consequence of the reactions occurred during the twin-screw extrusion, as discussed previously; pointing out that the strongest variation seems to occur after the first twin-screw extrusion process.

It is interesting to note that the crystallinity degree generated after the SSA treatment in all sample remains constant (≈56%) (as reported in Figure 5), what seems to indicate that the chemical modifications affect to the crystallization characteristics under dynamic conditions (kinetic aspects). But if the experimental conditions favour an annealing or the thermal rates are slow, the material has basically the same crystallization ability.

4. Conclusions

The melt-blending process of EVOH copolymers induces some structural modifications, which promoted a high molecular orientation of the films during the cast-film process.

MFR and rheological measurements displayed an increase on molecular weight of EVOH as a consequence of chain-extension reactions promoted by the reactivity of residual hydroxyl and acetoxyl groups. According to the DMTA results, the reactions should improve the mechanical behaviour, as appreciated by high storage modulus obtained.

The thermal fractionated EVOH films clearly showed a great segregation of several series of melting signals, proving that the SSA technique is a complementary useful tool for the structural characterization. The modifications induced during the processing of EVOH promoted the redistribution of the crystalline populations, where the less linear fractions were favoured by the most linear one.

Acknowledgements

The authors want to thank to the Ministerio de Educación y Ciencia for the financing of the MAT 2003-08480-C03-02 project. E. Franco-Urquiza thanks to the National Council of Science and Technology (CONACyT) of México, for the support of a doctoral research grant.

References

[1] Noro K.: Hydrolisis of polyvinyl acetate to polyvinyl alcohol. in 'Polyvinyl alcohol: Properties and applications' (ed.: Finch C. A.) John Wiley, London, Vol 1, 91–120 (1973).

[2] Pérez E., Lujan M., de Salazar J. M.: Preparation and properties of terpolymers of ethylene, vinyl acetate and vinyl alcohol. Macromolecular Chemistry and Physics, **201**, 1323–1328 (2000).
DOI: 10.1002/1521-3935(20000801)201:12<1323::AID-MACP1323>3.0.CO;2-7

[3] Ramakrishnan S.: Well-defined ethylene vinyl alcohol copolymers via hydroboration- control of composition and distribution of the hydroxyl-groups on the polymer backbone. Macromolecules, **24**, 3753–3759 (1991).
DOI: 10.1021/ma00013a003

[4] Vanderhart D. L., Simmons S., Gilman J. W.: Solid-state C-13 nuclear-magnetic-resonance spectroscopy of ethylene-vinyl alcohol copolymers – Morphological partitioning of hydroxyls. Polymer, **36**, 4223–4232 (1995).
DOI: 10.1016/0032-3861(95)92217-3

[5] Lasagabaster A., Abad M. J., Barral L., Ares A.: FTIR study on the nature of water sorbed in polypropylene (PP)/ethylene alcohol vinyl (EVOH) films. European Polymer Journal, **42**, 3121–3132 (2006).
DOI: 10.1016/j.eurpolymj.2006.03.029

[6] Aucejo S., Marco C., Gavara R.: Water effect on the morphology of EVOH copolymers. Journal of Applied Polymer Science, **74**, 1201–1206 (1999).
DOI: 10.1002/(SICI)1097-4628(19991031)74:5<1201::AID-APP17>3.0.CO;2-8

[7] Alvarez V. A., Ruseckaite V. A., Vázquez A.: Kinetic analysis of thermal degradation in poly(ethylene-vinyl alcohol) copolymers. Journal of Applied Polymer Science, **90**, 3157–3163 (2003).
DOI: 10.1002/app.13071

[8] Cerrada M. L., Pérez E., Pereña J. M., Benavente R.: Wide-angle X-ray diffraction study of the phase behavior of vinyl alcohol and ethylene copolymers. Macromolecules, **31**, 2559–2564 (1998).
DOI: 10.1021/ma9705127

[9] Artzi N., Narkis M., Siegmann A.: EVOH/clay nanocomposites produced by dynamic melt mixing. Polymer Engineering and Science, **44**, 1019–1026 (2004).
DOI: 10.1002/pen.20095

[10] Artzi N., Khatua B. B., Tchoudakov R., Narkis M., Berner A., Siegmann A., Lagaron J. M.: Physical and chemical interactions in melt mixed Nylon-6/EVOH blends. Journal of Macromolecular Science Part B: Physics, **43**, 605–624 (2005).
DOI: 10.1081/MB-120030009

[11] Chow W. S., Khim L. Y., Kang A. T.: Flexural properties of polystyrene/organo-montmorillonite masterbatch composites. Journal of Reinforced Plastics and Composites, **27**, 255–261 (2008).
DOI: 10.1177/0731684407083001

[12] Franco-Urquiza E., Gamez-Perez J., Sánchez-Soto M., Santana O. O., Maspoch M. L.: The effect of organo-modifier on structure and properties of poly(ethylene-vynil alcohol)/organo-modified montmorillonite composites. Polymer International, in press (2010).
DOI: 10.1002/pi.2788

[13] Maspoch M. L., Franco-Urquiza E., Gamez-Perez J., Santana O. O., Sanchez-Soto M.: Fracture behaviour of poly[ethylene-(vinyl alcohol)]/organo-clay composites. Polymer International, **58**, 648–655 (2009).
DOI: 10.1002/pi.2574

[14] Müller A., Hernández Z., Arnal M., Sánchez J.: Successive self-nucleation/annealing (SSA): A novel technique to study molecular segregation during crystallization. Polymer Bulletin **39**, 465–472 (1997).
DOI: 10.1007/s002890050174

[15] Arnal M., Balsamo V., Ronca G., Sánchez A., Müller A., Cañizales E., de Navarro C.: Applications of successive self-nucleation and annealing (SSA) to polymer characterization. Journal of Thermal Analysis and Calorimetry, **59**, 451–470 (2000).
DOI: 10.1023/A:1010137408023

[16] Müller A. J., Arnal M. L.: Thermal fractionation of polymers. Progress in Polymer Science **30**, 559–603 (2005).
DOI: 10.1016/j.progpolymsci.2005.03.001

[17] Marquez L., Rivero I., Müller A.: Application of the SSA calorimetric technique to characterize LLDPE grafted with diethyl maleate. Macromolecular Chemistry and Physics, **200**, 330–337 (1999).
DOI: 10.1002/(SICI)1521-3935(19990201)200:2<330::AID-MACP330>3.0.CO;2-Y

[18] Fillon B., Wittmann J. C., Lotz B., Thierry A.: Self-nucleation and recrystallization of isotactic polypropylene (alpha phase) investigated by differential scanning calorimetry. Journal of Polymer Science Part B: Polymer Physics, **31**, 1383–1393 (1993).
DOI: 10.1002/polb.1993.090311013

[19] Artzi N., Tzur A., Narkis M., Siegmann A.: The effect of extrusion processing conditions on EVOH/clay nanocomposites at low organo-clay contents. Polymer Composites, **26**, 343–351 (2005).
DOI: 10.1002/pc.20096

[20] Lagaron J. M., Giménez E., Saura J. J.: Degradation of high barrier ethylene-vinyl alcohol copolymer under mild thermal-oxidative conditions studied by thermal analysis and infrared spectroscopy. Polymer International, **50**, 635–642 (2001).
DOI: 10.1002/pi.674

[21] Rodriguez-Vazquez M., Liauw C. M., Allen N. S., Edge M., Fontan E.: Degradation and stabilisation of poly(ethylene-*stat*-vinyl acetate): 1-spectroscopic and rheological examination of thermal and thermo-oxidative degradation mechanisms. Polymer Degradation and Stability, **91**, 154–164 (2006).
DOI: 10.1016/j.polymdegradstab.2005.04.034

[22] Wissbrun K., Dealy J. M.: Melt rheology and its role in plastics processing: Theory and applications. Kluwer Academics, Dordrecht (1990).

[23] Cerrada M. L., Benavente R., Pérez E., Pereña J. M.: The effect of tensile drawing on the structure and relaxation processes in vinyl alcohol-ethylene copolymers. Polymer, **42**, 3127–3138 (2001).
DOI: 10.1016/S0032-3861(00)00698-4

eXPRESS Polymer Letters Vol.4, No.3 (2010) 161–170
Available online at www.expresspolymlett.com
DOI: 10.3144/expresspolymlett.2010.21

Functionalization of LDPE and mLLDPE via grafting *trans*-ethylene-1,2-dicarboxylic acid by reactive extrusion

Yu. M. Krivoguz[1], *A. M. Guliyev*[2], *S. S. Pesetskii*[1*]

[1]Department of Technology of Polymeric Composite Materials and Particles V.A. Belyi Metal-Polymer Research Institute of National Academy of Sciences of Belarus, 32a Kirov Street, 246050 Gomel, Republic of Belarus
[2]Institute of Polymer Materials National Academy of Sciences of Azerbaijan, 124 S.Vurgun Street, Az 5004 Sumgait, Azerbaijan Republic

Received 16 October 2009; accepted in revised form 22 December 2009

Abstract. An investigation was made of grafting *trans*-ethylene-1,2-dicarboxylic acid (TEDA) onto metallocene-linear low-density polyethylene (mLLDPE) and low-density polyethylene (LDPE) in the course of reactive extrusion. The initiator was 1,3-bis-(tert-butyl-peroxyisopropyl)benzene. The graft efficiency of TEDA has been shown to increase with increasing initiator concentration, irrespective of polyethylene type. The graft values for LDPE were higher than for mLLDPE over the initiator concentration range (0.05 to 0.4 wt%). The rheological properties of mLLDPE were found to undergo more tangible changes during functionalization than those of LDPE. These changes were caused by side reactions, mainly macromolecular crosslinking. It has been established that some carboxyl groups get transformed to anhydride groups in the grafted product. The concentration of end double bonds reduces, but intramolecular unsaturation in both polyethylenes increases. Data are presented on thermal and stress-strain (mechanical) properties of virgin and functionalized polymers, as well as rheological and viscoelastic properties of their melts.

Keywords: *material testing, low-density polyethylene, linear low-density polyethylene, funtionalization, trans-ethylene-1,2-dicarboxylic acid*

1. Introduction

Functionalization of polymers and copolymers of olefins via grafting polar monomers (or oligomers) onto macromolecules in melt by reactive extrusion has been studied for several decades. However, the importance of fundamental and applied investigations into this problem still holds and even is becoming more pressing. This is explained, on the one hand, by lack of a quantitative theory required to calculate the course of both main reactions and side processes in reacting systems. On the other hand, technological equipment, particularly extrusion compounding reactors, has been updated continually, which should be taken into consideration in choosing optimal technological parameters for functionalization. Besides, the necessity of solving applied problems requires that basic research be done into functionalization of various olefin copolymers [1–7], polyethylene (PE) and polypropylene (PP) blends [8, 9] as well as blends of polyolefins (PO) with copolymers of ethylene and higher olefins [10, 11], copolymers of ethylene and vinyl acetate [12], linear polyethylene [13] and others.

It should be noted that most studies of fundamental nature have been concerned with functionalization of PE and PP of conventional grades. Results of those studies have been reported in reviews and books [14–19]. It has been learned that saturated PO functionalization by grafting polar monomers

*Corresponding author, e-mail: otdel5mpri@tut.by

onto their macromolecules in melt and grafted product output depends on the nature of reactants (polymer, initiator of radical reactions, monomer to be grafted), composition of the reacting system and on a set of technological factors of which melt temperature, reaction period, degree of shear effect upon the melt are most important [16, 19, 20]. It is believed that at monomer grafting onto saturated PO, the free radicals, formed as a result of initiator decomposition, break away mobile hydrogen from macromolecules, while macroradicals formed interact with monomers making them grafted [18, 21]. There has been found a difference in the mechanisms and kinetics of side reactions during PE and PP functionalization: PE macromolecules undergo crosslinking for the most part, while PP macromolecules suffer degradation owing to β-decomposition of macroradicals which are formed at interaction with the initiator.

A number of basic laws explain the mechanism and kinetics of monomer grafting, but there are unsolved problems preventing the understanding of macromolecular transformations in greater detail. Particularly, it isn't clear what is the role of unsaturated (double) bonds – contained in PO macromolecular structure – in the reactions of functionalization? What is the character of double bond transformations, and how the total saturation level varies in the course of functionalization? What is the specific influence of molecular structure (degree of macromolecular branching, type of unsaturation, etc.) upon grafted product ratio and transformation of different double bonds during free-radical reactions taking place at monomer grafting?

Clarification of some aspects of these problems is dealt with in this work; its main task is to analyze the specificity of grafting a carboxyl-containing monomer onto different modifications of low density polyethylene, and to determine values of important properties of the prepared materials.

2. Experimental

2.1. Materials

The objects for analysis were low-density polyethylene (LDPE) (supplied by 'Polimir' Co., Republic of Belarus; Grade 15803-020; melting temperature T_m = 113°C; crystallization temperature T_{cr} = 89.5°C as determined by the differential scanning calorimetry (DSC) technique at a heating rate of 16°C/min) and metallocene linear low-density polyethylene (mLLDPE) (supplied by DOW Co., USA; Grade Elite 5400S; T_m = 125.8°C; T_{cr} = 103.7°C). The monomer to be grafted was *trans*-ethylene-1,2-dicarboxylic acid (TEDA) (the IUPAC name is fumaric acid, quality 'Pure', supplied by Komtex Co., Russia); 1,3-bis-(tert-bulyl peroxy-isopropyl)benzene (Grade Perk-14, supplied by Azko Nobel, Netherlands; ($\tau_{0,5}$ = 0.31 min at 200°C, the reactive oxygen concentration 9%) was the initiator.

2.2. Preparation of functionalized PE

The process of functionalization (monomer grafting) was run in the twin-screw extruder TSK 35/40 (Chengdu Pu Rui Polymer Engineering Co., Ltd., China; D = 35 mm; L/D = 40; the number of heating zones was 10); the screws were equipped with special compounding elements (two mixing sections of cam-type and one section of screw-type to ensure melt mixing in the opposite direction to the mainstream flow).

The reaction zone temperature in the extruder was 230°C. The concentration of TEDA grafted onto LDPE and mLLDPE was constant in all of the experiments making 1 wt%; the content of Perk-14 was varied between 0.05 and 0.4 wt%.

2.3. Methods of analysis of the materials

The grafting efficiency (α) and melt flow index (MFI) were the parameters to characterize the course of grafting reaction and side processes, as it had been done elsewhere [20].

Values of α were determined using film samples of thickness 40 μm with absorption IR-spectroscopy technique based on analysis of grafted monomer content in TEDA functionalized polyethylene (PE-g-TEDA) before and after extraction with acetone (Equation (1)):

$$\alpha = \frac{A_\tau}{A_0} \cdot 100 \quad (1)$$

where A_0 and A_τ are, respectively, integral absorption intensities of carbonyl (areas of respective absorption bands) at 1600–1875 cm^{-1} before and after extraction of films in acetone.

IR-spectra were recorded with Fourier Transform Infrared (FTIR) spectroscope Nicolet 5700 (USA).

Table 1. FTIR transmittance peaks for unsaturated bonds

Group	Structure	Wavenumber [cm^{-1}]
Vinylidene	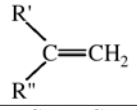	888
Vinyl	RCH=CH$_2$	909; 995
trans-Vinylene	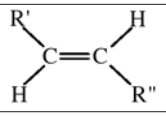	965
cis-Vinylene	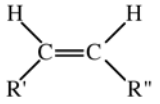	740

The resolution was 4 cm^{-1}; the number of scans was 60.

Unsaturated groups were analyzed using absorption bands at 850–1000 cm^{-1} (Table 1). The analysis was pursued of double bonds belonging to vinyl, vinylidene and *trans*-vinylene groups [22, 23]. It was impossible to define *cis*-vinylene via infrared spectrum because the absorption band at 740 cm^{-1} was overlapped with the intensive band of pendulum oscillations of –CH$_2$– groups at 720 cm^{-1} [22, 23].

The IR-spectra were treated mathematically using computer program OMNIC (Version 7.1) which includes functions to construct base lines and calculate integral intensities of absorption bands. The arithmetic mean values for integral intensities were obtained from analysis of nine samples (relative error of a single measurement did not exceed 1%).

Polymer melt viscosities were estimated by the flow index which was determined at 230°C under 10 kg load using the IIRT-AM device (Ukraine).

Thermal properties of the polymers were judged by the data of DSC. The study was carried out on Perkin Elmer Diamond DSC microcalorimeter (Shelton, USA); the sample weight = 5 mg, heating/cooling rate = 16°C/min. To eliminate effects of thermal pre-history of samples upon structure, measurements were done on samples pre-heated in cells of the calorimeter up to 160°C, thermostated at this temperature for 60 s, then used for analysis.

High elastic properties of melts of initial and functionalized LDPE and mLLDPE were judged by their strength (Equation (2)):

$$\sigma_m = \frac{M}{S_c} \tag{2}$$

where M is the extrudate weight at which it is separated from the capillary; S_c the area of capillary bore; and by swell index of melt jet (Equation (3)):

$$B = \frac{D_e}{D_c} \tag{3}$$

where D_e and D_c are, respectively, diameters of extrudate and capillary. Values of σ_m and B were found following the procedure described elsewhere [8]; the capillary diameter was 1.45 mm; length = 2 mm.

Stress-strain (mechanical) properties of the materials were determined on samples injection moulded at 170°C. Tensile tests were performed on Instron Universal Testing Machine Series 5567 (United Kingdom) according to ISO R527 at a loading (pulling) rate of 50 mm/min.

3. Results and discussion

3.1. Graft efficiency and MFI of materials

It is evident from Figure 1 that, irrespective of PE type, an increase in Perk-14 concentration in a reacting mix causes a rise in α-values. In both polymers, side reactions of macromolecular crosslinking occur simultaneously with grafting, which is understood from lower MFI (higher viscosity) of LDPE and mLLDPE grafted with TEDA (LDPE-g-TEDA and mLLDPE-g-TEDA). It should be mentioned that for mLLDPE, the crosslinking process occurs more actively than in grafting of TEDA onto LDPE. This can probably result from differences in structure of the polymers under investigation.

It is well known, that LDPE macromolecules are characterized by a relatively high degree of branching [23]. Particularly, this polymer contains a great number of short-chain and long-chain side branches randomly distributed along macrochains (the number of –CH$_3$– groups per 1000 carbon atoms = 21.6; ethyl-groups = 14.4) [24]. The mLLDPE produced with addition of metallocene catalysts, has fewer branches consisting of exclusively short-chain ramified structure the branches of which are regularly distributed along the main chain of the polymer [25]. It can be anticipated that with a higher degree of branching the steric factor will stronger influence the course of chemical macromolecular transformation [26]. It is quite probable that steric hindrances make crosslinking in molten LDPE pro-

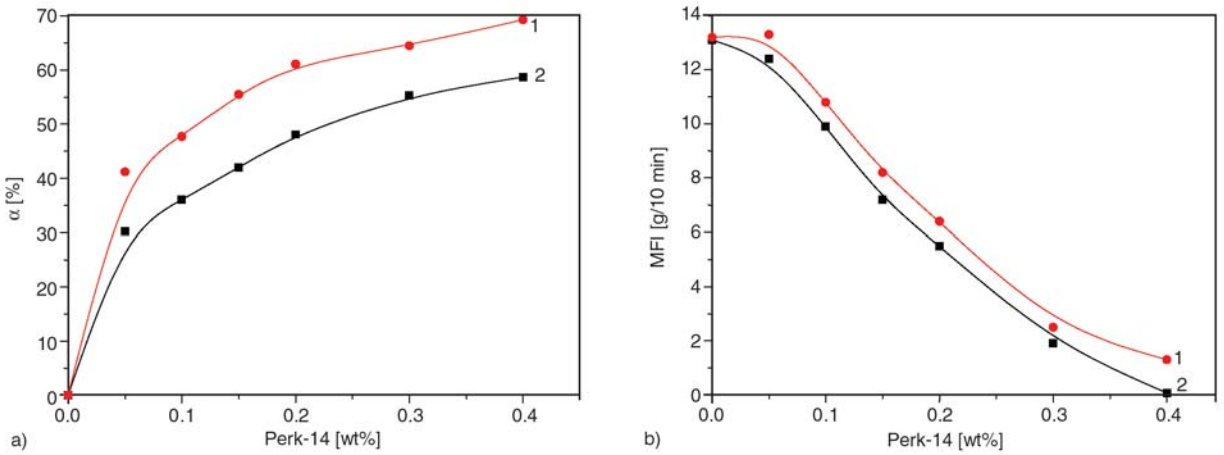

Figure 1. Effect of peroxide concentration on graft efficiency of TEDA (a) and MFI (b) for LDPE-g-TEDA (1) and mLLDPE-g-TEDA (2)

ceed less actively than in molten mLLDPE which has a more linear structure [26].

Crosslinking reactions lead to a higher viscosity of molten mLLDPE-g-TEDA compared with LDPE-g-TEDA. A higher viscosity can be harmful for the grafting reaction of a monomer; the rate of this reaction much depends on mobility of macromolecules in melt. On increasing the molten polymer viscosity, diffusion the monomer being grafted onto macroradicals becomes difficult. These macroradicals are formed from hydrogen atoms detached from macromolecules by primary free radicals which generated at thermal decomposition of the initiator. Probably for this reason the grafting rate of TEDA onto mLLDPE is lower than that onto LDPE (Figure 1).

Figure 2 shows that TEDA grafted onto both PE's causes changes in IR-spectra at 1600–1900 cm^{-1}, and new bands appear to indicate presence of oxygen-containing functional groups in the macromolecular structure. The band at 1710 cm^{-1} (Figure 2), unavailable in the spectra of the virgin PE, belongs to valence oscillations of carbonyl groups C=O in the structure of carboxyl groups.

The presence of this band in IR-spectra, after films of both PE's have been extracted in acetone, is an indication of the fact that some part of TEDA forms chemical links with macromolecules. In addition to the absorption band at 1710 cm^{-1}, there are peaks at 1760–1880 cm^{-1} in IR-spectra of PE-g-TEDA. The absorption bands are indicative of cyclic anhydride groups resulting from TEDA grafting onto macromolecules. Existence of grafted anhydride in the PE-g-TEDA is supported by a change in the character of the IR-spectra after the film samples have been treated by water: boiling of the films for 3 h transformed the anhydride groups to carboxylic ones; the absorption bands at 1790 cm^{-1} and

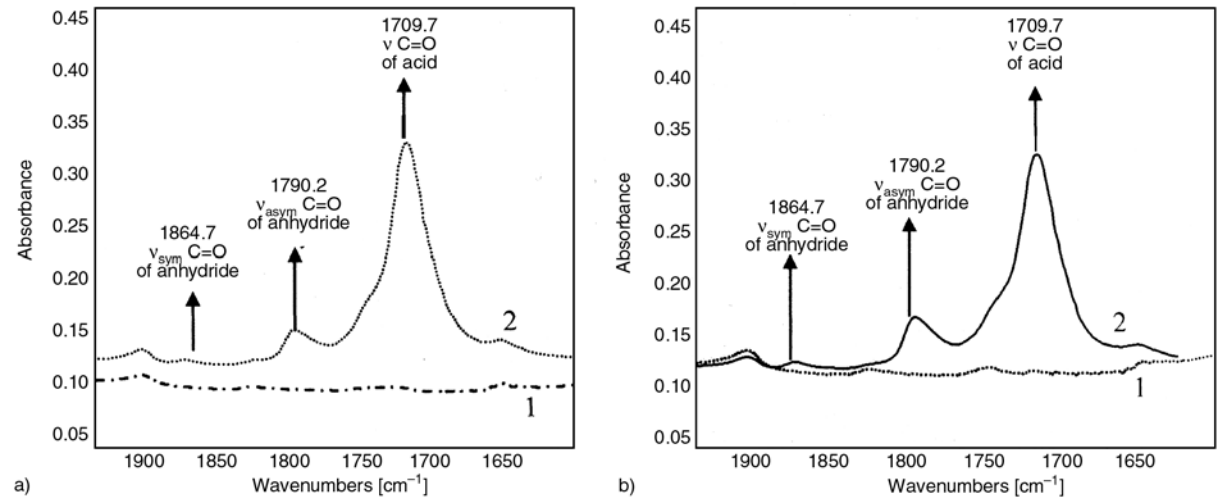

Figure 2. IR-spectra for (a) LDPE (1) and LDPE-g-TEDA (2) and (b) mLLDPE (1) and mLLDPE-g-TEDA (2)

1865 cm^{-1} disappeared. The TEDA is a transisomer, and it cannot form cyclic anhydride in a free state, because carboxylic groups are oriented in different directions with respect to double bonds.
Anhydride can be formed after TEDA has been attached to PE macromolecules or free radicals, when the double bond opens and carboxylic groups can approach each other to react and split out the water. As IR-spectra of PE-g-TEDA differ from those of initial PE by presence of new absorption bands at 1600–1900 cm^{-1} frequencies caused by valence oscillations of carbonyl C=O that belongs to carboxylic or anhydride groups, the grafting efficiency has been determined as a ratio of total bands area of carbonyl absorption (calculated per unit of the film thickness) before and after films extraction with acetone.

3.2. Analysis of double bonds transformations at PE functionalization

Because the chemical structure of the two polymers includes unsaturated groups capable of participating in the reactions of grafting, crosslinking and other transformations, it was of particular interest to analyze their change in the course of LDPE and mLLDPE functionalization. Quantitative variations in the unsaturation character of PE, that occur during TEDA grafting, are evident from the IR-spectra compared for pure and modified polymers (Figure 3 and Table 2). In the pure LDPE spectra, the vinylidene absorption band is more intensive at 888 cm^{-1}, but in LLDPE, the vinyl absorption band is more intensive at 909 cm^{-1}. These differences are explained by characteristic properties of ethylene polymerization with different catalysts [23]. The coefficients of extinction are similar for these groups [27], therefore, the difference observed in band intensities describes their concentration in PE.

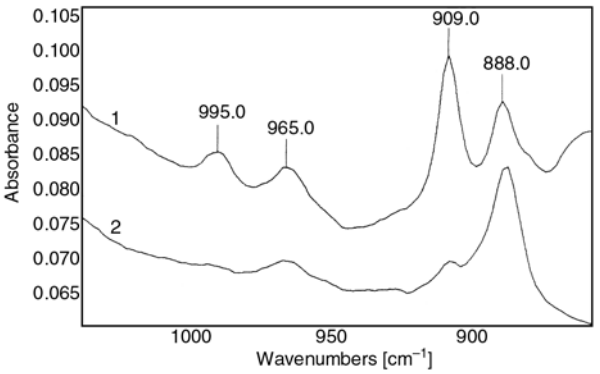

Figure 3. IR-spectra of mLLDPE (1) and LDPE (2) at unsaturated absorption region

Analysis of IR-spectra shows that at grafting of TEDA onto LDPE and mLLDPE, an increase in peroxide initiator concentration causes a reduction in vinylidene as well as vinyl groups. At the same time, the content of *trans*-vinylene groups increased (Table 2). Consequently, the free-radical grafting of TEDA onto PE changes the unsaturation nature and macromolecular structure. It should be noted, that despite an increased concentration of certain double bonds, the total unsaturation in PE-g-TEDA decreases in comparison with both types of original PE (Table 2). This fact shows that some portion of unsaturated bonds is spent in grafting and side processes (Figure 4). In Table 2, the content of double bonds of certain types is expressed in percent with respect to the total unsaturation being a sum of integral intensities of absorption bands of all unsaturated groups. For an easier understanding, the total unsaturation of initial LDPE and mLLDPE is taken to be 100%. The %-ratio of PE-g-TEDA total unsaturation to the unsaturation of the initial PE allows to state unambiguously that double bonds participate in the reactions taking place at functionalization. If the contribution of individual types of double bonds to the total unsaturation is known, it

Table 2. Unsaturation in PE as changed by TEDA grafting*

Perk-14 concentration [wt%] for producing PE-g-TEDA	Double bonds content [%] in original and functionalized PE			
	Vinylidene	Vinyl	*trans*-Vinylene	Total unsaturation
0.00	31.8 (82.7)	47.6 (4.0)	20.6 (13.3)	100.0 (100.0)
0.05	31.2 (74.1)	46.0 (3.7)	22.4 (13.9)	99.6 (91.7)
0.10	29.0 (71.4)	44.7 (3.6)	23.2 (14.8)	96.9 (89.8)
0.15	27.0 (70.6)	43.4 (3.6)	25.0 (15.0)	95.4 (89.2)
0.20	26.1 (69.2)	42.7 (3.3)	26.1 (16.5)	94.9 (89.0)
0.30	25.9 (66.0)	39.8 (3.1)	28.3 (19.8)	94.0 (88.9)
0.40	24.3 (65.5)	37.2 (2.8)	31.0 (20.4)	92.5 (88.7)

Note*: Double bond contents: figures outside brackets are for mLLDPE-based materials; those inside brackets, for LDPE -based materials

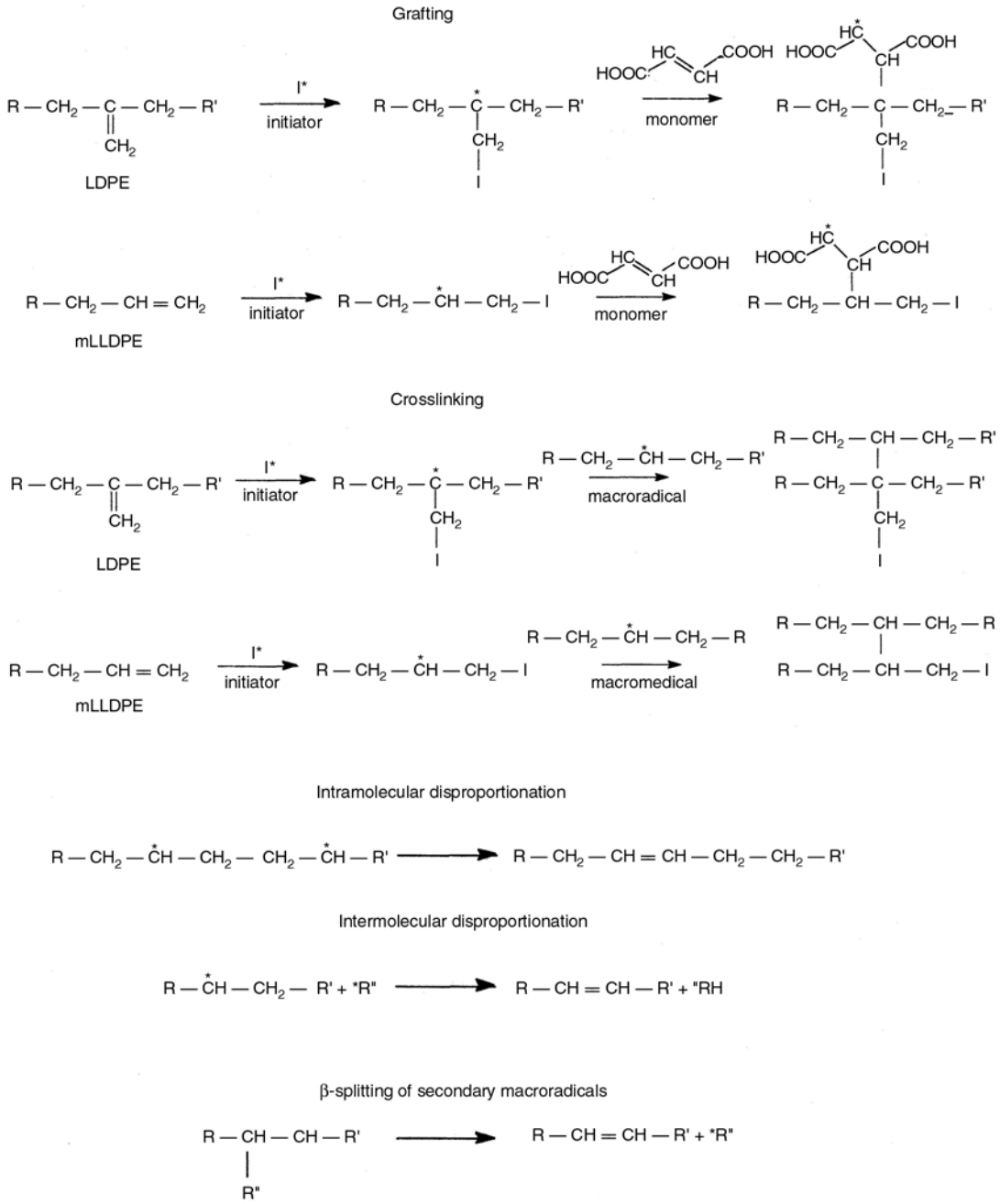

Figure 4. Suggested reactions for grafting monomer onto double bonds of LDPE and mLLDPE, crosslinking and formation of *trans*-vinylene groups

is possible to judge about their reactivity and degree of transformations.

The FTIR-spectroscopy findings concerning changes in unsaturation of PE during functionalization allow making some assumptions about chemical reactions taking place in free-radical grafting of a monomer. It is worth mentioning that the mechanism of monomer grafting onto PE has been understood inadequately, and numerous researchers treat it using general theoretical propositions about free-radical chain reactions. There is agreed upon information, that at free-radical grafting of monomers onto PE, two reactions occur: a major reaction of attaching the monomer to a macrochain and a side reaction of macroradical recombination that leads to macromolecular crosslinking. The occurrence of these reactions has been supported by FTIR- and NMR-spectroscopies and by rheological measurements made on molten grafted products [18].

The results of FTIR-spectral analysis, of how unsaturation varies in functionalized PE, allow a suggestion that free-radical grafting of TEDA onto

PE leads, besides acid grafting and macromolecular crosslinking, to a number of other macromolecular transformations. For example, an increase in *trans*-vinylene concentration, irrespective of PE type, is indicative of intra- and intermolecular disproportionation, along with β-splitting of secondary radicals (Figure 4).

It should be mentioned, that β-splitting of macroradicals during TEDA grafting onto LDPE and mLLDPE is an important characteristic of this process. Reactions of β-splitting of macroradicals are typical of free-radical grafting of polar monomers onto PP [18]. They result in a decreased molecular weight and viscosity of this polymer. For PE, on the contrary, an increased viscosity is typical. This fact indicates that recombination of macroradicals dominates over their disintegration. It was impossible to follow β-splitting via analysis of rheological properties of a modified PE. The same is true of disproportionation reactions which do not cause serious variations in polymer rheological properties. These reactions can only be ascertained by analyzing characteristic changes in the unsaturation of a functionalized PE.

Thus, FTIR-spectroscopy data on variations in unsaturation of PE functionalized by free-radial grafting of TEDA onto its macromolecules represent important information for more profound understanding of the grafting mechanism for polar monomers onto macromolecules in the course of reactive extrusion.

3.3. Results of DSC analysis

Analysis of data in Table 3 can reveal a characteristic influence of functionalization on PE crystallizability. The melting temperatures of virgin and functionalized PE's containing a peroxide between 0.05 and 0.2 wt%, are close; only with a higher peroxide initiator concentration (up to 0.3 to 0.4 wt%) T_m values become somewhat lower. The crystallization temperature and heat of grafted products, obtained with 0.05–0.2 wt% of the initiator exceed respective values for the original PE.

Analysis of DSC-data allows a suggestion that TEDA grafted in the presence of small (up to 0.2 wt%) concentrations of a peroxide, at which few cross intermolecular bonds are probably formed, facilitates polymer crystallization. A higher peroxide content in reacting systems induces an extra viscosity rise in molten PE-g-TEDA; as a result, crystallization becomes hindered, which manifests itself in a lower enthalpy of crystallization (degree of crystallinity), as well as lower melting and crystallization temperatures.

3.4. High-elastic properties of PE-g-TEDA melts

The fitness of polymers and their blends for processing by one or another technology depends not singly on their viscosity but on viscoelastic properties of their melts as well. The latter are characterized, first of all, by strength and swelling of the melt jet [28].

Swelling of an extrudate jet happens owing to normal stresses (Weissenberg effect) caused by applied shear stresses. The swell of extrudate usually enlarges with shear rate when the melt moves through the die and the temperature becomes lower [29–31].

The strength of polymer melt is an important characteristic of extruded and extrusion-blown materials. It much depends on the viscosity, high-elasticity properties of melts, molecular weight of polymers, temperature and other technological parameters [29]. Data on swelling effect of melt jet and the strength of melt are important when choosing a design for the moulding tools, as well as technological parameters of processing, to ensure production of high-quality items.

Table 3. Thermal properties of initial and functionalized mLLDPE and LDPE

Peroxide content [wt%]	mLLDPE-g-TEDA			LDPE-g-TEDA		
	T_m [°C]	T_{cr} [°C]	ΔH_{cr} [J/g]	T_m [°C]	T_{cr} [°C]	ΔH_{cr} [J/g]
0.00 (initial PE)	125.8	103.7	145.1	113.0	89.5	108.3
0.05	125.8	106.7	154.5	109.0	90.7	127.8
0.10	125.2	104.7	165.6	109.8	90.1	99.1
0.15	126.2	103.7	121.2	110.4	90.1	97.0
0.20	124.2	104.7	92.5	108.4	90.7	118.1
0.30	124.2	103.7	137.5	109.4	89.7	113.5
0.40	122.4	99.6	125.5	110.7	88.5	123.9

It should be noted, that despite regular studies carried out for many years, the accumulated information on swelling mechanisms and strength of polymer melts mostly refers to virgin PO and their blends [32–38]. Little information is available on functionalized PO.

Our experimental results on the effect of grafting on melt strength and swelling of molten extrudate for LDPE, mLLDPE, LDPE-g-TEDA and mLLDPE-g-TEDA are given in Table 4. It is clear that mLLDPE has lower melt strength than LDPE. Grafted TEDA improves the mLLDPE melt strength. The rise is especially significant at higher concentrations of the peroxide initiator (between 0.2 and 0.4 wt%). The melt strength values for all mLLDPE-g-TEDA compositions are several times lower against similar compositions of LDPE-g-TEDA. This great difference in melt strength between LDPE, mLLDPE and functionalized products based on these is explained by the fact that mLLDPE has narrower molecular weight distribution and more linear macromolecular structure than LDPE.

The extrudate swelling values for mLLDPE and mLLDPE-g-TEDA are also lower than for LDPE. The *B*-dependence on mLLDPE-g-TEDA composition is of an extreme nature, unlike that of σ_m of the melt (Table 4). A maximum swelling is typical of mLLDPE-g-TEDA prepared with peroxide concentrations between 0.05 and 0.2 wt%. A further increase in the peroxide content leads to *B*-reduction. This regularity is peculiar to both types of PE under consideration. A probable reason for this is the fact that with increased peroxide concentrations, macromolecules of the grafted products undergo crosslinking, which prevents the extrudate jet from swelling.

3.5. Mechanical properties of the materials

Table 5 presents results of mechanical testing of functionalized mLLDPE and LDPE. In case of LDPE, it is clear, that variations between 0.05 and 0.4 wt% of peroxide initiator in a reacting system, cause no appreciable changes in the deformation-strength properties. In case of mLLDPE-g-TEDA, on the contrary, a sharp increase (by ~50%) in mechanical strength occurs with an increased initiator concentration (0.4 wt%) against pure mLLDPE. The relative elongation of functionalized mLLDPE tends to reduce considerably.

Thus, in the course of grafting, mLLDPE experiences greater deformation-strength changes in comparison with LDPE.

4. Conclusions

Grafting of TEDA onto LDPE and mLLDPE through reactive extrusion in the presence of peroxide Perk-14 (Perk-14 concentration being varied between 0.05 and 0.4 wt%) results in grafted products; the grafting efficiency α varies between 30%

Table 4. High-elasticity properties of initial and functionalized mLLDPE and LDPE melts

Peroxide content [wt%]	mLLDPE-g-TEDA		LDPE-g-TEDA	
	σ_m [kPa]	B [rel.unit]	σ_m [kPa]	B [rel.unit]
0.00 (initial PE)	1.1	4.0	1.8	5.0
0.05	1.6	4.2	16.4	5.8
0.10	1.8	4.2	21.2	5.4
0.15	2,1	4.3	24.2	5.0
0.20	3.4	4.1	28.5	4.9
0.30	8.7	4.0	31.5	4.3
0.40	12.4	3.8	33.5	4.3

Table 5. Stress-strain properties of initial and functionalized mLLDPE and LDPE

Peroxide content [wt%]	mLLDPE-g-TEDA		LDPE-g-TEDA	
	σ_t [MPa]	ε_t [%]	σ_t [MPa]	ε_t [%]
0.00 (initial PE)	18.0	265.5	14.2	89.3
0.05	15.2	229.0	13.6	73.9
0.10	17.1	237.7	13.4	69.6
0.15	18.3	242.3	13.2	70.5
0.20	17.4	205.5	13.5	65.9
0.30	19.8	108.4	13.5	62.5
0.40	26.9	60.4	13.4	63.5

and 70%. The α-value for LDPE-g-TEDA, within the whole concentration range of Perk-14, exceeds by ~10% that for mLLDPE-g-TEDA. Grafting makes MFI of melts decrease (viscosity becomes higher) for the two polyethylenes; this effect is most pronounced for mLLDPE-g-TEDA over the entire concentration range of the peroxide, which is explained by intensification of side reactions of macromolecular crosslinking. It has been established that in the grafted product, some part of carboxylic groups are transformed to anhydride groups. During TEDA grafting, the concentration of end double bonds becomes lower and intramolecular unsaturation grows in LDPE, as well as is mLLDPE macromolecular structure. The crystallizing tendency of PE-g-TEDA varies depending on the initiator content: with Perk-14 ≤ 0.2 wt%, the crystallizability accelerates, while at higher peroxide doses it decelerates. Functionalization of the two PEs leads to a higher strength and lower swell coefficient of the melts at their leaving the capillary. The mechanical values for LDPE-g-TEDA are similar to the original LDPE, whereas for mLLDPE-g-TEDA the strength rises essentially (upto 1.5 times), but the relative elongation at break reduces 4.4 times at higher concentrations (up to 0.4 wt%) of Perk-14.

Acknowledgements

The research has been financially supported by Belarusian Foundation for Fundamental Research, Project NoT07A3–003.

References

[1] Greco R., Maglio G., Martuscelli E., Musto P., Palumbo P.: Functionalization of an EPR rubber by bulk mixing processes. Polymer Process Engineering, **4**, 253–261 (1986).

[2] Greco R., Maglio G., Musto P., Scarinzi G.: Bulk functionalization of ethylene-propylene copolymers. II. Influence of the initiator concentration and of the copolymer composition and chain microstructure on the reaction kinetics. Journal of Applied Polymer Science, **37**, 777–788 (1989).
DOI: 10.1002/app.1989.070370314

[3] Greco R., Maglio G., Musto P. V.: Bulk functionalization of ethylene-propylene copolymers. I. Influence of temperature and processing on the reaction kinetics. Journal of Applied Polymer Science, **33**, 2513–2527 (1987).
DOI: 10.1002/app.1987.070330720

[4] Greco R., Musto P.: Bulk functionalization of ethylene-propylene copolymers. IV. A theoretical approach. Journal of Applied Polymer Science, **44**, 781–788 (1992).
DOI: 10.1002/app.1992.070440505

[5] Zhang X. M., Yin Z. H., Li L. X., Yin J. H.: Grafting of glycidyl methacrylate onto ethylene-propylene copolymer: Preparation and characterization. Journal of Applied Polymer Science, **61**, 2253–2257 (1996).
DOI: 10.1002/(SICI)1097-4628(19960926)61:13<2253::AID-APP2>3.0.CO;2-B

[6] Oostenbrink A. J., Gaymans R. J.: Maleic anhydride grafting on EPDM rubber in the melt. Polymer, **33**, 3086–3088 (1992).
DOI: 10.1016/0032-3861(92)90102-3

[7] Grigoryeva O. P., Karger-Kocsis J.: Melt grafting of maleic anhydride onto an ethylene-propylene-diene terpolymer (EPDM). European Polymer Journal, **36**, 1419–1429 (2000).
DOI: 10.1016/S0014-3057(99)00205-0

[8] Pesetskii S. S., Jurkowski B., Krivoguz Y. M., Tomczyk T., Makarenko O. A.: PP/LDPE blends produced by reactive processing. I. Grafting efficiency and rheological and high-elastic properties of [PP/LDPE]-g-IA melts. Journal of Applied Polymer Science, **102**, 5095–5104 (2006).
DOI: 10.1002/app.24097

[9] Krivoguz Y. M., Pesetskii S. S., Jurkowski B., Tomczyk T.: Structure and properties PP/LDPE blends grafted with itaconic acid in the course of reactive extrusion. Journal of Applied Polymer Science, **102**, 1746–1754 (2006).
DOI: 10.1002/app.23998

[10] Premphep K., Chalearmthtlpa S.: Melt grafting of maleic anhydride onto elastomeric ethylene-octene copolymer by reactive extrusion. Polymer Engineering and Science, **41**, 1978–1986 (2001).
DOI: 10.1002/pen.10894

[11] Jurkowski B., Pesetskii S. S., Krivoguz Y. M.: Functionalization of olefin polymer and copolymer blends in the melt. in 'Polyolefin blends' (eds.: Nwabunma D., Kyu T.) Wiley, New York, 273–308 (2007).

[12] Yin J., Zhang J., Yao Y.: Melt grafting of poly(ethylene-vinylacetate) copolymer with maleic anhydride. Journal of Applied Polymer Science, **102**, 841–846 (2006).
DOI: 10.1002/app.24320

[13] Saade-Caballero H. G., Martínez-Colunga J.: Reactive extrusion process for the grafting of maleic anhydride onto linear low-density polyethylene with ultraviolet radiation. Journal of Applied Polymer Science, **113**, 3125–3129 (2009).
DOI: 10.1002/app.28273

[14] Moad G.: The synthesis of polyolefin graft copolymers by reactive extrusion. Progress in Polymer Science, **24**, 81–142 (1999).
DOI: 10.1016/S0079-6700(98)00017-3

[15] Chung M.: Functionalization of polyolefins. Academic Press, San Diego (2002).
[16] Hu G. H., Lambla M.: Fundamentals of reactive extrusion: An overview. in 'Materials Science and Technology' (eds.: Cahn R. W., Haasen P., Krame E. J.) Wiley-VCH, New York, 345–400 (1997).
[17] Xanthos M.: Reactive extrusion: Principles and practice. Hanser, Munich (1992).
[18] Al-Malaika S.: Reactive modifiers for polymers. Blackie, London (1997).
[19] Prut E. V., Zelensky A. N.: Chemical modification and blending of polymers in an extruder reactor. Uspekhi Khimii (Russian Chemical Reviews), **70**, 72–87 (2001).
[20] Pesetskii S. S., Jurkowski B., Krivoguz Y. M., Urbanowicz R.: Itaconic acid grafting on LDPE blended in molten state. Journal of Applied Polymer Science, **65**, 1493–1502 (1997).
DOI: 10.1002/(SICI)1097-4628(19970822)65:8<1493::AID-APP6>3.0.CO;2-B
[21] Pesetskii S. S., Jurkowski B., Krivoguz Y. M., Kelar K.: Free-radical grafting of itaconic acid onto LDPE by reactive extrusion: I. Effect of initiator solubility. Polymer, **42**, 469–475 (2001).
DOI: 10.1016/S0032-3861(00)00356-6
[22] Tarutina L. I., Pozdnyakova F. O.: Spectral analysis of polymers (in Russian). Khimya, Leningrad (1986).
[23] Polyakov A. V., Duntov F. I., Sofiev A. E., Tumarkin N. Ya., Kondratev Yu. N., Domareva N. M., Goldenberg A. L., Kobyakov V. M., Zernov V. S.: Low-density polyethylene. Fundamentals of commercial synthesis (in Russian). Khimia, Leningrad (1988).
[24] Garbar M. I., Akutin M. S., Egorov I. M.: Handbook of plastics (in Russian). Khimia, Moscow (1967).
[25] White J., Choi D.: Polyethylene, polypropylene and other polyolefins. Professia, St. Petersburg (2006).
[26] Jekins A. D., Ledwith A.: Reactive mechanism and structure in polymer chemistry. Wiley, London (1977).
[27] Mahdavi H., Nook M. E.: Characterization and microstructure study of low-density polyethylene by Fourier transform infrared spectroscopy and temperature rising elution fractionation. Journal of Applied Polymer Science, **109**, 3492–3501 (2008).
DOI: 10.1002/app.28398
[28] Kalinchev E. L., Sakovtseva M. B.: Properties and processing of thermoplastics. Khimia, Leningrad (1983).
[29] Rosato D. V., Rosato D. V.: Blow molding handbook. Hanser, Munich (1989).
[30] Vinogradov G. V., Malkin A. Ya.: Rheology of polymers (in Russian). Khimia, Moscow (1978).
[31] Koopmans R. J.: Extrudate swell of high density polyethylene. Part I: Aspects of molecular structure and rheological characterization methods. Polymer Engineering and Science, **32**, 1741–1749 (1992).
DOI: 10.1002/pen.760322302
[32] Koopmans R. J.: Extrudate swell of high density polyethylene. Part III: Extrusion blow molding die geometry effects. Polymer Engineering and Science, **32**, 1755–1764 (1992).
DOI: 10.1002/pen.760322304
[33] Wong A. C-Y., Cheung V. H. K.: Elongation strength of polyethylene melt. Journal of Materials Processing Technology, **67**, 117–119 (1997).
DOI: 10.1016/S0924-0136(96)02829-4
[34] Wong A. C-Y., Liang J. Z.: Relations between die swell ratio and melt flow index. Chemical Engineering Science, **52**, 3219–3221 (1997).
DOI: 10.1016/S0009-2509(97)00115-2
[35] Wong A C-Y.: Factors affecting extrudate swell and melt flow rate. Journal of Materials Processing Technology, **79**, 163–169 (1998).
DOI: 10.1016/S0924-0136(98)00006-5
[37] Dekmezian A. H., Weng W., Gargia-Franco C. A., Markel E. J.: Melt strength of blends of linear low density polyethylene and comb polymers. Polymer, **45**, 5635–5640 (2004).
DOI: 10.1016/j.polymer.2004.03.075
[38] Guadarrama-Medina T. J., Pérez-Gonzalez J., Vargas L.: Enhanced melt strength and stretching of linear low-density polyethylene extruded under strong slip conditions. Rheologica Acta, **44**, 278–286 (2005).
DOI: 10.1007/s00397-004-0409-0

eXPRESS Polymer Letters Vol.4, No.3 (2010) 171–182
Available online at www.expresspolymlett.com
DOI: 10.3144/expresspolymlett.2010.22

Mechanical and dielectric characterization of hemp fibre reinforced polypropylene (HFRPP) by dry impregnation process

B. Kechaou[1], M. Salvia[2], B. Beaugiraud[2], D. Juvé[2], Z. Fakhfakh[1], D. Treheux[2]*

[1]Laboratoire des Matériaux Composites Céramiques et Polymeres, Faculté des Sciences de Sfax (3018), Tunisia
[2]Laboratoire de Tribologie et Dynamique des Systemes UMR CNRS 5513, Ecole Centrale de Lyon 69134 ECULLY Cedex, France

Received 14 October 2009; accepted in revised form 14 January 2010

Abstract. Natural fibres such as jute, coir, sisal, bamboo and pineapple are known to have high specific strength and can be effectively used in composites in various applications. The use of hemp fibres to reinforce the polymer aroused great interest and expectations amongst scientists and materials engineers. In this paper, composites with isotactic polypropylene (iPP) matrix and hemp fibres were studied. These materials were manufactured via the patented FIBROLINE process based on the principle of the dry impregnation of a fibre assembly with a thermoplastic powder (iPP), using an alternating electric field. The aim of this paper is to show the influence of fibre/matrix interfaces on dielectric properties coupled with mechanical behaviours. Fibres or more probably the fibre/matrix interfaces allow the diffusion of electric charges and delocalise the polarisation energy. In this way, damages are limited during mechanical loading and the mechanical properties of the composites increase. The structure of composite samples was investigated by X-ray and FTIR analysis. The mechanical properties were analysed by quasistatic and dynamic tests. The dielectric investigations were carried out using the SEMME (Scanning Electron Microscope Mirror Effect) method coupled with the measurement of the induced current (ICM).

Keywords: *polymer composites, hemp, iPP, mechanical properties, electrical properties*

1. Introduction

It is now proven that natural fibres are excellent reinforcements for composite materials. Economic and environmental reasons have generated increasing interest to use ligno-cellulosic fibres in composite systems. New environmental legislation as well as consumer pressure have forced manufacturing industries (particularly automotive, construction and packaging) to look for new materials that can substitute conventional reinforcing materials, which are non-renewable, such as glass fibre [1]. The main advantages of natural plant fibres compared to traditional glass fibres are economical viability, low density, reduced tool wear, enhanced energy recovery, reduced dermal irritation, reduced respiratory irritation and good biodegradability. Moreover these reinforcements [2–5] can reach mechanical properties such as specific strength and modulus comparable with glass fibres. Recently, natural fibres have been used to reinforce traditional thermoplastic polymers, especially polypropylene in automotive applications [6–12].

As for fibre reinforced composites, the interfacial zone plays a leading role in load transfer between fibre and matrix and consequently in the mechanical properties such as strength. Different previous studies, which focused on model or technical insulating materials, show the effect of the electric charges on the dielectric properties (such as breakdown etc.) on the mechanical properties (such as

*Corresponding author, e-mail: daniel.treheux@ec-lyon.fr

friction, wear, fracture etc.) of ceramics and polymers [13–16]. In fact, both mechanical and dielectric catastrophic effects could be due to the trapping-detrapping of electric charges on intrinsic or extrinsic structural defects [13, 14]. Previous papers have shown the significant role of the fibre/matrix interface (glass fibre *E*/epoxy matrix), on the motion of the electric charges related to the interface nature: a material that favours the diffusion of electric charges along interfaces has better mechanical and tribological properties [17, 18].

In this study, this approach is applied and focuses on composites with isotactic polypropylene (iPP) organic matrix reinforced by hemp natural fibres, fabricated by a new dry impregnation process.

2. Materials and techniques

2.1. Materials

These materials were manufactured via the patented FIBROLINE [19] process that has been based on the principle of the impregnation of a fibre assembly (dried or not dried) with a thermoplastic powder (iPP), using an alternating electric field. This process was developed in co-operation by FIBROLINE (France) and IFTH (Institut Français du Textile et d'Habillement) Lyon, France.

The application of an alternating voltage produced by electrodes creates ions between the two dielectric ones and forms plasma. These ions enter in collision with the polypropylene powder particles and charge them electrically. Following complex physical phenomena, the modification of the surface of the hemp fibres band the IPP powders can occur, that could induce an improvement of the adherence on the matrix. Ultra high fluidity iPP of Lyondell-Basell group (Moplen HP500V) with melt flow rate (MFR) of 120 g/10 min is used. The polymer pellets are micronized. The micronized powder average diameter is in the range 50–200 μm.

Before impregnation, the fibres have the form of a randomly dispersed 'non-woven (mat)' in the plane without any privileged orientation in the plane. The mat is provided by IFTH (Institut Français du textile et de l'habillement). The average diameter and length of the fibre are 26 μm and 25 mm, respectively. Two batches of composites were manufactured by Fibroline using the specific process developed by IFTH. Following preliminary tests, the 30% average fibre volume fraction was chosen to be in the range of classical short fibre GFRP density used in automotive industry (weight fraction around 40%). In this study, three samples were studied: the polypropylene (PP) matrix, composite with PP matrix and dried hemp fibre (C_D), composite with PP matrix and not dried hemp fibre (C_{ND}). For composite named C_D, the mat was dried for 72 h at a temperature of 60°C for one batch (dry) and immediately impregnated after drying. For the other system (C_{ND}) the reinforcement was used as received. The humidity content of the fibre before drying is 4%. The immediate impregnation after drying makes impossible the measurement of exact hemp humidity after drying, but the weigh loss is very weak. In both cases, fibres did not receive any specific interface treatment. All the samples were taken directly in the plates 1 or 2 mm thick,

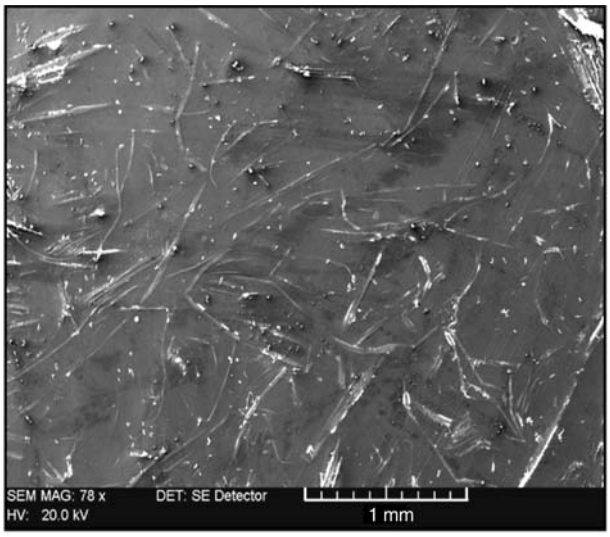

Figure 1. Microscopic observation (SEM) of the surface (C_D or C_{ND})

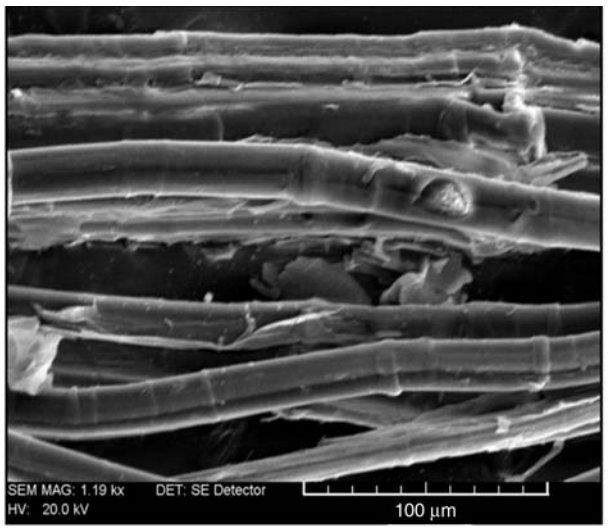

Figure 2. Microscopic observation (SEM) of the shape of the hemp fibres

obtained after the impregnation, without machining of surface.

Figure 1 presents SEM pictures to the surface of the sample that show the random distribution of the fibre. The shape of the hemp fibres is given in Figure 2.

2.2. Characterization methods

Physicochemical characterizations by FTIR and X-ray were carried out for comparing the structure of our composites, obtained by dry impregnation, with the results of the literature which use traditional processes.

2.2.1. Infra-red spectroscopy (FTIR)

The spectra were obtained with a Perkin-Elmer spectrum one FT-IR spectrometer working in Attenuated Total Reflectance mode (ATR) performing a total of 8 scans and having a resolution of 4 cm^{-1}. All ATR spectra were plotted in transmittance vs. wave number. The analyzed zone is 3 mm^2.

2.2.2. X-ray diffraction (WAXS)

X-ray diffraction analyses of materials were performed at room temperature by using a Nonius FR590 diffractometer (operating at 30 kV and 15 mA) with a CuK_α monochromatic radiation ($\lambda_{K\alpha} = 0.154$ nm). The scans were achieved within a range from 5 to 50° (2θ) with a scanning step of 0.03° in symmetrical geometry (Bragg-Brentano configuration). The spot size was about 10 mm high and 1 mm wide.

2.2.3. Dynamic Mechanical Analysis (DMA)

Dynamic mechanical tests were carried out with a DMA 50 analyzer from 01 dB-Metravib working in the tension-compression mode. The value of 0.01% for the strain magnitude was chosen that is in the linear domain of viscoelasticity of the material. The samples were thin rectangular strips that have dimensions of about (35×5.8×1) mm^3. Measurements were performed in isochronal conditions at 10 Hz, at a rate of 2°C/min and the temperature range is –100 and 130°C. This setup measured the complex tensile modulus E^*, i.e. the storage, E', and the loss, E'', as well as their ratio (E''/E'), i.e. tanδ.

2.2.4. Monotonous flexion test

The three-point bending monotonic tests, using an INSTRON testing machine (4300 type), allowed us to determine the apparent modulus (E), the maximum stress (σ_{max}) and the maximum strain ε_{max} [%]. The samples were about 100 mm long, 10 mm wide and 2 mm thick. The span to depth ratio (L/h) is greater than 20 in order to minimize shear stress. The tests were performed at 2 mm/min, under ambient conditions (test temperature: 23°C; relative humidity: 50%).

2.2.5. Induced Current Method (ICM) and Scanning Electron Mirror Effect Method (SEMME)

The dielectric behaviour of insulating material is related to its aptitude to trap electric charges, i.e. to the density and energy of traps present in the material. It is also related to its capacity to diffuse electric charges without damage.

Before dielectric study, each sample was ultrasonicated in ethanol bath during 5 minutes, and dried before its introduction in the vacuum chamber of the SEM at the ambient temperature.

After the introduction of the sample into the microscope, the insulating material is charged by a focused or unfocused electron beam (LEO 440 Electron Microscopy Ltd., Cambridge, UK) during an injection time t_{inj} and a well controlled acceleration voltage V_{acc}.

Any evolution of the total electric charges in the SEM/insulating material system involves a flow of induced charges towards the ground of the SEM [20]. This evolution is recorded in the form of Induced Current I_g. This current is measured using a picoammeter (Keithley type). The curve $I_g = f$(times) permits to obtain the total quantity of charges Q_{IC}, distributed in the samples (bulk and surface) during the injection.

The injection conditions fixed for this study are: V_{acc} = 10 or 30 kV, t_{inj} = 40 or 100 ms.

The evolution of I_g during injection (Figure 3) gives information on the different steps of diffusion or trapping of charges present in the insulating sample.

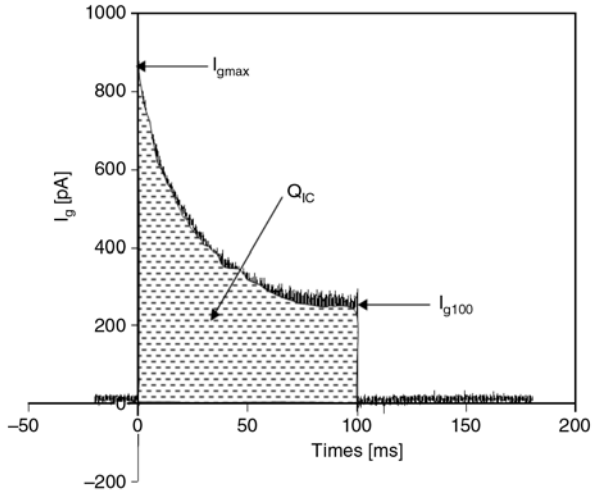

Figure 3. Parameters measured by Induced Current Method (ICM)

Different parameters can be deduced from this curve (Figure 3):

– I_{gmax}: initial current that informs on the response of material without any perturbation;
– Q_{IC}: quantity of charges distributed in the sample;
– I_{g40} or I_{g100}: value of the induced current respectively for 40 or 100 ms injection time.

The SEMME method will be performed after the injection step. The observation at lower energy (V = 100–200 V) of the irradiated zone makes it possible to put in evidence the mirror effect (Figure 4) [21, 22]. In fact negative charges Q_t locally trapped and stabilized near to the injection point can induce the deflection of incident electrons: the mirror image is a view of the SEM chamber. The quantity Q_t of trapped charges can be deduced from the slope of the linear part of the 'mirror' curve $1/d = f(V)$ according to an electrostatic law, established by Vallayer [22], relating the real diameter d' of the last output diaphragm and the apparent one, d, measured on the mirror image (Equation (1)):

$$\frac{1}{d} = \frac{4L}{d'} \cdot \frac{2\pi\varepsilon_0(\varepsilon_r + 1)}{K(h) \cdot Q_t} \cdot V \tag{1}$$

where L is the working distance of the SEM; d' the diameter of the last output diaphragm, d the apparent diameter measured on the mirror image, $K(h)$ a parameter dependent on SEM chamber and permittivity of the sample, and V the acceleration potential of the electron beam.

The comparison between Q_{IC}, measured by the ICM method and Q_t, measured by the mirror method, gives information of the charge state in the sample. In fact, if $Q_t/Q_{IC} = 1$, the charges are stabilized and trapped near the injection point. However, if Q_t/Q_{IC} tends towards 0, the charges diffuse in the sample from the injection point.

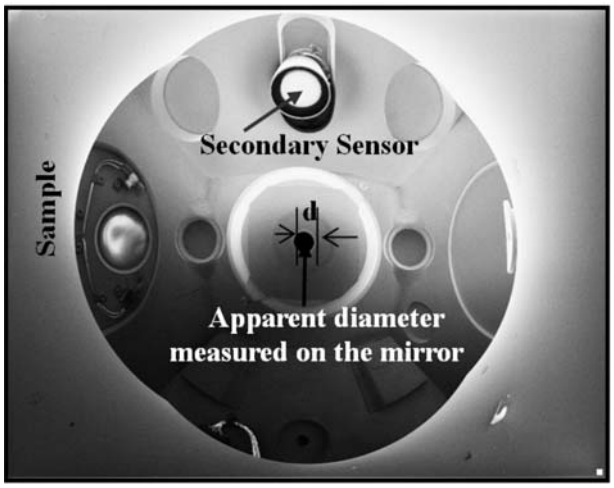

Figure 4. Mirror image

3. Results and discussion

3.1. Infrared spectroscopy measurements

Figure 5 shows the spectra of neat iPP matrix, hemp fiber mat as received, composite C_D and composite C_{ND}, obtained with infra-red spectrometer (FTIR) in Attenuated Total Reflectance (ATR) mode.

The neat matrix:

The isotactic polypropylene consists of propene repeating units (CH_2–$CH(CH_3)$) linked together.

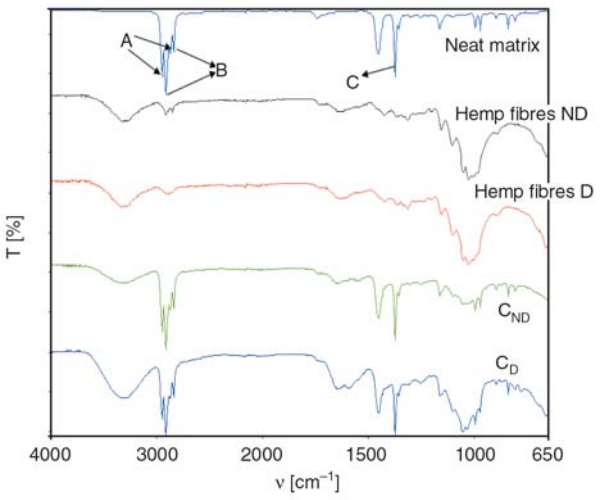

Figure 5. FTIR spectra (transmittance T vs. wave number ν) of four samples: matrix, fibre of hemps no dried and dried, C_{ND}, C_D (the scale is the same for each spectrum)

The methyl groups (–CH_3) are located on alternation with a hydrogen (H) in the backbone chain and are all on the same side. The peaks corresponding to the methyl group occur at 2953, 2873 and 1375 cm^{-1} (C). The two first peaks (A) are attributed to the stretch vibration asymmetric and symmetric of C–H. The last one is known as 'umbrella' mode (symmetric bending mode) (C). The peaks at 2913 and 2840 cm^{-1} (B) are related to methylene group (CH_2) asymmetric and symmetric C–H stretches. The peak located at 1453 cm^{-1} is due to the overlapping of the asymmetric bending mode of the (CH_3) and the methylene scissoring mode [23]. The other peaks are of less intensity, but the occurrence of the adsorption peaks at about 1160, 997, 973, and 841 cm^{-1} is in agreement with the tacticity of the polymer [24, 25]. Moreover, even though the methine groups (CH) are present in the structural unit, the peaks are not observed [23].

The hemp mat:
Hemp fibre mat was analyzed ($\%T = f(\nu)$) in the as received (not dry) and dry state. Plant fibre such as hemp contains cellulose (about 70%), non cellulosic polysaccharide (hemicellulose and pectin), lignin and wax. According to the literature [25], the native cellulose consists of long chain of (1-4)-β linked D-glucose units mostly aligned in parallel (cellulose I_β).
The spectra show the major bands classically observed in other ligno-cellulosic fibres. The broad and strong peak at about 3300 cm^{-1} [25] is characteristic of O–H stretching for hydrogen-bonded hydroxyl group in polysaccharides. The weak absorption peak observed at about 1730 cm^{-1} is characteristic of hemicelllulose. It is attributed to carbonyl group (C=O) stretch. The weak broad peak that occurs at around 1600–1650 cm^{-1} is associated with water adsorbed in cellulose [25]. The large peak with maximum at about 1030 cm^{-1} is linked with C–O vibrations in cellulose. Finally, it appears that the absence of peak at around 1500 cm^{-1} corresponding of aromatic symmetrical stretching points out that the fibres are practically free of lignin. Probably, because of the low rate of humidity (<4%), there are no obvious differences between as received and dry mats except the peak characteristic of waxes [26] (CH_2 symmetrical stretching) at about 2850 cm^{-1}.

The composites:
The spectra of composite PP/hemp fibres (C_D or C_{ND}) are finally analyzed. These spectra show that PP matrix is modulated by the presence of hemp fibres i.e. there is no new peak appearing in the composites and thus no bond formed between the matrix and the fibres. Although the two spectra are similar, it can be noted that the amplitudes of the peaks at 3300 and 1030 cm^{-1} are higher for C_D. This phenomenon is possibly due to the fact that the surface of the C_D composite exhibits more cellulosic fibre characteristic than C_{ND} composite [27].
The literature [28, 29] reports that the volume crystallinity index is proportional to A_{841}/A_{973} ratio where A_{973} is the absorbance peak intensity at 973 cm^{-1} that is insensitive to the amorphous/crystalline ratio of isotactic polypropylene whereas A_{841} is the intensity of the band at 841 cm^{-1} linked to crystallinity content. For the neat matrix and the two composites this ratio is close and thus the crystallinity rate too.
Thus, the dry impregnation process does not modify basically the results observed classically.

3.2. X-ray analysis

Figure 6 illustrates the WAXS patterns in conventional mode (θ–2θ) of the different samples. The peaks of semicrystalline polypropylene and an

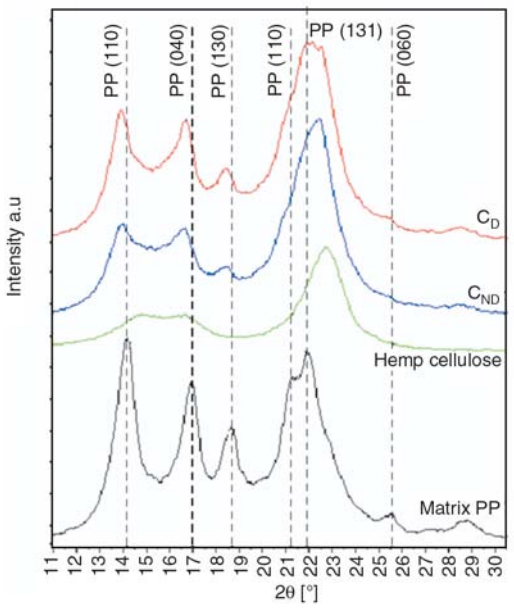

Figure 6. X-ray diffraction patterns of matrix, hemp fibres and composites. The figure is limited to the angular field presenting peaks of significant intensity.

amorphous background noise between 12 to 24° (in 2θ), were observed. These peaks, in accordance with JCPDS 00-050-2397, appear at 14.16, 17.06, 18.65, 21.34 and 21.91° (in 2θ) that are characteristics of the α-monoclinic crystal structure and corresponding to the (110), (040), (130), (111) and ($\bar{1}$31) planes, respectively. No peak occurs at 2θ = 16° that is characteristic of the β-hexagonal phase.

The XR diffractogram of hemp fibres shows three peaks at 15; 16.47 and 22.77° (in 2θ) corresponding to the (1$\bar{1}$0), (110), (002) planes of the I_β cellulose structure [30] respectively as the cellulose is expected to be the only crystalline constituent in plant fibre. Using synchrotron radiation and neutron diffraction, Nishiyama *et al.* [31] specifies that the structure consisted of two parallel chains having slightly different conformations and organized in sheets packed in a 'parallel-up' fashion, with all hydroxymethyl groups.

For composites, the presence of hemp fibres modulated the PP diffractograms. As for neat matrix, no hexagonal phase (β) is detected. Indeed β-hexagonal form could appear in HFRPP according to the processing [12]. The broad peak at 2θ ~ 22.5° is due to the overlapping of the diffraction peaks of the PP-crystals at 2θ = 21.34 and 21.91° with the peak of the cellulose-crystals at 2θ = 22.77°. The incorporation of hemp fibres involves a shift to lower 2θ of the other polypropylene peaks that corresponds to a modification of the lattice parameters of the monoclinic α phase of the polypropylene matrix, most probably due to internal stress.

3.3. Dynamic mechanical thermal properties

Experimental results of mechanical dynamic tests, are represented in Figures 7 (loss factor tanδ) and 8 (tensile storage modulus E') for the neat matrix and the two composites at 10 Hz.

The three classical relaxations of polypropylene are observed named γ, β and α in order of increasing temperature [32]:

– Relaxation γ (T_γ ~ –65°C for neat PP) is related to the local motions in the amorphous phase.
– Relaxation β (T_β ~ 10.5°C, for neat PP) is associated with the glass transition, that is to long distance molecular motions.
– Relaxation α (T_α = 100°C for neat PP), that appears only on neat matrix spectrum is attributed to the presence of the crystalline phase. In fact, this relaxation is not found on the curves of tanδ of an atactic PP (amorphous) and it is known to be sensitive to modifications of crystallites by thermal or mechanical treatments (annealing, drawing). Even this relaxation is a post-T_g transition the activation energy (~130 kJ/mole) is lower than the activation energy of α-relaxation ~ (330 kJ/mole) and follows an Arrhenius law that implies less cooperative motion than α-relaxation. The mechanisms generally proposed for explaining this relaxation include conformational defect diffusion within the crystal, and interaction between amorphous and crystalline phases, the translation of chains in the crystal part involving modification of chain segments at the interface between the two phases [32, 33].

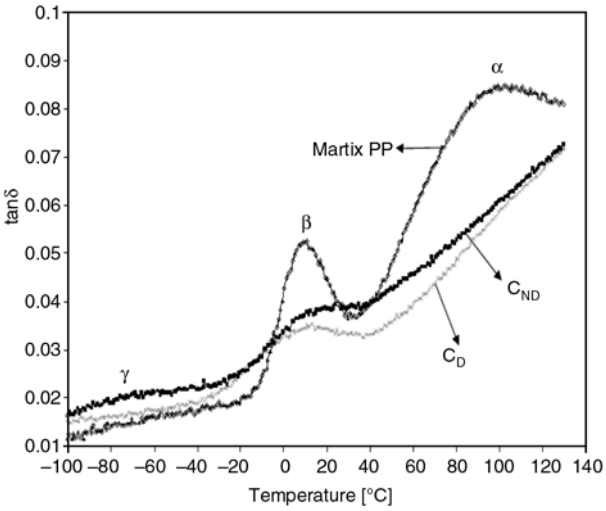

Figure 7. Mechanical loss factor log(tanδ) vs. temperature of the neat matrix and the two composites at 10 Hz

The incorporation of the hemp fibres increases the storage modulus of the matrix whatever the temperature range. Indeed the modulus of composite is determined by the moduli of the constituents (fibre and matrix) but also by the fibre-matrix interaction especially in the case of off-axis and randomly oriented fibre composite. The slightly higher increase of modulus for composites with dried fibres suggests improved adhesion between fibre and matrix probably due to better wetting associated to the wax removal, leading to the slightly better transfer of stress from matrix to the fibre in the case of composite with dried fibre. In fact, the modulus of the fibre is about the same whatever the treatment

(50 GPa [19]). The effect of fibre-matrix adhesion on tensile modulus of such composites has been already experimentally shown in different studies [34, 35] but this factor is generally not taken into account for in the classical models [36] for which a perfect interface is considered. Therefore, the DMA results seem to indicate a medium adhesion at the interface.

Moreover as shown by Figure 7, the intensity of the β-relaxation is lowered in the composites compared to the neat matrix and a slight shift in peak temperature of the β-relaxation can be observed towards higher temperatures ($T_\beta \approx 10.5$°C for the matrix and ≈15.5°C for the composites). These behaviours cannot be attributed to an increase in crystallinity of PP matrix since IR results indicated no major modification in crystallinity index with reinforcement. That is probably related to the reduction in the molecular mobility due to the reinforcing effect of the fibres that indicates the applied stresses are expected to be easily transferred from the matrix. The decrease of the amplitude of the relaxation associated to the glass temperature is more important for C_D composite that is consistent with enhanced polymer-fibre interaction.

Hence, the non-appearance of the α-relaxation peak in the tanδ spectra of the composites in the studied temperature range can be related to higher constraints through the interlamellar regions linked the presence of fibres that seems to be consistent with WAXS results that suggest crystal rearrangement and internal stresses.

3.4. Monotonous flexion test

The Figure 9 shows typical flexural stress strain curves for the neat matrix and the two composites obtained from the three-point bending experiment at room conditions. Three characteristic zones are pointed out:

– A linear zone corresponding to the elastic behaviour of the material.
– A nonlinear zone associated to the appearance of the plastic deformation and damage.
– A zone of failure. In all the cases the material (neat matrix and composites) beams fail from the tensile side. It can be noted that both composites can undergo loading after the maximum stress to a large extent whereas for the neat matrix, the failure is more sudden.

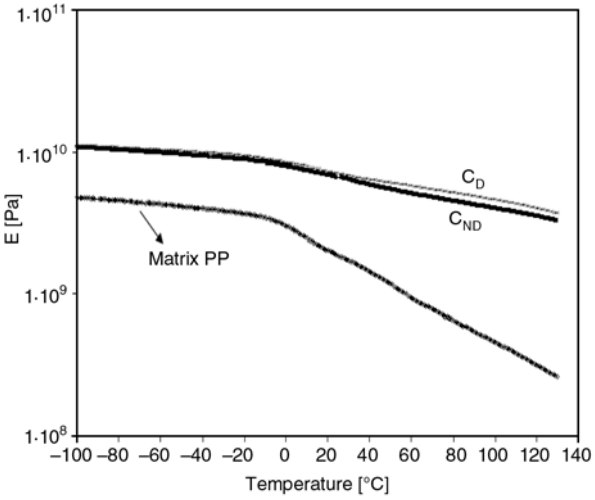

Figure 8. Tensile storage modulus (E') vs. temperature of the neat matrix and the two composites at 10 Hz

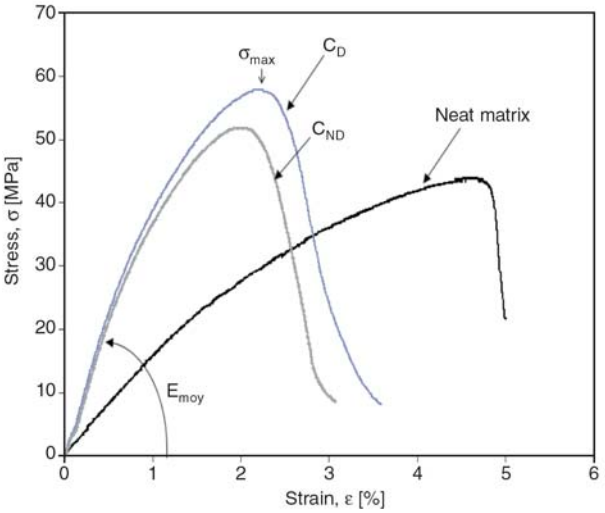

Figure 9. Typical curve of three-point bending, strain-stress for the neat matrix and the two composites at room conditions

Table 1. Flexural Mechanical properties of the tested composite materials E_{moy} apparent flexural modulus, σ_{max} and ε_{max} flexural stress and flexural strain respectively at maximum of the stress-strain curve (the standard deviations are in parentheses)

	E_{moy} [GPa]	σ_{max} [MPa]	ε_{max} [%]
Matrix	1.57 (± 0.10)	43.8 (±1.4)	4.55 (±0.25)
C_{ND}	4.54 (± 0.45)	51.8 (±1.2)	2.11 (±0.22)
C_D	4.51 (± 0.44)	56.8 (±2.7)	2.34 (±0.15)

The main mechanical properties determined by flexural testing are given in Table 1 (average values on five samples). Improvements in both maximum flexural stress and modulus are well noticed for the two composites.

The flexural modulus increases from 1.57 GPa for the neat polypropylene matrix to about 5.50 GPa for the composites. However, conversely to DMA

tensile storage modulus results, there is no difference within experimental scatter between flexural moduli of the C_D and C_{ND} composites. This result can be explained in term of the non-uniform stress distribution through thickness in the case of three-point bending loading.

The composite reinforced with dried fibres displays (C_D) slightly higher stress at maximum compared to composites made with as received fibres (C_{ND}), probably linked to an improved fibre/matrix adhesion.

SEM micrographs of typical fracture feature is given in Figures 10 (C_{ND}) and 11 (C_D). The comparative analysis of the fracture features highlights some traces of matrix remaining on the fibres after extraction (pull-out). These observations suggest a medium transfer efficiency or fibre/matrix adhesion. However the phenomenon is clearer for the composite with dried fibres (Figure 11) that is consistent with DMA results.

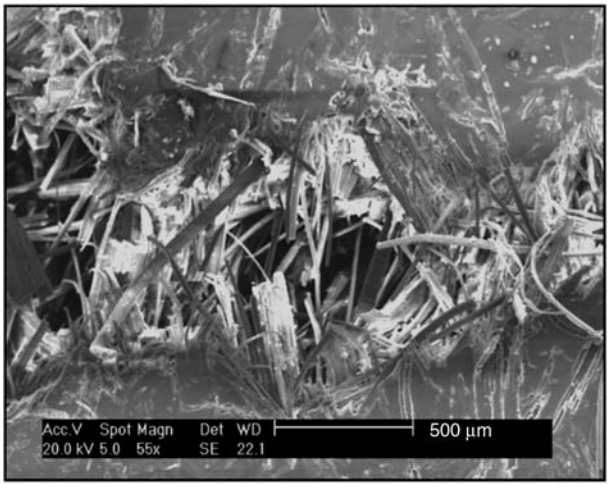

Figure 10. Examples of fracture topographies (C_{ND}) pull out and matrix rupture

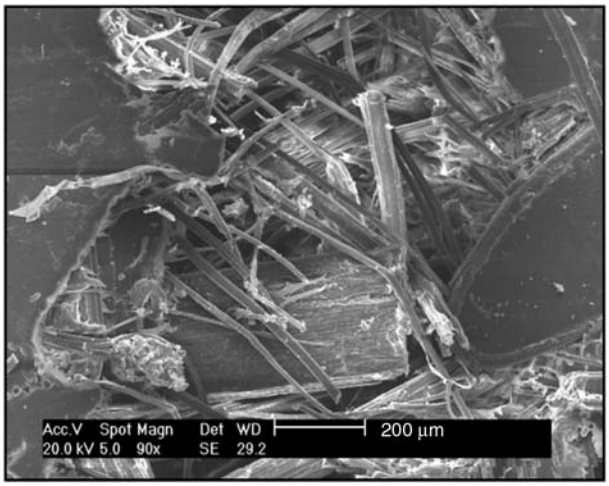

Figure 11. Fracture topography (SEM): matrix traces on fibres (C_D)

3.5. Mirror and Induced Current Methods (ICM)

To characterize the behaviour of the samples studied in this work, with regard to the presence of the electric charges, the 'mirror method' was used coupled with measurement of induced current.

In a first stage, the injection of the electrons was carried out under an accelerating voltage of 30 kV in focused mode. After injection, for low observation tension, the injected zone shows a degradation of material as proved in Figure 12 (SEM micrographs a-b).

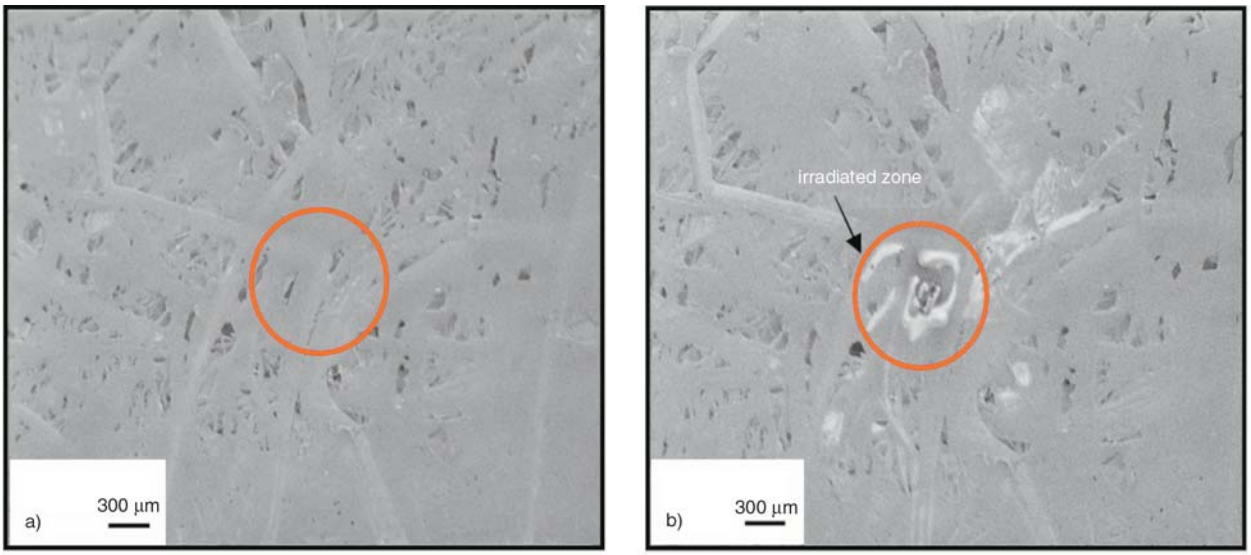

Figure 12. Total damaging of the irradiated zone (C_D or C_{ND}): (a) before injection, (b) after injection

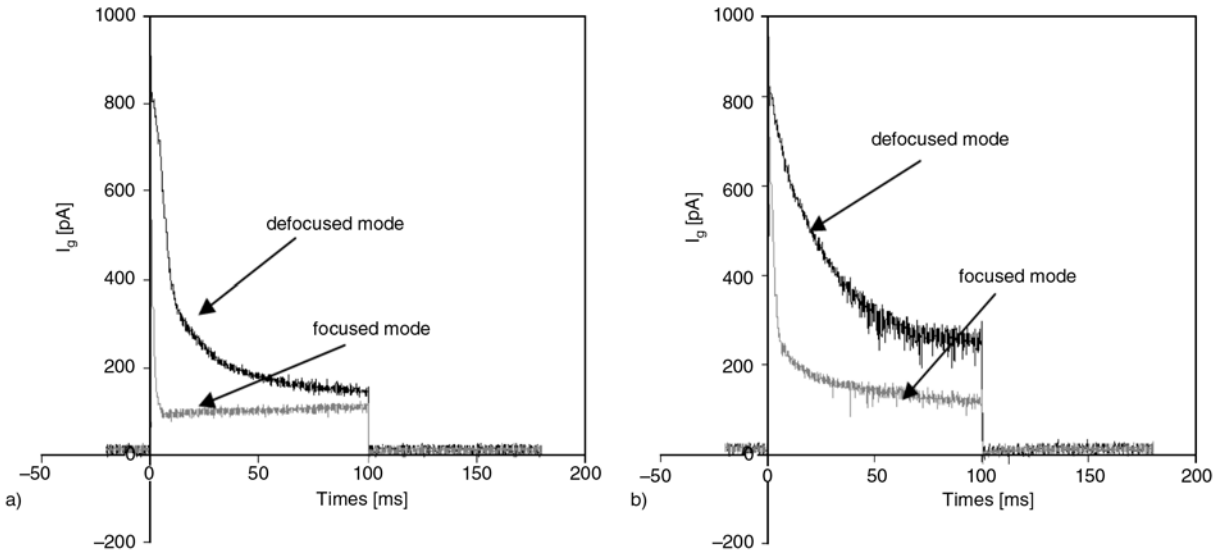

Figure 13. Curves $I_g = f$(time) in defocused or focused mode: (a) matrix PP, (b) C_D composite

For these injection conditions, a collective electric charges detrapping occurs, inducing a local destruction of the material (explosive emission) [37].

Therefore, a voltage of 10 kV was chosen, using focused or unfocused mode (diameter of injection zone: 70 μm); the injection time is 100 or 40 ms.

Figure 13 represents the ICM curves $I_g = f$(time) in defocused or focused mode for the matrix and for the C_D (similar C_{ND}).

ICM curves present the same shape in focused or defocused modes, (sharp slope of the curve at the beginning of injection and a plateau at the end of injection). However, for the defocused mode, more fibres are concerned favouring the flow of the electric charges, inducing a weaker slope at the beginning of the injection and higher current intensity at the end.

Figure 14 represents the ICM curves $I_g = f$(time) in defocused mode for the three samples: matrix PP; C_D and C_{ND}. During the injection step, some unstable micro relaxations appear (time > 50 ms) only for the C_D and C_{ND} composite (Figure 14). This phenomenon can probably protect the composite from catastrophic damages.

Consequently, following measurements were carried out using a 10 kV accelerating tension in defocused mode and t_{inj} = 40 ms. Figure 15 represents the evolution of the ICM current $I_g = f$(time) for the three samples and Table 2 summarizes the parameters measured by ICM and SEMME methods.

Based on ICM measurements, we can note that the incorporation of dried or not dried fibres in PP matrix increases the material capacity to store elec-

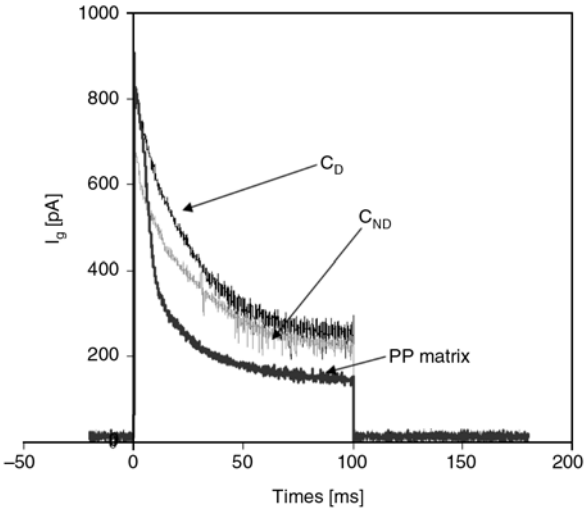

Figure 14. $I_g = f$(time) in defocused mode for the three samples, PP matrix, composite C_D and composite C_{ND} for t_{inj} = 100 ms

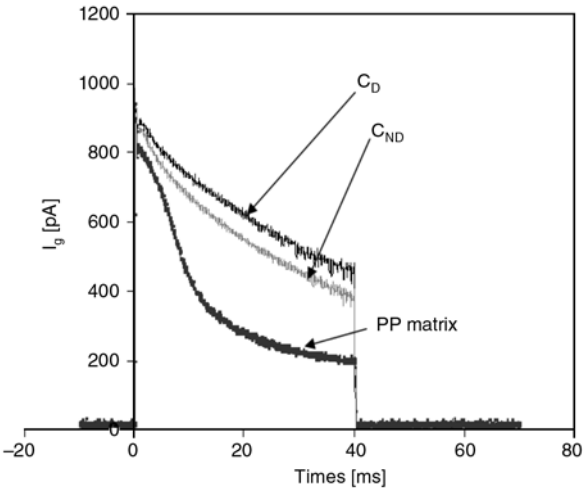

Figure 15. $I_g = f$(time) in defocused mode for the three samples, PP matrix, composite C_D and composite C_{ND} for t_{inj} = 40 ms

Table 2. Parameters measured according to the ICM curves and the mirror method for the three samples: matrix PP, composite C_D and composite C_{ND} for t_{inj} = 40 ms

	Matrix PP	C_D	C_{ND}
I_{gmax} [pA]	817 (±9)	898 (±10)	867
I_{g40} [pA]	206 (±9)	435 (±30)	406 (±36)
Q_{IC} [pC]	14.73 (±0.4)	25.65 (±3)	23.31 (±1)
Q_t [pC]	12.8 (±0.1)	6 (±0.1)	9.51 (±0.1)
V_d [V]	1800	1200	1600
Q_t/Q_{IC}	0.826	0.234	0.37

tric charges (Q_{IC} composites > Q_{IC} matrix), but with an easier diffusion of the charges (I_{g40} composites > I_{g40} matrix) (Figure 15 and Table 2). At the beginning of the injection, the slope of the ICM curve is stronger for the matrix than for the composites and, for the matrix, the charges are more localised, near the injection zone.

Confirming the results obtained by the ICM method, the observation at low voltage, after injection of electrons, shows stable mirror images. Figure 16 represents the mirror curves $1/d = f(V)$, for the three materials. The potential V_d of disappearance of the mirror is 1200 V for the two composites (outspread of electric charges) as opposed to (1800 V) for the matrix (electric charges remains more stable and localised). This can, also, be deduced by the ratio Q_t/Q_{IC} that represents the stability of the charges which decrease under the effect of incorporating fibres in the PP matrix

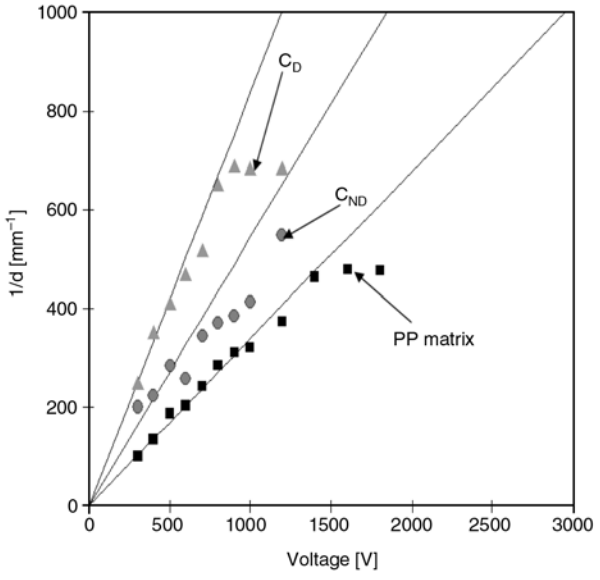

Figure 16. $1/d = f(V)$ for the three samples, PP matrix, composite C_D and composite C_{ND} for t_{inj} = 40 ms

(Table 2). The comparison between the dielectric measurements (Table 2) shows that the composites presents high aptitude to spreading of the electric charges (high current at the end of the injection, faster disappearance of the mirror image and Q_t/Q_{IC} weak) compared to the matrix. We can think that the incorporation of fibres or the creation of the fibre/matrix interface supports this phenomenon of delocalization of the charges and, consequently, the reduction in the polarization energy. Such a phenomenon has the effect of increasing the mechanical properties as seen previously for composites with epoxy matrix reinforced with glass fibres E [18].

In addition, a drying of fibres before the introduction into the composite is favourable. But, the observed difference remains weak compared to the composites including not dried fibres.

4. Conclusions

This work enabled us to confirm the correlation between dielectric behaviour and mechanical properties of polymers reinforced by natural fibres.

Several techniques are used to characterize the samples and the fibre/matrix interface:

– From FTIR analysis, it can be concluded that there is no chemical bond formed between the matrix and the fibres, and that the crystallinity rate is similar for neat PP and composites.
– X-ray diffraction analysis of materials shows that the presence of hemp fibres modifies the lattice parameter of polypropylene in composite materials due to internal stresses.
– As for continuous E-glass fibres [18], tests performed on hemp fibre reinforced composites prove that hemps fibres modify the dielectric response of the polymeric matrix. The fibres, or more probably the fibres/matrix interfaces, allow a diffusion of the electric charges which delocalizes the polarization energy. The drying of fibres is well differentiated by IR, X-ray, ICM and SEMME methods, because the drying modifies the fibre/matrix interface and, then the trapping and/or the motion of the electric charges.
– Consequently, from the mechanical point of view, the drying of fibres is beneficial since it reinforces the fibres/matrix load transfer which, in addition, favours the diffusion of the electric charges.

In conclusion we see that it is possible to modify the characteristic of composite by the nature of fibre and the interfaces.

Acknowledgements

The authors particularly thank Eric Forest and Laurence Caramaro for the Fibroline Company for the fabrication of the samples used in this study.

References

[1] Lee N-J., Jang J.: The effect of fibre-content gradient on the mechanical properties of glass-fibre-mat/polypropylene composites. Composites Science and Technology, **60**, 209–217 (2000). DOI: 10.1016/S0266-3538(99)00122-0

[2] Bledzki A. K., Gassan J.: Composites reinforced with cellulose base fibres. Progress in Polymer Science, **24**, 221–274 (1999). DOI: 10.1016/S0079-6700(98)00018-5

[3] Leao A. L., Rowell R., Tavares N.: Applications of natural fibres in automobile industry in Brazil – Thermoforming process. in 'Science and technology of polymers and advanced materials, emerging technologies and business opportunities' (eds.: Prasad P. N., Mark J. E., Kandil S. H.: Kafafi Z.) Plenum Press, New York, 755–761 (1998).

[4] Robson D., Hague J., Newman G., Jeronomidis G., Ansell M.: Survey of natural materials for use in structural composites as reinforcement and matrices. Woodland Publishing Ltd., Abingdon (1996).

[5] Mohanty A. K., Misra M., Hinrichsen G.: Biofibres, biodegradable polymers and biocomposites: An overview. Macromolecular Materials and Engineering, **276–277**, 1–24 (2000). DOI: 10.1002/(SICI)1439-2054(20000301)276:1<1::AID-MAME1>3.0.CO;2-W

[6] Wötzel K., Wirth R., Flake M.: Life cycle studies on hemp fibre reinforced component and ABS for automotive parts. Die Angewandte Makromoleculare Chemie, **272**, 121–127 (1999). DOI: 10.1002/(SICI)1522-9505(19991201)272:1<121::AID-APMC121>3.0.CO;2-T

[7] Riedel U., Nickel J.: Natural fibre-reinforced biopolymers as construction materials-new discoveries. Die Angewandte Makromolekulare Chemie, **272**, 34–40 (1999). DOI: 10.1002/(SICI)1522-9505(19991201)272:1<34::AID-APMC34>3.0.CO;2-H

[8] Peijs T.: Composites for recyclability. Materials Today, **6**, 30–35, April (2003). DOI: 10.1016/S1369-7021(03)00428-0

[9] Zah R., Hischier R., Leao A. L., Braun I.: Curauá fibers in the automobile industry – A sustainability assessment. Journal of Cleaner Production, **15**, 1032–1040 (2007). DOI: 10.1016/j.jclepro.2006.05.036

[10] IENICA Summary report for European Union- Fibre crops. August (2000).

[11] Lovins A. B., Cramer D. R.: Hypercars, hydrogen, and the automobile transition. International Journal of Vehicle Design, **35**, 50–85 (2004). DOI: 10.1504/IJVD.2004.004364

[12] Paukszta D., Borysiak S.: Structure of isotactic polypropylene in composites with natural fibres obtained in various processing methods. Fibres and Textiles in Eastern Europe, **13**, 107–109 (2005).

[13] Blaise G., Le Gressus C.: Charge trapping-detrapping processes and related breakdown phenomena. in 'High voltage vacuum insulation' (ed.: Latham R.) Academic Press, London, 330–338 (1995).

[14] Berriche Y., Vallayer J., Trabelsi R., Treheux D.: Severe wear mechanisms in Al_2O_3-AlON ceramic composites. Journal of the European Ceramic Society, **20**, 1311–1318 (2000). DOI: 10.1016/S0955-2219(99)00294-0

[15] Berroug A., Fayeulle S., Hamzaoui B., Tréheux D., Le Gressus C.: Effect of X-irradiation and friction on the properties of insulators. IEEE Transactions on Electrical Insulation, **28**, 528–534 (1993). DOI: 10.1109/14.231535

[16] Guerret-Piécourt C., Vallayer J., Juvé D., Tréheux D.: Limitation induced by electrical charges effects on micromechanisms. Wear, **254**, 950–958 (2003). DOI: 10.1016/S0043-1648(03)00299-0

[17] Kchaou B., Turki C., Salvia M., Fakhfakh Z., Tréheux D.: Dielectric and friction behaviour of unidirectional glass fibre reinforced epoxy (GFRE). Wear, **265**, 763–771 (2008). DOI: 10.1016/j.wear.2008.01.015

[18] Kchaou B., Turki C., Salvia M., Fakhfakh Z., Tréheux D.: Role of fibre-matrix interface and fibre direction on dielectric behaviour of epoxy composites. Composites Science and Technology, **64**, 1467–1475 (2004). DOI: 10.1016/j.compscitech.2003.10.016

[19] Bouzouita S., Salvia M., Ben Daly H., Forest E.: Hemp/polypropylene composites. Effects of fibre treatment on fibre and fibre/matrix interface mechanical properties (in French). Revue des Composites et des Matériaux Avancés, **19**, 25–38 (2009). DOI: 10.3166/rcma.19.25-38

[20] Temga T., Juvé D., Tréheux D., Guerret-Piécourt C., Jardin C.: Conduction and trapping of electric charges in an anisotropic material after irradiation with an electron beam: Application to TiO_2 single-crystal. Nuclear Instruments and Methods in Physics Research B: Beam Interactions with Materials and Atoms, **245**, 519–527 (2006). DOI: 10.1016/j.nimb.2005.11.151

[21] Attard C., Bigarré J., Hourquebie P.: Determination of the spatial distribution of trapped charges in insulators: Application of the electrostatic mirror method to polymers. in 'Proceeding of the 2nd Conference of Electrostatics. Montpellier, France' 77–83 (2000).
[22] Vallayer B., Blaise G., Tréheux D.: Space charge measurement in a dielectric material after irradiation with 30 kV electron beam: Application to single-crystals oxide trapping properties. Review of Scientific Instruments, **70**, 3102–3112 (1999). DOI: 10.1063/1.1149887
[23] Smith B. C.: Infrared spectral interpretation. CRC Press, Boca Raton (1999).
[24] Klopffer W.: Introduction to polymer spectroscopy. Springer-Verlag, Berlin (1984).
[25] Subramanian K., Senthil Kumar P., Jeyapal P., Venkatesh N.: Characterization of ligno-cellulosic seed fibre from *Wrightia tinctoria* plant for textile applications- An exploratory investigation. European Polymer Journal, **41**, 853–861 (2005). DOI: 10.1016/j.eurpolymj.2004.10.037
[26] Le Troëdec M., Peyratout C., Chotard T., Bonnet J-P., Smith A., Guinebretiére R.: Physico-chemical modifications of the interactions between hemp fibres and a lime mineral matrix: Impacts on mechanical properties of mortars. in '10th International Conference of the European Ceramic Society, Berlin, Germany' 451–456 (2007).
[27] Stark M. N., Matuana L. M.: Characterization of weathered wood plastic composite surfaces using FTIR spectroscopy, contact angle, and XPS. Polymer Degradation and Stability, **92**, 1883–1890 (2007). DOI: 10.1016/j.polymdegradstab.2007.06.017
[28] Sundell T., Fagerholm H., Crozier H.: Isotacticity determination of polypropylene using FT-Raman spectroscopy. Polymer, **37**, 3227–3231 (1996). DOI: 10.1016/0032-3861(96)88466-7
[29] Lamberti G., Brucato V.: Real-time orientation and crystallinity measurements during the isotactic polypropylene film-casting process. Journal of Polymer Science Part B: Polymer Physics, **41**, 998–1008 (2003). DOI: 10.1002/polb.10411
[30] Abou-Sekkina M. M., Saafan A. A., Sakran M. A., Ewaida M. A.: Effects of tempering time and tempering temperature of caustic mercerization on the spectral and electrical properties of Egyptian cotton fibres. Journal of Thermal Analysis, **31**, 791–803 (1986). DOI: 10.1007/BF01913550
[31] Nishiyama Y., Langan P., Chanzy H.: Crystal structure and hydrogen-bonding system in cellulose I_β from synchrotron X-ray and neutron fiber diffraction. Journal of the American Chemical Society, **124**, 9074–9082 (2002). DOI: 10.1021/ja0257319
[32] Jourdan C., Cavaille J. Y., Perez J.: Mechanical relaxations in polypropylene: A new experimental and theoretical approach. Journal of Polymer Science Part B: Polymer Physics, **27**, 2361–2384 (1989). DOI: 10.1002/polb.1989.090271115
[33] Davies G. R., Owen A. J., Ward I. M., Gupta V. B.: Interlamellar shear in anisotropic polyethylene sheets. Journal of Macromolecular Science Part B: Physics, **6**, 215–228 (1972). DOI: 10.1080/00222347208224798
[34] Di Liello V., Martuscelli E., Ragosta G., Zihlif A.: Effect of fibre surface treatment on yielding and fracture behaviour of glass fibre-polypropylene composite. Journal of Materials Science, **26**, 2100–2106 (1991). DOI: 10.1007/BF00549174
[35] Ségard E., Benmedakhene S., Laksimi A., Laï D.: Influence of the fibre/matrix interface on the behaviour until fracture of polypropylene reinforced with short glass fibres (in French). Mécanique et Industries, **6**, 479–486 (2005). DOI: 10.1051/meca:2005060
[36] Joseph P. V., Mathew G., Joseph K., Groeninckx G., Thomas S.: Dynamic mechanical properties of short sisal fibre reinforced polypropylene. Composites Part A: Applied Science and Manufacturing, **34**, 275–290 (2003). DOI: 10.1016/S1359-835X(02)00020-9
[37] Vaisburd D. I., Tverdokhlebov S., Tukhfatullin T. A.: Critical (burst) electron emission from dielectrics, induced by injection of a dense electron beam. Russian Physics Journal, **40**, 1064–1082 (1997). DOI: 10.1007/BF02508942

eXPRESS Polymer Letters Vol.4, No.3 (2010) 183–187
Available online at www.expresspolymlett.com
DOI: 10.3144/expresspolymlett.2010.23

Ferroferric oxide/polystyrene (Fe_3O_4/PS) superparamagnetic nanocomposite via facile *in situ* bulk radical polymerization

W. Zhong[1], *P. Liu*[1*], *H. G. Shi*[2], *D. S. Xue*[2]

[1]State Key Laboratory of Applied Organic Chemistry and Institute of Polymer Science and Engineering, College of Chemistry and Chemical Engineering, Lanzhou University, Gansu 730000, China
[2]Key Laboratory for Magnetism and Magnetic Materials of the Ministry of Education, Lanzhou University, Gansu 73000, China

Received 13 November 2009; accepted in revised form 17 January 2010

Abstract. Organo-modified ferroferric oxide superparamagnetic nanoparticles, synthesized by the coprecipitation of superparamagnetic nanoparticles in presence of oleic acid (OA), were incorporated in polystyrene (PS) by the facile *in situ* bulk radical polymerization by using 2,2-azobisisobutyronitrile (AIBN) as initiator. The transmission electron microscopy (TEM) analysis of the resultant uniform ferroferric oxide/polystyrene superparamagnetic nanocomposite (Fe_3O_4/PS) showed that the superparamagnetic nanoparticles had been dispersed homogeneously in the polymer matrix due to the surface grafted polystyrene, confirmed by Fourier transform infrared (FT-IR) spectroscopy and thermogravimetric analysis (TGA). The superparamagnetic property of the Fe_3O_4/PS nanocomposite was testified by the vibrating sample magnetometer (VSM) analysis. The strategy developed is expected to be applied for the large-scale industrial manufacturing of the superparamagnetic polymer nanocomposite.

Keywords: *nanocomposites, superparamagnetic, bulk polymerization, large-scale manufacturing*

1. Introduction

Polymer nanocomposites containing magnetic metal, alloy, or oxide nanoparticles have excellent potential for applications such as electromagnetic interference shielding, magneto-optical storage, biomedical sensing, flexible electronics, biomedicine, separations, etc. Control over the dispersion of the nanoparticle phase embedded in a polymer matrix is critical and often challenging. To achieve excellent dispersion, competition between polymer-polymer and polymer-particle interactions have to be balanced to avoid clustering of particles in polymer nanocomposites [1].

By far, there are two main approaches for the preparation of the polymer-based magnetic nanocomposites: physical mixing and *in situ* polymerization. In the first approach, the magnetic nanoparticles were physically mixed into polymeric matrices after being surface-modified with polymers [2–7]. The strategy is suitable for the large-scale industrial manufacturing, however, the uniform dispersion of the magnetic nanoparticles in the polymeric matrices could not be guaranteed [2]. As for the *in situ* polymerization approach via the solution polymerization [8, 9], dispersion polymerization [10, 11], and emulsion polymerization techniques [12–18], the magnetic nanoparticles are dispersed well in the polymeric matrices. But it is not suitable for the preparation of bulk magnetic nanocomposites because of its low efficiency.

*Corresponding author, e-mail: pliu@lzu.edu.cn

The bulk polymerization technique is desired to be the most suitable method for the large-scale industrial manufacturing except that, if the magnetic nanofillers are used in the form of small particles, the aggregation of the nanoparticles could be avoided. Most recently, Li *et al.* [19] prepared the bulk transparent PMMA/Fe-oxide nanocomposites via the bulk radical polymerization. In the present work, the ferroferric oxide/polystyrene superparamagnetic nanocomposite (Fe_3O_4/PS) was prepared via the facile bulk radical polymerization of styrene with the incorporation of the oleic acid modified ferroferric oxide superparamagnetic nanoparticles (OA-Fe_3O_4).

2. Experimetal

2.1. Materials

Ferric chloride hexahydrate ($FeCl_3 \cdot 6H_2O$), ferrous chloride tetrahydrate ($FeCl_2 \cdot 4H_2O$), ammonium hydroxide (NH_4OH, 25% of ammonia), and oleic acid (OA) were analytical grade reagents received from Tianjin Chemical Co. (Tianjin, China) and used without further purification and were used as received. The monomer, styrene (St, analytical reagent, Tianjin Chemicals Co. Ltd., China) was dried over CaH_2 and distilled under reduced pressure. The initiator, 2,2′-azobis(isobutylonitrile) (AIBN) (Tianjin Chemicals Ltd. Co. Tianjin, China) was re-crystallization in ethanol. Other reagents used were all analytical grade from Tianjin Chemicals Co. Ltd., China. Distilled water was used throughout.

2.2. OA-Fe_3O_4

The oleic acid modified ferroferric oxide superparamagnetic nanoparticles (OA-Fe_3O_4) were prepared according to our previous report [9]: 2.07 g $FeCl_3 \cdot 6H_2O$ and 0.81 g $FeCl_2 \cdot 4H_2O$ were dissolved into 100 ml water with stirring and bubbling with N_2. Then a mixture containing 10.0 ml ammonium hydroxide, 1.0 ml OA and 15 ml water was added dropwise to the solution after it was heated to 90°C. The reacting mixture was stirred for another 30 min after the addition. Finally, the products were collected by a magnet and rinsed with water three times and with ethanol once and dried in vacuum.

2.3. Bulk polymerization

The bulk polymerization was followed: 0.6 g OA-Fe_3O_4, 10 ml styrene, 0.15 g AIBN was added into a glass polymerization pipe, then the mixture was irradiated ultrasonically for 5 min and subsequently heated to 90°C and lasted for 8 h. After the temperature was cooled to room temperature, the polymerization pipe was broken open and the resulting superparamagnetic nanocomposite (Fe_3O_4/PS) was collected.

2.4. Analytical methods

A Bruker IFS 66 v/s infrared spectrometer was used for the Fourier transform infrared (FTIR) spectroscopy analysis. The morphologies of the superparamagnetic nanoparticles were characterized with a JEM-1200 EX/S transmission electron microscope (TEM).Thermogravimetric analysis (TGA) was performed with a Perkin-Elmer performed with a Perkin-Elmer TGA system from room temperature to 800°C in N_2 at a scan rate of 10°C min^{-1}. The magnetic properties were examined by vibrating sample magnetometer (VSM) (Lakeshore 7304).

3. Results and discussion

The properties of the inorganic nanoparticle/polymer composites definitively depend on the dispersibility of the inorganic nanoparticles in the polymer matrices. Surface modification of the inorganic nanoparticles with polymers has been validated to be the most impactful method to improve the dispersibility of the inorganic nanoparticles in the polymer matrices [20]. In the preparation of the magnetic nanocomposites via the *in situ* polymerization technique, oleic acid (OA) is the most used surface-modifier for the magnetic nanoparticles [21]. By modification with OA, the magnetic nanoparticles could be dispersed well in the monomers. Furthermore, the polymer grafted magnetic nanoparticles could be achieved by the copolymerization of the monomers and OA molecules immobilized on the surfaces of the magnetic nanoparticles. Therefore, the aggregation of the magnetic nanoparticles could be avoided and the uniform dispersion of the magnetic nanoparticles is obtained.

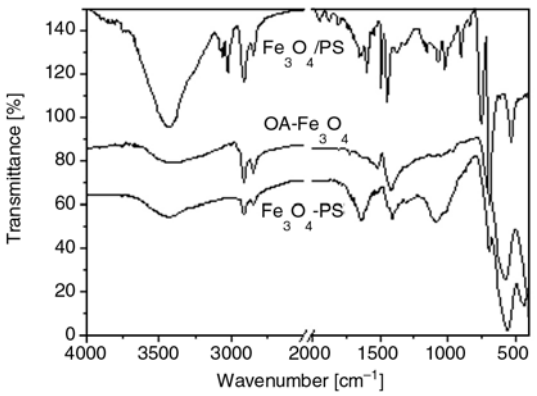

Figure 1. FT-IR spectra of the OA-Fe_3O_4 and Fe_3O_4-PS nanoparticles and Fe_3O_4/PS nanocomposite

The FT-IR spectrum reveals the nature of the bond that is formed between OA and the surface atoms. The antisymmetric and symmetric vibrations at 2920 and 2850 cm^{-1}, respectively, are clearly observed due to the aliphatic alkyl chains (Figure 1). The presence of two peaks at 1520 and 1425 cm^{-1}, attributed to the carboxylate unit vibration modes, shows that oleic acid is bound through the carboxylate anions, i.e. chemisorptions of the surfactant on the iron oxide surface. Except the chemisorbed amount, a physisorbed part was also present as evidenced by a less intense peak at 1721cm^{-1} (–COOH) because the miscibility of oleic acid with ethanol is low [22]. The TGA analysis (Figure 2) showed that the OA content of the OA-Fe_3O_4 nanoparticles were more than 20%.

In our previous work [9], the ferroferric oxide/polystyrene superparamagnetic nanocomposites (Fe_3O_4/PS) were prepared by the *in situ* solution polymerization of styrene in the present of the OA-Fe_3O_4 nanoparticles. It was found that the highest percent of grafting (PG%) had been achieved in the polymerization of 10.0 ml styrene with 0.60 g OA-Fe_3O_4 nanoparticles added in 10 ml toluene. So the ratio of the magnetic nanoparticles and monomer was applied in the present work.

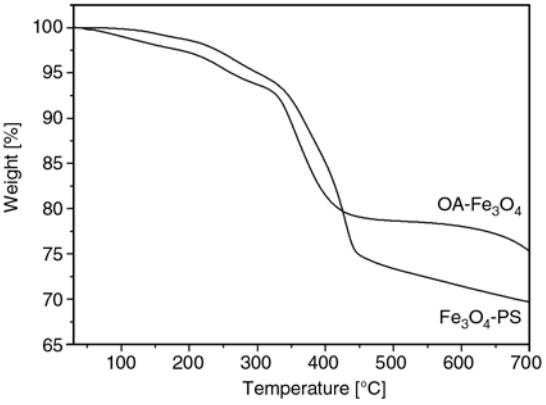

Figure 2. TGA curves of the OA-Fe_3O_4 and Fe_3O_4-PS nanoparticles

After the *in situ* bulk radical polymerization, the magnetic nanoparticles in the magnetic nanocomposite (Fe_3O_4/PS) were characterized with FT-IR and TGA techniques after being separated from the non-grafted PS by extracting the Fe_3O_4/PS with toluene, as reported previously [21]. Besides the same absorbance bands at 2920 and 2850 cm^{-1} of the CH_2 antisymmetric and symmetric vibrations, the characteristic absorption peaks at 580 cm^{-1} attributed to the lattice absorption of magnetite in the FT-IR spectra of the OA-Fe_3O_4 nanoparticles and the magnetic nanoparticles in the magnetic nanocomposite (Fe_3O_4/PS), the absorbance band at 699 cm^{-1} attributed to the phenyl structure, which is not present in the FT-IR spectrum of the OA-Fe_3O_4 nanoparticles, appeared (Figure 1). It indicated that the polystyrene had been successfully grafted onto the surfaces of the superparamagnetic nanoparticles via the *in situ* bulk polymerization. So the uniform grey-black superparamagnetic nanocomposite was achieved in the present work. Compared with the obvious macroscopic aggregations reported [23], the vital difference is the higher OA content in the OA-Fe_3O_4 nanoparticles.

The grafting percentage (GP%, mass ratio of the organic and inorganic components) of the polystyrene grafted magnetic nanoparticles (Fe_3O_4-PS) was calculated to be about 30% from the TGA analysis (Figure 2). The main weight loss of both OA-Fe_3O_4 and Fe_3O_4-PS occurred in the temperature range of 350–450°C, attributed to the thermal degradation of OA and PS modified on the surfaces of the magnetic nanoparticles.

Compared with the small aggregations of the oleic acid modified ferroferric oxide magnetic nanoparticles (OA-Fe_3O_4) in toluene as shown in Figure 3, most of the magnetic nanoparticles had been dispersed into toluene with diameter less than 10 nm in the polystyrene grafted magnetic nanoparticles (Fe_3O_4-PS). In fact, the magnetic nanoparticles tend to form the aggregations because of their magnetic forces although oleic acid molecules had been terminated on their surface. The aggregations seen in the OA-Fe_3O_4 nanoparticles were the clusters of OA-Fe_3O_4 nanoparticles, not the real aggregations of the magnetic nanoparticles. Their magnetic

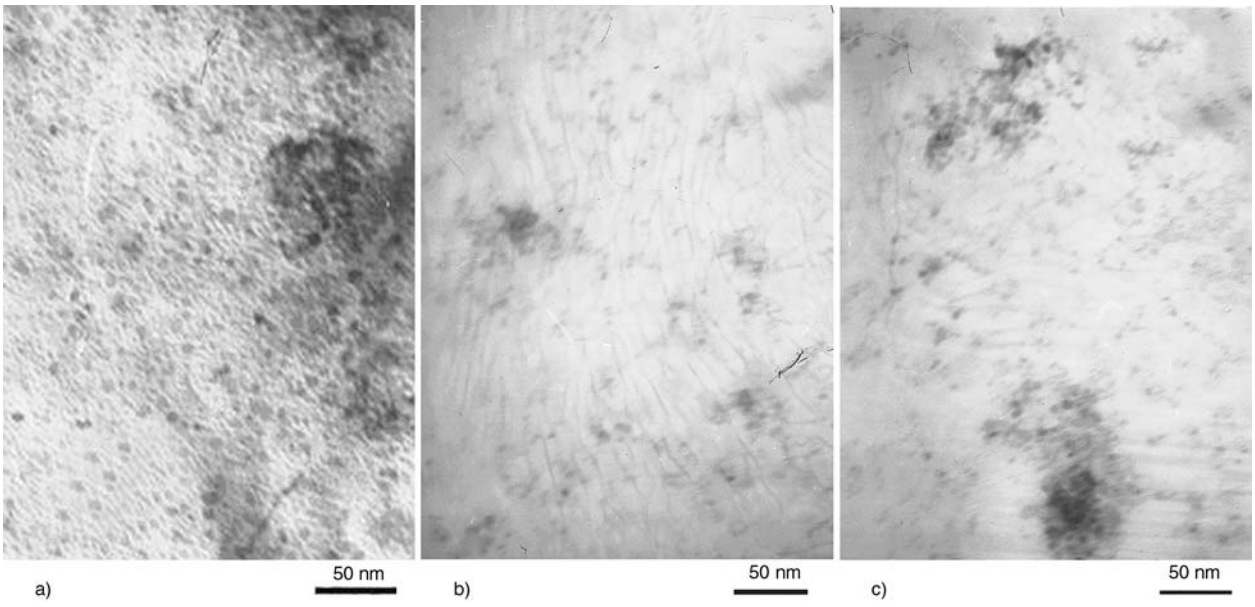

Figure 3. The TEM images of the OA-Fe_3O_4 (a), Fe_3O_4-PS (b) nanoparticles and PS/Fe_3O_4 nanocomposite (c)

forces could be conquered after the polystyrene macromolecules had been grafted. So they showed the better dispersibility in the organic solvent.

The hysteresis curves of the OA-Fe_3O_4 nanoparticles, Fe_3O_4-PS nanoparticles, and Fe_3O_4/PS nanocomposite were illustrated in Figure 4. Neither the remanence nor the coercivity was observed in the three hysteresis curves. They showed superparamagnetic with the saturation magnetization (M_s) values of 32, 40, and 2.2 emu/g at 25°C, respectively. It indicated that the polymerization did not affect magnetic properties of the nanoparticles. The saturation magnetization value of the Fe_3O_4-PS nanoparticles was higher than that of the OA-Fe_3O_4 nanoparticles because of the excellent dispersion of the magnetic nanoparticles. Furthermore, the saturation magnetization (M_s) value of the accidental sampling Fe_3O_4/PS nanocomposite was near to the theoretic value of about 2.3 emu/g. It indicated that the monomer conversion in the *in situ* radical bulk polymerization was near to 100% and the magnetic nanoparticles were dispersed uniformly in the polymer matrix. It is expected that the superparamagnetic polymer nanocomposite with different saturation magnetization values could be prepared with the strategy developed by simply changing the magnetic nanoparticles feeding ratio.

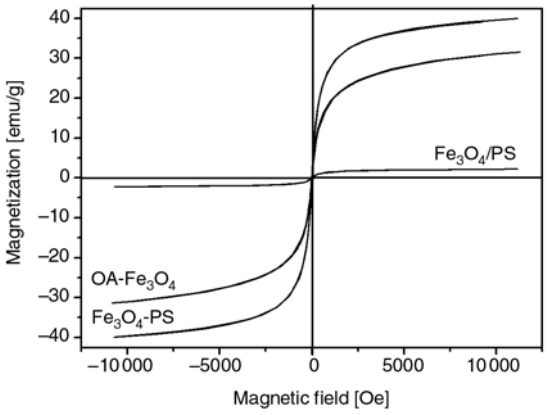

Figure 4. Magnetization curves of OA-Fe_3O_4, Fe_3O_4-PS and Fe_3O_4/PS

4. Conclusions

In summary, a facile *in situ* bulk radical polymerization strategy was developed for the preparation of the superparamagnetic nanocomposite (Fe_3O_4/PS). The polymerization did not affect magnetic properties of the nanoparticles. The strategy developed is expected to be applied for the large-scale industrial manufacturing of the superparamagnetic polymer nanocomposite due to the advantages such as simple manipulation and high efficiency.

References

[1] Pyun J.: Nanocomposite materials from functional polymers and magnetic colloids. Polymer Reviews, **47**, 231–263 (2007).
DOI: 10.1080/15583720701271294

[2] Xu C., Ohno K., Ladmiral V., Composto R. J.: Dispersion of polymer-grafted magnetic nanoparticles in homopolymers and block copolymers. Polymer, **49**, 3568–3577 (2008).
DOI: 10.1016/j.polymer.2008.05.040

[3] Garcia I., Tercjak A., Gutierrez J., Rueda L., Mondragon I.: Nanostructuration via solvent vapor exposure of poly(2-vinyl pyridine-*b*-methyl methacrylate) nanocomposites using modified magnetic nanoparticles. Journal of Physical Chemistry C, **112**, 14343–14347 (2008).
DOI: 10.1021/jp802345q

[4] Yáñez-Flores I. G., Betanvount-Galindo R., Aquino J. A. M., Rodríguez-Fernández O.: Preparation and characterization of magnetic PVC nanocomposites. Journal of Non-Crystalline Solids, **353**, 799–801 (2007).
DOI: 10.1016/j.jnoncrysol.2006.12.109

[5] Fang P. F., Chen Z., Zhang S. P., Wang S. J., Wang L. Y., Feng J. W.: Microstructure and thermal properties of ethylene-(vinyl acetate) copolymer/rectorite nanocomposites. Polymer International, **55**, 312–318 (2006).
DOI: 10.1002/pi.1957

[6] Yang T-I., Brown R. N. C., Kempel L. C., Kofinas P.: Magneto-dielectric properties of polymer-Fe_3O_4 nanocomposites. Journal of Magnetism and Magnetic Materials, **320**, 2714–2720 (2008).
DOI: 10.1016/j.jmmm.2008.06.008

[7] Hoppe C. E., Rivadulla F., López-Quintela M. A., Buján M. C., Rivas J., Esrantes D., Baldomir D.: Effect of submicrometer clustering on the magnetic properties of free-standing superparamagnetic nanocomposites. Journal of Physical Chemistry C, **112**, 13099–13104 (2008).
DOI: 10.1021/jp8039548

[8] Dallas P., Georgakilas V., Dimitrios N., Komninou P., Kehagias T., Petridis D.: Synthesis, characterization and thermal properties of polymer/magnetite nanocomposites. Nanotechnology, **17**, 2046–2053 (2006).
DOI: 10.1088/0957-4484/17/8/043

[9] Liu P., Zhong W., Shi H. G., Xue D. S.: Polymer grafted magnetite nanoparticles via a facile in-situ solution radical polymerization. Journal of Experimental Nanoscience, **4**, 323–329 (2009).
DOI: 10.1080/17458080903108150

[10] Gyergyek S., Huskic M., Makovec D., Drofenik M.: Superparamagnetic nanocomposites of iron oxide in a polymethyl methacrylate matrix synthesized by in situ polymerization. Colloids and Surfaces A: Physicochemical and Engineering Aspects, **317**, 49–55 (2008).
DOI: 10.1016/j.colsurfa.2007.09.035

[11] Fan L-H., Luo Y-L., Chen Y-S., Zhang C-H., Wei Q-B.: Preparation and characterization of Fe_3O_4 magnetic composite microspheres covered by a P(MAH-co-MAA) copolymer. Journal of Nanoparticle Research, **11**, 449–458 (2009).
DOI: 10.1007/s11051-008-9556-z

[12] Qiu G. H., Wang Q., Wang C., Lau W., Guo Y. L.: Polystyrene/Fe_3O_4 magnetic emulsion and nanocomposite prepared by ultrasonically initiated miniemulsion polymerization. Ultrasonics Sonochemistry, **14**, 55–61 (2007).
DOI: 10.1016/j.ultsonch.2006.03.001

[13] Jiang J.: Ultrasonic-assisted synthesis of PMMA/$Ni_{0.5}Zn_{0.5}Fe_2O_4$ nanocomposite in mixed surfactant system. European Polymer Journal, **43**, 1724–1728 (2007).
DOI: 10.1016/j.eurpolymj.2007.02.011

[14] Martins M. A., Neves M. C., Esteves A. C. C., Girginova P. I., Guiomar A. J., Amaral V. S., Trindade T.: Biofunctionalized ferromagnetic $CoPt_3$/polymer nanocomposites. Nanotechnology, **18**, 215609 (2007).
DOI: 10.1088/0957-4484/18/21/215609

[15] Mahdavian A. R., Ashijari M., Mobarakeh H. S.: Nanocomposite particles with core-shell morphology. I. Preparation and characterization of Fe_3O_4-poly(butyl acrylate-styrene) particles via miniemulsion polymerization. Journal of Applied Polymer Science, **110**, 1242–1249 (2008).
DOI: 10.1002/app.28729

[16] Liu H., Xu F., Li L. C., Wang Y. P., Qiu H. Z.: A novel $CoFe_2O_4$/polyacrylate nanocomposite prepared via an *in situ* polymerization in emulsion system. Reactive and Functional Polymers, **69**, 43–47 (2009).
DOI: 10.1016/j.reactfunctpolym.2008.10.009

[17] Yang S., Liu H. R., Huang H. F., Zhang Z. C.: Fabrication of superparamagnetic magnetite/poly(styrene-*co*-12-acryloxy-9-octadecenoic acid) nanocomposite microspheres with controllable structure. Journal of Colloid and Interface Science, **338**, 584–590 (2009).
DOI: 10.1016/j.jcis.2009.07.007

[18] Zhang X. J., Jiang W., Li F. S., Sun Z. D., Ou'yang Z.: Controllable preparation of magnetic polymer nanospheres with high saturation magnetization by miniemulsion polymerization. Materials Letters, **64**, 119–121 (2010).
DOI: 10.1016/j.matlet.2009.10.002

[19] Li S. H., Qin J., Formara A., Toprak M., Muhammed M., Kim D. K.: Synthesis and magnetic properties of bulk transparent PMMA/Fe-oxide nanocomposites. Nanotechnology, **20**, 185607 (2009).
DOI: 10.1088/0957-4484/20/18/185607

[20] Liu P., Su Z. X.: Thermal stabilities of polystyrene/silica hybrid nanocomposites via microwave-assisted in-situ polymerization. Materials Chemistry and Physics, **94**, 412–416 (2005).
DOI: 10.1016/j.matchemphys.2005.05.023

[21] Wu W., He Q., Jiang C.: Magnetic iron oxide nanoparticles: Synthesis and surface functionalization strategies. Nanoscale Research Letters, **3**, 397–415 (2008).
DOI: 10.1007/s11671-008-9174-9

[22] Liu G., Liu P.: Synthesis of monodispersed crosslinked nanoparticles decorated with surface carboxyl groups via soapless emulsion polymerization. Colloids and Surfaces A: Physicochemical and Engineering Aspects, **354**, 377–381 (2010).
DOI: 10.1016/j.colsurfa.2009.05.016

[23] Xia A., Hu J., Wang C., Jiang D.: Synthesis of magnetic microspheres with controllable structure via polymerization-triggered self-positioning of nanocrystals. Small, **3**, 1811–1817 (2007).

eXPRESS Polymer Letters Vol.4, No.3 (2010) 188–195
Available online at www.expresspolymlett.com
DOI: 10.3144/expresspolymlett.2010.24

A novel polymer of $Al_2(SO_4)_3$-poly(acrylamide-co-2-acrylamido-2-methyl-1-propanesulfonate) ionic hybrid prepared by dispersion polymerization

Y. M. Wu, W. P, Zhao, J. Xu, C. X. Wang*

College of Chemical Engineering, Qingdao University of Science & Technology, Qingdao 266042, P. R. China

Received 17 November 2009; accepted in revised form 23 January 2010

Abstract. A novel polymer $Al_2(SO_4)_3$-poly(acrylamide-co-2-acrylamido-2-methyl-1-propanesulfonate) ($Al_2(SO_4)_3$-P(AM/AMPS)) had been synthesized by dispersion polymerization in an aqueous solution of ammonium sulfate and aluminum sulfate, using poly(2-acrylamido-2-methyl-1-propanesulfonate) P(AMPS) as stabilizer, acrylamide (AM) and 2-acrylamido-2-methyl-1-propanesulfonate (AMPS) as monomers, poly(2-acrylamido-2-methyl-1-propanesulfonate) (PAMPS) as stabilizer and [2-(2-imidazdino-2-yl)propane]dihydrochloride (VA-044) as initiator. The average particle size of polymer dispersion ranged from 0.2 to 0.3 μm, the molecular weight was from $4.3 \cdot 10^6$ to $5.7 \cdot 10^6$ g·mol^{-1}. The polymer was characterized by infrared (IR) spectroscopy, thermogravimetry (TGA) and transmission electron microscopy (TEM). The swelling property of the dispersion polymer was studied by particle size distribution. When the polymer dispersion was diluted with deionized water, particle sizes decreased several times. When the polymer dispersion was diluted with salt water, the particle size increased with increasing concentration of salt. The effects of $Al_2(SO_4)_3$ and stabilizer on the particle size and the relative molecular weight of the polymer were investigated, respectively. The optimum conditions for the stable $Al_2(SO_4)_3$-P(AM/AMPS) dispersion were that the concentration of $Al_2(SO_4)_3$ was 1.12 wt%, the concentration of PAMPS stabilizer was 3 wt% and the concentration of initiator was 0.2 mol·l^{-1} and the monomers concentration was 14 wt%.

Keywords: *smart polymers, dispersion polymerization, polyacrylamide, organic-inorganic hybrids, aluminum sulfate*

1. Introduction

As attractive materials, organic-inorganic hybrids that could have high performance or high function due to synergism of two components have been widely used, such as photochromic films, optical functionalities, flocculants and process aids for low-grade oil sand ore [1–4]. Several methods have been used to prepare organic-inorganic hybrids such as sol-gel reaction [5, 6], intercalation polymerization [7, 8], melt-processing [9, 10], and *in situ* polymerization [11, 12].

The first condition for preparation of organic-inorganic hybrids with enhanced performance is to guarantee uniform distribution of inorganic particles within the polymer matrix. Dispersion polymerization has been considered as a promising and preponderant approach in preparing nearly monodisperse polymer particles in a single step [13]. In dispersion polymerization, the organic polymer can be uniformly dispersed in the form of particles whose size ranged from 0.1–15 μm, which can ensure the inorganic particles uniformly dispersed as much as possible in the system.

To our knowledge, little research has been reported on inorganic/polyacrylamide hybrids. Feng *et al.* [1] prepared photochromic nanocomposite thin films by entrapping polyoxometalate in a polyacrylamide matrix via the ultrasound technique. Mat-

*Corresponding author, e-mail: wuyumin001@126.com

suura *et al.* [2] had synthesized polysilane-acrylamide block copolymers by photopolymerization of acrylamide monomers. Yang *et al.* [3] had synthesized $Al(OH)_3$-polyacrylamide using a redox initiation in aqueous medium. However, there existed little works about the hybrid $Al_2(SO_4)_3$-poly(acrylamide-co-2-acrylamido-2-methyl-1-propanesulfonate) ($Al_2(SO_4)_3$-poly(AM/AMPS)) by dispersion polymerization in aqueous medium.

In this work, a novel dispersion polymer $Al_2(SO_4)_3$-poly(AM/AMPS) ionic hybrid was synthesized by using 2,2'-azobis(2-(2-imidazolin-2-yl) propane) dihidrochloride (VA-044) as an initiator and poly(2-acrylamido-2-methyl-1-propanesulfonate) (PAMPS) as the stabilizer through dispersion polymerization and ionic bond between $Al_2(SO_4)_3$ and poly(AM/AMPS) was characterized by thermogravimetric analysis and IR spectroscopy. Compared with the nonionic stabilizer used in other works, the negative charged end groups in the polymer chains of PAMPS were anticipated to enhance the stability of the lattices by electrostatic repulsion as well as to interact with $Al_2(SO_4)_3$ with positive charge. The effects of concentration of $Al_2(SO_4)_3$, the stabilizer and initiator on molecular weight, particle size distribution and the overall conversion of the monomers were investigated, and the swelling property of the dispersion polymer was discussed. The difference between P(AM/AMPS) and $Al_2(SO_4)_3$-poly(AM/AMPS) was discussed in terms of the stabilizer concentration and particle size distribution.

2. Experimentals

2.1. Materials

Acrylamide (AM) and 2-acrylamido-2-methyl-1-propane sulfonate (AMPS) were industrial materials purchased from Dia-Nitrix Co. Ltd. (Japan) and Zhenxing Fine Chemicals Inc. Henan (China), respectively. Aluminium sulfate ($Al_2(SO_4)_3$) and ammonium sulfate ($(NH_4)_2SO_4$) were analytical grade. Deionized water was used throughout the experiments. 2,2′-azobis(2-(2-imidazolin-2-yl) propane) dihidrochloride (VA-044, A. R. Grade) was purchased from WAKO Pure Chemical Industries Ltd. (Japan). Poly(2-acrylamido-2-methyl-1-propanesulfonate) (PAMPS) was prepared from AMPS in an aqueous solution using VA-044 as initiator at 40°C under nitrogen atmosphere for 4–5 h. The molecular weight of PAMPS was $3.0 \cdot 10^5$–$7.0 \cdot 10^5$ g·mol^{-1}. In this work we used PAMPS whose molecular weight was around $3.5 \cdot 10^5$ g·mol^{-1}.

2.2. Preparation of polymer dispersion

Varying quantities of the ingredients containing monomers, aluminium sulfate, ammonium sulfate, PAMPS and deionized water were added to a 250 ml four-neck flask fitted with a stirrer, a reflux condenser, a thermometer and a nitrogen inlet tube. After purging with nitrogen for 30 min and controlling the temperature at 60°C by means of an external heating jacket, the monomers were initiated by drop-feeding VA-044 aqueous solution into the reactor evenly over a period of 1 h. After reacting 6 h, heating stopped and the $Al_2(SO_4)_3$-P(AM/AMPS) hybrids were obtained. The stirring speed was fixed at 120 rpm in all experiments.

2.3. Characterization of dispersion copolymer

$Al_2(SO_4)_3$-P(AM/AMPS) dispersion was dissolved in water. Then, the polymer was washed with acetone. These operations were repeated several times to remove the inorganic salts, unreacted monomers and PAMPS. Then the copolymer precipitated was dried to a constant weight at 50°C under vacuum. The dried sample was used to determine the intrinsic viscosity [η] of the copolymer was determined in a 1 mol/l NaCl aqueous solution with an Ubbelohde capillary viscometer at 30°C. The concentration used for the measurement of viscosity was 0.0005–0.001 g/ml. The viscosity-average molecular weight M_v could be calculated with the Mark-Houwink relationship (Equation (1)):

$$M_v = \left(1000 \cdot \frac{[\eta]}{3.73}\right)^{1/0.66} \quad (1)$$

The method to determine PAMPS molecular weight was the same as in the case of $Al_2(SO_4)_3$-P(AM/AMPS).

Particle size and particle size distribution were measured with Coulter LS230 particle size analyzer. The samples were usually dispersed by ultrasonic agitation before measurements.

FT-IR spectra were recorded on a spectrophotometer (AVATAR 360, Nicolet, USA) using KBr pellets. The thermal degradation test was conducted on

TGA (TG209, NETZSCH, Germany) at a heating rate of 10°C/min under static N_2 atmosphere. Weigh 5 mg $Al_2(SO_4)_3$ and 5 mg P(AM/AMPS) and then mix them together. All samples (10.0 mg) used had been dried in vacuum at 110–120°C for 8 h. The change in weight differential difference with temperature was recorded. The particle morphology of $Al_2(SO_4)_3$-P(AM/AMPS) and P(AM/AMPS) were measured by TEM (JEM-1200EX, JEOL, Japan).

The total monomer conversion could be obtained by determining residual contents of AM and AMPS with bromating method [14].

3. Results and discussion

3.1. Effect of $Al_2(SO_4)_3$ concentrations

Effect of $Al_2(SO_4)_3$ concentration on the relative molecular weight, particles size and conversion of monomers were shown in Table 1. As shown in Table 1, with increasing concentration of $Al_2(SO_4)_3$, molecular weight increased, but the particle size and the particle size distribution decreased. When $Al_2(SO_4)_3$ concentration was between 0 and 1.86 wt%, stable dispersion could be obtained. $Al_2(SO_4)_3$ and $(NH_4)_2SO_4$ can form a complex salt called $AlNH_4(SO_4)_2{\cdot}12H_2O$ whose solubility in water is much lower than any of them. So, in our experiments, the concentration of $Al_2(SO_4)_3$ in aqueous $(NH_4)_2SO_4$ solution is less than 1.86% to avoid precipitation. But the reaction temperature between $Al_2(SO_4)_3$ and $(NH_4)_2SO_4$ was 100°C, in our experiment the temperature was around 60°C. So there was little $AlNH_4(SO_4)_2$ in the system. Compared with $Al_2(SO_4)_3$ concentration, the $AlNH_4(SO_4)_2$ could be ignored. According to Electric Double Layer Theory, the thickness of diffusion electrical double layer reduced with adding Al^{3+} into the reaction system. As a result, the molecular chain of polymer crimples seriously, at the same time, and the number of mature particles does not change [15], so the particle sizes decreased. Moreover, $Al_2(SO_4)_3$ also has the precipiation effect. The precipitation effect became stronger with increasing $Al_2(SO_4)_3$ concentration, so the particles size decreased with $Al_2(SO_4)_3$.

3.2. Effect of stabilizer concentrations

A series of experiments were carried out to examine the effect of stabilizer concentrations on the hybrid. As shown in Table 2, when PAMPS content was less than 1.5%, it could not provide enough electrostatic repulsion and steric stabilization and an agglomerating system was obtained. With increasing PAMPS, the relative molecular weight

Table 1. Effect of salt concentration on the properties of dispersion polymers

$Al_2(SO_4)_3$ [wt%]	M_w [10^6 g·mol^{-1}]	Conversion [%]	P.D. [μm]	Notes
0.00	4.33	93.3	0.30(0.10–0.7)	
0.37	4.42	93.5	0.27(0.07–0.7)	
0.75	4.57	93.2	0.25(0.07–0.6)	
1.12	4.76	93.4	0.23(0.07–0.8)	
1.49	5.12	93.2	0.21(0.07–0.6)	
1.86	5.22	92.1	0.20(0.07–0.7)	
1.93	–	–	–	precipitated

Polymerization conditions: AM/AMPS (mole ratio), 5/1; total monomer 14%; PAMPS 1.8%; VA-044 0.01 wt%; $(NH_4)_2SO_4$ 25%. P.D., average of particle diameter (range of particle diameter).

Table 2. Effect of stabilizer concentrations on dispersion polymer

PAMPS [wt%]	M_w [10^6 g·mol^{-1}]	Conversion [%]	P.D. [μm]
1.5	coagulated	–	–
2.0	4.12	89.1	0.27(0.07–0.7)
3.0	4.76	93.6	0.26(0.07–0.7)
4.0	4.36	92.3	0.24(0.07–0.6)
5.0	4.62	90.3	0.23(0.07–0.6)
6.0	4.83	89.4	0.22(0.07–0.6)
8.0	5.74	88.4	0.20(0.07–0.6)

Polymerization conditions: AM/AMPS (mol ratios) 5/1; total monomer, 14%; $(NH_4)_2SO_4$ 25%; $Al_2(SO_4)_3$ 1.12%; and VA-044, 0.01 wt%

had a slowly increasing tendency, but the particle sizes decreased.

Compared with the system without adding $Al_2(SO_4)_3$ in the syntheses media, obviously different results were found. We have reported [14] that when PAMPS concentration was below 1.2 or above 3.0%, the copolymer dispersion would coagulate. Suitable PAMPS concentration was from 1.8 to 2.7%. In this system, even if PAMPS concentration was up to 8%, the system was still stable. It could be attributed to $Al_2(SO_4)_3$ colloid with positive charge interacting with the with negatively charged stabilizer filling. There was an obvious tendency that the particle sizes decreased and the molecular weight increased as the stabilizer concentration increased. It was different from the results of Cho *et al.* [15] and Chen *et. al.* [16] but in correspondence with the results of dispersion polymerization Ray and Mandal's [17, 18] reported in the literature. The particle size decreased with increasing stabilizer concentration. The increasing of molecular weight was the contribution of the solid phase polymerization increase associated with the gel effect. As for a given quantity of polymer smaller particles present greater surface area, so the particle phase captures oligomeric radical from the continuous will increase, and the molecular weight of the polymer would increase. Furthermore, PAMPS used as stabilizer was incorporated in the final dispersion copolymer and may influence the final molecular weight. The influence maybe very small because the molecular weight of the PAMPS was too low compared with the dispersion copolymer.

As shown in Table 2, the overall conversions decreased with PAMPS concentration increasing. Since with increasing PAMPS, the viscosity of the continuous phase increased correspondingly, which prevented monomer radicals freely transferred between nature particles and continuous phase. So, the overall conversion was reduced.

3.3. Effect of initiator concentrations

Experimental sets in Table 3 showed the effects of initiator concentration from 1.0 to 4.5 $mol \cdot l^{-1}$, whereas the monomer, stabilizer, $(NH_4)_2SO_4$, and $Al_2(SO_4)_3$ concentrations were fixed at 14, 3, 25, and 1.12%, respectively. As shown in Table 3, the relative molecular weight decreased with increasing VA-044. While the rate of polymerization increases with increase of initiator concentration, the average numbers of monomer molecules consumed per each radical become smaller, resulting in the lower molecular weight [19].

It also could be seen that particle size increased with increasing the initiator concentration which was commonly observed in dispersion polymerization. The most commonly offered explanation was that a higher initiator concentration would lead to a greater rate of generation of unstable oligoradicals or dead polymer molecules. These primary particles are not stabilized enough by the stabilizers, resulting in a greater rate of coagulation, yielding lager size particles [14].

3.4. Particle size of dispersion polymers

As shown in Figure 1, the average particle size of the original dispersion ranged from 0.03 to 0.8 μm, while those diluted with different salt water and deionized water were in the range of 0.01–0.1, 1.3–2.7 and 0.007–0.05 μm, respectively. The results were contrary to some works reported. We have reported that when diluted with deionized water the particle size became large [15]. It was explained that the insufficient salt concentration weakening the electrostatic repulsion between particles led to expanded molecular chains, and the particle size became larger.

Chen *et al.* [16] said that oligomeric radicals and monomers could enter the particles through solvent channel. It also could be understood as the inorganic salt could enter the particles. Through

Table 3. Effect of initiator concentrations on dispersion polymer

VA-044 [10^{-4} mol·l^{-1}]	M_w [10^6 g·mol^{-1}]	Conversion [%]	P.D. [μm]
1.0	4.76	93.6	0.26(0.07–0.7)
2.0	4.59	94.2	0.27(0.07–0.7)
3.0	4.44	94.9	0.29(0.1–0.8)
4.0	4.21	95.3	0.31(0.1–0.9)
4.5	4.05	95.7	0.35(0.1-0.9)

Polymerization conditions: AM/AMPS (mol ratios) 5/1; total monomer, 14%; $(NH_4)_2SO_4$ 25%; $Al_2(SO_4)_3$ 1.12%, PAMPS 1.8%

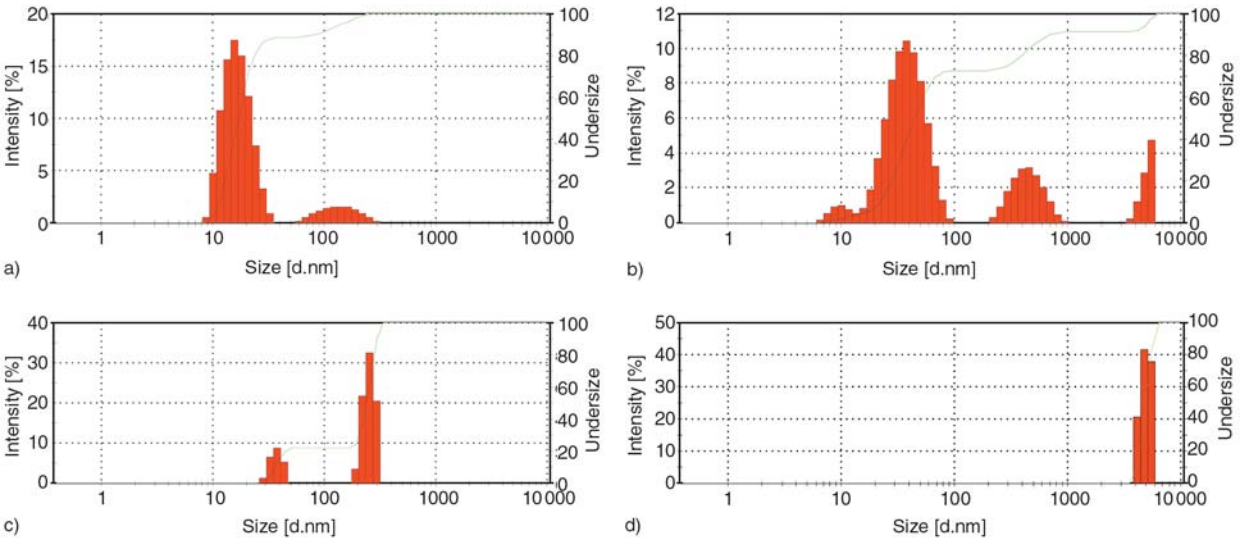

Figure 1. Particle size distribution of different solutions: (a) solution diluted with deionzed water, (b) solution diluted with 15% $(NH_4)_2SO_4$ solution, (c) solution diluted with original solution, and (d) solution diluted with 30% $(NH_4)_2SO_4$ solution

Brownian diffusion the concentration of inorganic salt inside the particles and outside the particles must be consistent. When diluted with the lower concentration of salt water, the inorganic salt could diffuse from the particle to the continuous phase, so the particle size decreased. Similarly, when diluted with high concentration of salt water, the inorganic salt diffused from continuous phase to the particles, so the particle size increased.

3.5. Characteristics of $Al_2(SO_4)_3$-P(AM/AMPS)

Figure 2 represented the FT-IR spectra of $Al_2(SO_4)_3$-P(AM/AMPS) and P(AM/AMPS), respectively. Curves 'b' displayed almost the same characteristic bands as curves 'a' except for the nuances of 940 and 713 cm^{-1}. $Al_2(SO_4)_3$ has absorbance at 940 and 713 cm^{-1}, assigned to $\upsilon_{Al\text{-}SO_3}$ and $\upsilon_{Al\text{-}O}$, respectively. It indicated that the sample was an organic-inorganic hybrid of $Al_2(SO_4)_3$-P(AM/AMPS).

Figure 3 showed the TGA curves of $Al_2(SO_4)_3$-P(AM/AMPS), $Al_2(SO_4)_3$/P(AM/AMPS) mixture and P(AM/AMPS). As shown in Figure 3, $Al_2(SO_4)_3$-P(AM/AMPS) hybrid had two peaks of pyrolysis rate (T_p) at 280 and 739°C, respectively, while $Al_2(SO_4)_3$/P(AM/AMPS) mixture and the pure P(AM/AMPS) had peaks at 269, 654.5 and 225, 598.1°C, respectively. Activation energies (E_a) of these samples could be evaluated from TGA data according to Flynn and Wall method [20]. The results of T_p and E_a are shown in Table 4. Accord-

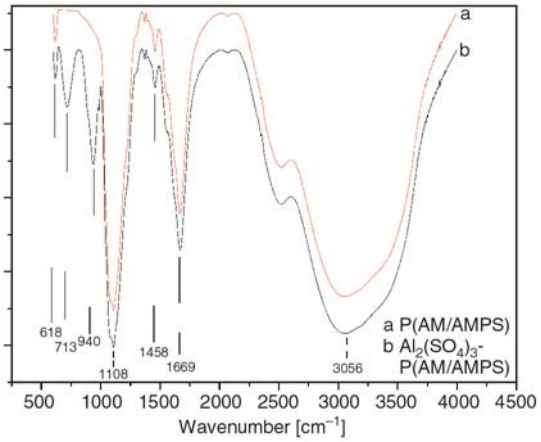

Figure 2. IR spectra of $Al_2(SO_4)_3$-P(AM/AMPS) and P(AM/AMPS)

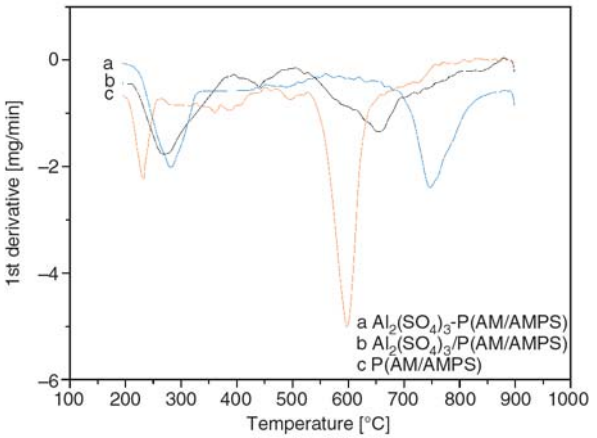

Figure 3. Different TGA curves of $Al_2(SO_4)_3$-P(AM/AMPS), $Al_2(SO_4)_3$/P(AM/AMPS) mixture and P(AM/AMPS)

Table 4. T_p and E_a of $Al_2(SO_4)_3$-P(AM/AMPS), $Al_2(SO_4)_3$/P(AM/AMPS) mixture, and P(AM/AMPS)

Samples	T_p [°C]		E_a [KJ/mol]	
	First stage	Second stage	First stage	Second stage
$Al_2(SO_4)_3$-P(AM/AMPS)	280	739.5	176.1	292.3
$Al_2(SO_4)_3$/P(AM/AMPS)	269	654.5	152.2	273.9
P(AM/AMPS)	225	598.1	141.8	246.3

ing to the results from Yang and coworkers [3, 21], high T_p and large E_a of the $Al_2(SO_4)_3$-P(AM/AMPS) were also attributed to the ionic bond formed between $Al_2(SO_4)_3$ and P(AM/AMPS) chains.

When researching the interaction between colloidal particles and polyelectrolyte with opposite charge, Hou *et al.* [22] found that the presence of these colloidal particles increased the degree of ionization of the polyelectrolyte. According to this, heat resistance of the $Al_2(SO_4)_3$-P(AM/AMPS) and FTIR spectra indicated that the negative end group of P(AM/AMPS) chain could form an ionic bond with $Al_2(SO_4)_3$ with positive charge.

Figure 4 showed the TEM micrograph of $Al_2(SO_4)_3$-P(AM/AMPS) and P(AM/AMPS). Compared with Figure 4a and 4b significant differences were shown. Figure 4a had a bright rim structure around the surface of the particles but Figure 4b did not have such structure. The very different between the two samples was that one with $Al_2(SO_4)_3$ in it, the other was not. So, we indicate that the $Al_2(SO_4)_3$ particles were present outside of the particles.

4. Conclusions

The main conclusions from this work are as follows:

(1) $Al_2(SO_4)_3$-poly(AM/AMPS) ionic hybrid was synthesized by dispersion polymerization in an aqueous solution of $Al_2(SO_4)_3$ and $(NH_4)_2SO_4$ in the presence of PAMPS as stabilizer. Ionic bonds between $Al_2(SO_4)_3$ and poly(AM/AMPS) chains in $Al_2(SO_4)_3$-P(AM/AMPS) are displayed.

(2) The optimum conditions for obtaining stable dispersion polymer of $Al_2(SO_4)_3$-P(AM/AMPS) were as follows: the concentration of $Al_2(SO_4)_3$ was 1.12%, the concentration of the PAMPS stabilizer was 3%, and the concentration of initiator was 0.2 mol·l^{-1}, respectively. With increasing the concentration of $Al_2(SO_4)_3$, the molecular weight increased but the particle sizes decreased, respectively. With increasing the concentration of the stabilizer, the particle sizes decreased and the molecular weight increased.

(3) The swelling property of the dispersion polymer was studied by particle size distribution.

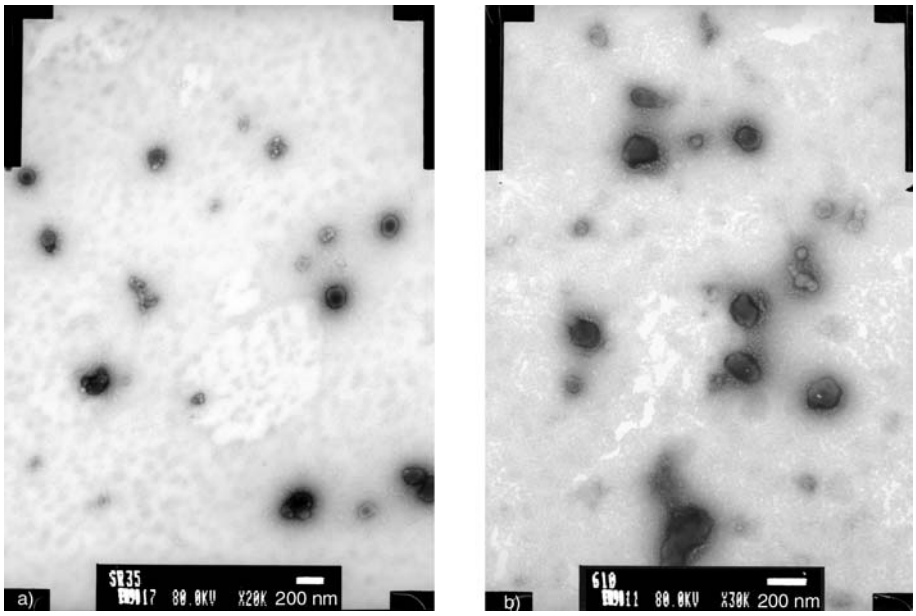

Figure 4. TEM micrograph of $Al_2(SO_4)_3$-P(AM/AMPS) and P(AM/AMPS): (a) $Al_2(SO_4)_3$-P(AM/AMPS) content $Al_2(SO_4)_3$ 1.12 wt%; (b) P(AM/AMPS)

When diluted with different concentrations of $(NH_4)_2SO_4$ solutions the particle size increased with the $(NH_4)_2SO_4$ concentration increased, and when diluted with deionzed water the particle size minimized.

Acknowledgements

Authors gratefully acknowledge the financial support by National Science Foundation of China (20876081) and Projects under Scientific and Technological Planning of Shandong Province (J08LC04).

References

[1] Feng W., Zhang T. R., Wei L., Lu R., Bai Y. B., Li T. J., Zhao Y. Y., Yao J. N.: Photochromic behavior and mechanism of thin films in $H_3PW_{12}O_{40}$/polyacrylamide system. Materials Letters, **54**, 309–313 (2002). DOI: 10.1016/S0167-577X(01)00583-3

[2] Matsuura Y., Matsukawa K., Kawabata R., Higashi N., Niwa M., Inoue H.: Synthesis of polysilane-acrylamide copolymers by photopolymerization and their application to polysilane-silica hybrid thin films. Polymer, **43**, 1549–1553 (2002). DOI: 10.1016/S0032-3861(01)00693-0

[3] Yang W. Y., Qian J. W., Shen Z. Q.: A novel flocculant of $Al(OH)_3$-polyacrylamide ionic hybrid. Journal of Colloid and Interface Science, **273**, 400–405 (2004). DOI: 10.1016/j.jcis.2004.02.002

[4] Li H. H., Long J., Xu Z. H., Masliyah J. H.: Novel polymer aids for low-grade oil sand ore processing. The Canadian Journal of Chemical Engineering, **86**, 168–176 (2008). DOI: 10.1002/cjce.20030

[5] Huang H-H., Wilkes G. L., Carlson J. G.: Structure-property behavior of new hybrid materials incorporating oligomeric poly(tetramethylene oxide) with inorganic silicates by a sol-gel process. Polymer Bulletin, **18**, 455–462 (1987). DOI: 10.1016/0032-3861(89)90286-3

[6] Noell J. L. W., Wilkes G. L., Mohanty D. K., McGrath J. E.: The preparation and characterization of new polyether ketone-tetraethylorthosilicate hybrid glasses by the sol-gel method. Journal of Applied Polymer Science, **40**, 1177–1194 (1990). DOI: 10.1002/app.1990.070400709

[7] LeBaron P. C., Wang Z., Pinnavia T.: Polymer-layered silicate nanocomposites: An overview. Applied Clay Science, **15**, 11–29 (1999). DOI: 10.1016/S0169-1317(99)00017-4

[8] Messersmith P. B., Giannelis E. P.: Synthesis and barrier properties of poly(ε-caprolactone)-layered silicate nanocomposites. Journal of Polymer Science Part A: Polymer Chemistry, **33**, 1047–1057 (1995). DOI: 10.1002/pola.1995.080330707

[9] Vaia R. A., Jandt K. D., Kramer E. J., Giannelis E. P.: Kinetics of polymer melt intercalation. Macromolecules, **28**, 8080–8085 (1995). DOI: 10.1021/ma00128a016

[10] Vaia R. A., Ishii H., Giannelis E. P.: Synthesis and properties of two-dimensional nanostructures by direct intercalation of polymer melts in layered silicates. Chemistry of Materials, **5**, 1694–1696 (1995). DOI: 10.1021/cm00036a004

[11] Wu W., He T. B., Chen J-F., Zhang X., Chen Y.: Study on in situ preparation of nano calcium carbonate/PMMA composite particles. Materials Letters, **60**, 2410–2415 (2006). DOI: 10.1016/j.matlet.2005.03.077

[12] Du Z., Zhang W., Zhang C., Jing Z., Li H.: A novel polyethylene/palygorskite nanocomposite prepared via in-situ coordinated polymerization. Polymer Bulletin, **49**, 151–158 (2002). DOI: 10.1007/s00289-002-0086-z

[13] Hasegawa H., Arai K., Saito S.: Uniform encapsulation of fine inorganic powder with soapless emulsion polymerization. Journal of Polymer Science Part A: Polymer Chemistry, **25**, 3117–3125 (1987). DOI: 10.1002/pola.1987.080251115

[14] Wu Y. M., Wang Y. P., Yu Y. Q., Xu J., Chen Q. F.: Dispersion polymerization of acrylamide with 2-acrylamido-2-methyl-1-propane sulfonate in aqueous solution. Journal of Applied Polymer Science, **102**, 2379–2385 (2006). DOI: 10.1002/app.24494

[15] Cho M. S., Yoon K. J., Song B. K.: Dispersion polymerization of acrylamide in aqueous solution of ammonium sulfate: Synthesis and characterization. Journal of Applied Polymer Science, **83**, 1397–1450 (2002). DOI: 10.1002/app.2300

[16] Chen D., Liu X., Yue Y., Zhang W., Wang P.: Dispersion copolymerization of acrylamide with quaternary ammonium cationic monomer in aqueous salts solution. European Polymer Journal, **42**, 1284–1297 (2006). DOI: 10.1016/j.eurpolymj.2005.12.007

[17] Ray B., Mandal B. M.: Dispersion polymerization of acrylamide. Langmuir, **13**, 2191–2196 (1997). DOI: 10.1021/la9605044

[18] Ray B., Mandal B. M.: Dispersion polymerization of acrylamide: Part II. 2,2′-azobisisobutyronitrile initiator. Journal of Polymer Science Part A: Polymer Chemistry, **37**, 493-499 (1999). DOI: 10.1002/(SICI)1099-0518(19990215)37:4<493::AID-POLA13>3.0.CO;2-Y

[19] Odian G.: Principles of polymerization. Wiley, New York (1970).

[20] Reich L.: Approximate estimation of activation energy from DTA and TGA traces. Journal of Polymer Science Part B: Polymer Letters, **4**, 423–426 (1966). DOI: 10.1002/pol.1966.110040610

[21] Yang M-H.: The two-stages thermal degradation of polyacrylamide. Polymer Testing, **17**, 191–198 (1998). DOI: 10.1016/S0142-9418(97)00036-6

[22] Hou T., Xu R. K., Zhao A. Z.: Interaction between electric double layers of kaolinite and Fe/Al oxides in suspensions. Colloids and Surfaces A: Physicochemical and Engineering Aspects, **297**, 91–94 (2007). DOI: 10.1016/j.colsurfa.2006.10.029